

# Solution based synthesis of Cu<sub>2</sub>ZnSnS<sub>4</sub> nanoparticles and thin films for solar cell application

Li, Zhenggang

2014

Li, Z. (2014). Solution based synthesis of Cu<sub>2</sub>ZnSnS<sub>4</sub> nanoparticles and thin films for solar cell application. Doctoral thesis, Nanyang Technological University, Singapore.

<https://hdl.handle.net/10356/61771>

<https://doi.org/10.32657/10356/61771>



# Solution Based Synthesis of $\text{Cu}_2\text{ZnSnS}_4$ Nanoparticles and Thin Films for Solar Cell Application

**Li Zhenggang**

School of Materials Science and Engineering

Aug 2014

# **SOLUTION BASED SYNTHESIS OF CU<sub>2</sub>ZNSNS<sub>4</sub> NANOPARTICLES AND THIN FILMS FOR SOLAR CELL APPLICATION**

**LI ZHENGANG**

**School of Materials Science and Engineering**

A thesis submitted to the Nanyang Technological University  
in partial fulfillment of the requirement for the degree of Doctor of Philosophy

**2014**

## Abstract

Quaternary chalcogenide compound  $\text{Cu}_2\text{ZnSnS}_4$  (CZTS) is a promising absorber material for low-cost thin film solar cells owing to the abundance of its constituents, suitable band-gap and high absorption coefficient. Conventionally, CZTS thin films are mainly fabricated using vacuum techniques including evaporation, sputtering and pulsed laser deposition. An encouraging power conversion efficiency of 8.4% has been achieved using vacuum deposition method. However, the vacuum deposition techniques are often associated with high energy input and thus impose a significant cost on the devices. Hence, there is a driving force towards replacing the vacuum deposition method with cost-effective processing techniques. In this thesis, I present the solution-based synthesis of CZTS nanoparticles and the deposition of CZTS thin films.

CZTS nanoparticles were successfully synthesized using hot injection method. It was found that the reaction temperature plays an important role in determining the phase formation. At reaction temperature below  $200^\circ\text{C}$ , the binary  $\text{Cu}_{2-x}\text{S}$  and ternary CTS form together with quaternary CZTS phases. At reaction temperature of  $220^\circ\text{C}$  and above, pure quaternary CZTS phase is favored. A detailed investigation of CZTS nanoparticles synthesized at  $240^\circ\text{C}$  shows that the nanoparticles have an average size of 19.8 nm and the average ratio of S, Cu, Zn and Sn was estimated to be 4.19: 1.96: 0.80: 1.05. In addition, the optical band gap of the CZTS nanoparticles was estimated to be 1.55 eV based on UV-vis-NIR absorption measurements. The reaction time greatly affects the nucleation and growth of nanoparticles. CZTS nanoparticles formed immediately after injection of S precursor. From 0 min to 30 min, the average size of the nanoparticles



gradually increased and the size distribution became narrower. With longer reaction time, the growth of nanoparticles shows the phenomenon of Ostwald ripening. The size and shape of nanoparticles could be controlled through solvent-ligand optimization. With 1,2-dichlorobenzene (DCB) as the solvent and oleylamine (OLA) as the ligand, sub-micrometer size clusters (0 ml OLA), near-spherical shape (0.5 ml OLA), faceted (1 ml OLA), and nanoplates (2 ml OLA) CZTS nanostructures were synthesized.

The sulfur precursor is the key parameter that determines the phase formation of CZTS polytypes. Kesterite CZTS were formed using elemental sulfur as the sulfur source, while wurtzite CZTS were produced using 1-dodecanthiol (DDT). The use of thioacetamide (TAA) resulted in the formation of mixture of kesterite and wurtzite phases. Further investigation revealed that the reaction rate of sulfur precursors plays a critical role. The elemental S could react with oleylamine to produce highly reactive small molecule  $H_2S$ , which then precipitate with Cu, Zn and Sn species to form kesterite CZTS nanoparticles. As for the case of DDT, the covalent bonded S is very stable and difficult to be broken down to release S, leading to formation of wurtzite phase. TAA exhibit reaction rate between elemental S and DDT, therefore yields a mixture of kesterite and wurtzite phases. The optical and electrical properties of kesterite and wurtzite were evaluated and showed similar properties. The optical band gaps of kesterite phase and wurtzite phase were estimated based on absorption measurements to be 1.48 eV and 1.55 eV respectively. The valance band and conduction band energy levels are determined using CV measurements to be -5.37 and -3.85 eV (kesterite), -5.60 and -3.91 eV (wurtzite).

Compared with CZTS nanoparticles ink approach, a greener synthesis route based on CuS, ZnS and  $SnS_2$  nanoparticles with water or ethanol solvent was developed. The post-

annealing plays an important role in the phase evolution from binary phases into quaternary CZTS phase. It was found that pure CZTS phase formed at 300°C, 400°C and 450°C. The selenization process was performed on the nanoparticles precursor film. CZTSSe thin film solar cells were fabricated following Mo/CZTSSe/CdS/ZnO/ITO/Au architecture. The as-fabricated device exhibited a total area efficiency of 5.12% with  $V_{oc}$  of 378 mV,  $J_{sc}$  of 26.2 mA/cm<sup>2</sup> and FF of 51.7%. These results are comparable with some of the best performing nanoparticles based CZTSSe solar cells. Combined with the low-cost, environmentally friendly and upscalable fabrication steps, our synthesis method is highly promising for potential industry scale application.

# Acknowledgement

I would like to acknowledge and express my deep gratitude towards the following persons who have contributed and supported my Ph.D studies as well as the completion of this thesis.

First of all, I would like to express my foremost gratitude and appreciation to my supervisor, Associate Professor Lam Yeng Ming, for her patient guidance and generous support throughout my Ph.D studies. It has always been a great pleasure to work with her. Her encyclopedic knowledge, insightful suggestions and optimistic attitude encourage me to overcome all kinds of difficulties encountered in my research.

I would also like to extend my deep appreciation to Professor Subodh Mhaisalkar and Assistant Professor Lydia Helena Wong from the Institute of Energy Research at NTU (ERI@N) for their suggestions and feedback during the group meeting.

I would also want to thank those have helped me with experimental work, sample measurements and results analysis. They are Dr. Stevin Snellius Pramana, Dr. Xi Lifei, Mr. Lam Kwan Hang, Mr. Cai Yongan, Mr. Ho Chun Wan John, Mr. Zhang Tianliang, Mr. Lee Kian Keat and Mr. Zeng Xin.

My gratitude also goes to the following undergraduate students Mr. Bian Shangzhi, Mr. Lim Hong Yi, Mr. Keng Wei Lieh Willie, Mr. Alvic Lim and Mr. Wong Chong Hou for their help in experimental work. The contribution of their work to this thesis is greatly acknowledged.

I am grateful to have worked with some of the best groupmates: Mr. Sun Shuangyong, Dr. Mahshid Ahmadi, Dr. Teddy Salim, Dr. Lek Jun Yan, Mr. Abe Yuichiro and the CIGS group members.

Last but not least, I would extend my gratitude to my wife Dr. Lai Linfei for her strong emotional support and encouragement during Ph.D studies. I am thankful to her for being not only the best wife but also great friend.

# Table of Contents

<b>Abstract</b>	<b>i</b>
<b>Acknowledgements</b>	<b>iv</b>
<b>Table of Contents</b>	<b>vi</b>
<b>List of Figures</b>	<b>viii</b>
<b>List of Tables</b>	<b>xiii</b>
<b>List of Abbreviations</b>	<b>xiv</b>
<b>Chapter 1: Introduction</b>	<b>1</b>
1.1 Research Background and Motivation	1
1.2 Objectives and Scope	4
1.3 Thesis Organization	5
<b>Chapter 2: Literature Review</b>	<b>9</b>
2.1 Synthesis of CZTS Nanoparticles	9
2.1.1 Synthesis methods	9
2.1.2 Properties of CZTS kesterite	11
2.1.3 Size and shape control	17
2.2 CZTS Thin Film Deposition Approaches	20
2.2.1 Vacuum deposition techniques	20
2.2.2 Non-vacuum deposition techniques	21
2.3 CZTSSe Based Solar Cells	24
<b>Chapter 3: Controlled Synthesis of Characterizations of Cu<sub>2</sub>ZnSnS<sub>4</sub> Nanoparticles</b>	<b>35</b>
3.1 Introduction	35
3.2 Experimental Procedures	37
3.3 Results and Discussion	39
3.3.1 Effects of reaction temperature	40
3.3.2 Effect of reaction time – A study on growth mechanism	47

3.3.3 Effect of solvent and ligand.....	53
3.4 Conclusions.....	58
<b>Chapter 4: Controlled Synthesis of Kesterite-type and Wurtzite-type CZTS Nanoparticles through Sulfur Precursor .....</b>	<b>63</b>
4.1 Introduction.....	63
4.2 Experimental Procedures.....	68
4.3 Results and Discussion.....	69
4.3.1 Synthesis of CZTS nanoparticles with different phases.....	70
4.3.2 Growth mechanism for kesterite and wurtzite.....	75
4.3.4 Effects of crystal structures on optical and electrical properties.....	79
4.4 Conclusions.....	83
<b>Chapter 5: Synthesis of CZTS Thin Films Using Binary Sulfides Nanoparticles.....</b>	<b>88</b>
5.1 Introduction.....	88
5.2 Experimental Procedures.....	91
5.3 Results and Discussion.....	94
5.3.1 Binary sulfide nanoparticles.....	94
5.3.2 Kesterite CZTS thin film using binary sulfide nanoparticles.....	97
5.3.3 Solar cell performance.....	103
5.4 Conclusions.....	109
<b>Chapter 6: Conclusions and Future Works.....</b>	<b>114</b>
6.1 Overall Summary.....	114
6.2 Scientific Contributions.....	116
6.3 Future Recommendation.....	117
<b>Appendix A.....</b>	<b>119</b>
<b>Appendix B.....</b>	<b>121</b>
<b>Appendix C.....</b>	<b>122</b>

## List of Figures

<b>Figure 2.1.</b> (a) TEM, (b) HRTEM and (c) SEM images of the CZTS nanoparticles synthesized using hot injection method.....	10
<b>Figure 2.2.</b> The typical XRD pattern of CZTS nanoparticles prepared with hot injection method. The red reference pattern was the standard XRD pattern for kesterite CZTS. Inset shows the intensity in log scale. ....	12
<b>Figure 2.3.</b> The Raman spectrum of CZTS under 488 nm laser showing Raman peaks at $288\text{ cm}^{-1}$ , $338\text{ cm}^{-1}$ and $368\text{ cm}^{-1}$ . The shade area is due to the synergic effect of $338\text{ cm}^{-1}$ and $368\text{ cm}^{-1}$ . ....	14
<b>Figure 2.4.</b> The typical UV-vis-NIR absorption measurement of CZTS nanocrystals. The inset shows the $(\alpha h\nu)^2$ vs. $h\nu$ plot from which band gap was estimated.....	16
<b>Figure 2.5.</b> The photoelectrochemical response of near stoichiometric CZTS nanocrystal thin films. The inset shows the photostability test at negative bias of -500 mV. ....	17
<b>Figure 2.6.</b> HRTEM images of synthesized CZTS nanocrystals with diameters of: (a) 2 nm, (b) 2.5 nm, (c) 5 nm, (d) 7 nm. The scale bars in a-d are 2 nm. (e) the UV-vis-NIR absorption measurement CZTS nanoparticles with different size. The inset displays the Tauc plot for the corresponding absorbance curves. ....	18
<b>Figure 2.7.</b> (a) and (b) the SEM images of the CZTS nanowires array prepared with AAO template. ....	19
<b>Figure 2.8.</b> Overview of solar cell fabrication using nanoparticles “ink” approach. (a) synthesis of nanoparticles, (b) nanoparticles ink formation, (c) film deposition, (d) heat treatment of as deposited film and (e) Device fabrication.....	23

<b>Figure 2.9.</b> Ternary phase diagram of CZTS prepared by sulfidizing stacked metal layers. ....	25
<b>Figure 2.10.</b> (a) the architecture of CZTSSe based TFSCs and (b) its energy band diagram under zero-bias. ....	26
<b>Figure 2.11.</b> (a) J–V curve under light and dark condition. (b) EQE curve of the cell. Inset: band gap determination of the cell from the EQE data. ....	28
<b>Figure 2.12.</b> Cross-sectional (a) TEM image and (b) EDX line scan of CZTSSe solar cell prepared using hydrazine method. ....	28
<b>Figure 3.1:</b> A brief illustration of experimental setup for the synthesis of CZTS nanocrystals using hot injection method. The metal precursor contains Cu-, Zn- and Sn-OLA complex. ....	38
<b>Figure 3.2.</b> The XRD diffraction patterns of samples prepared at different reaction temperatures of 180, 200, 220, 240 and 260 °C. The standard diffraction peaks for kesterite CZTS (JCPDS no. 26-0575) is provided. ....	41
<b>Figure 3.3.</b> The Raman analysis of samples prepared at different reaction temperatures of 180, 200, 220, 240 and 260 °C. The peak positions of 288, 338 and 368 cm <sup>-1</sup> are labeled with vertical dotted lines. ....	42
<b>Figure 3.4.</b> The rietveld refinement XRD data obtained from samples prepared at 240 °C. A five-coefficient Chebychev polynomial and 1/x background, a zero error, scale factor, lattice parameters, crystal size and preferred orientation were successively refined. ....	43
<b>Figure 3.5.</b> (a) TEM and (b) HRTEM images of as-synthesized CZTS. The TEM sample was prepared by dropping casting CZTS nanoparticles suspension onto a Ni-grid. ....	45
<b>Figure 3.6.</b> STEM-EDS elemental mapping of as-synthesized CZTS nanocrystals. The distributions of Cu, Zn, Sn and S were presented. ....	46



<b>Figure 3.7:</b> UV-vis absorption spectrum of as synthesized CZTS nanocrystals. Inset shows the $h\nu$ vs. $(\alpha h\nu)^2$ and the band gap is calculated to be 1.55 eV. ....	47
<b>Figure 3.8:</b> The XRD patterns of CZTS nanoparticles synthesized at different reaction time of 0 min, 10 min, 30 min, 1 h, 2 h and 6 h. ....	48
<b>Figure 3.9.</b> The TEM images of CZTS nanoparticles synthesized at 240 °C with different reaction time of (a) 0 min, (b) 10 min, (c) 30 min, (d) 1 h, (e) 2 h, and (f) 6 h. The scale bar stands for 100 nm for all. (g-l) presents the size distribution for (a-f) sequentially. ....	49
<b>Figure 3.10.</b> The average size of nanoparticles vs. $t^{1/3}$ plot where t is the reaction time. The near linear relationship is observed from 30 min onward. ....	51
<b>Figure 3.11.</b> (a) The XRD pattern and (b) the Raman analysis of CZTS nanoparticles synthesized with DCB solvent and 1 ml OLA as surfactant. ....	54
<b>Figure 3.12.</b> TEM images of CZTS nanoparticles with (a) 0 ml, (b) 0.5 ml, (c) 1 ml, (d) 2ml OLA, and HRTEM images of CZTS nanoparticles with (e) 1 ml OLA and (f) 2 ml OLA. ....	56
<b>Figure 4.1.</b> Close relationship of ternary $\text{CuInSe}_2$ and quaternary $\text{Cu}_2\text{ZnSnS}_4$ to binary ZnS with cation substitutions. ....	64
<b>Figure 4.2.</b> The unit cell structure of CZTS (a) kesterite (in the Cu-Zn layer, the Cu and Zn ions have equal occupancy of 0.5) and (b) wurtzite (the red ion represent Cu, Zn or Sn ions with the 0.5 occupancy of Cu ion, 0.25 occupancy of Zn ion and 0.25 occupancy of Sn ions). ....	66
<b>Figure 4.3.</b> The XRD patterns of as synthesized samples using elemental S, DDT and TAA as the sulfur source respectively. The XRD database for kesterite CZTS and wurtzite CZTS are also presented and indexed for comparison. ....	72
<b>Figure 4.4.</b> The Raman shifts of sample S, sample DDT and sample TAA. The peak positions of 288, 338 and 368 $\text{cm}^{-1}$ are marked by dotted lines. ....	73

<b>Figure 4.5:</b> The TEM images of (a) sample S, (c) sample DDT, (e) sample TAA, and the high-resolution TEM images of (b) sample S, (d) sample DDT, (f) sample TAA. The lattice spacing is calculated and labeled in the high resolution images. ....	74
<b>Figure 4.6:</b> The XRD patterns of CZTS nanoparticles synthesized using elemental S as the sulfur source with different reaction timings of 10 min, 30 min, 60 min and 120 min. ....	76
<b>Figure 4.7:</b> The XRD patterns of sample DDT at reaction timing of 10 min, 30 min, 1 hour and 2 hours. ....	77
<b>Figure 4.8:</b> The UV-vis-NIR absorbance of sample S, sample DDT and sample TAA. Inset: the $(\alpha h\nu)^2$ vs. $h\nu$ plot for the three samples and the dotted tangent lines were drawn to assist estimating the band gap. ....	80
<b>Figure 4.9.</b> The cyclic voltammograms of the oxidation potential of Ferrocene as the internal standard in order to calibrate the measurements. From the oxidation scan the onset of the curve shows the oxidation potential of ferrocene to be 0.3V. ....	81
<b>Figure 4.10.</b> Cyclic voltammetry of CZTS nanoparticles samples prepared with elemental S, DDT and TAA. ....	82
<b>Figure 5.1.</b> The scheme of the preparations of CZTS thin film using CuS, ZnS and SnS <sub>2</sub> nanoparticles. ....	93
<b>Figure 5.2.</b> The XRD patterns of as-synthesized CuS, ZnS and SnS <sub>2</sub> nanoparticles. The diffraction peaks for CuS (JCPDS no. 6-0464) and ZnS (JCPDS no. 5-0566) from the database are also shown as comparison. The XRD samples were prepared by spraying the respective nanoparticles suspension in ethanol onto glass substrates. ....	95
<b>Figure 5.3.</b> The TEM images of as-synthesized (a) CuS, (b) ZnS and (c) SnS <sub>2</sub> nanoparticles. ....	96
<b>Figure 5.4.</b> The XRD spectra for the as-prepared precursor film and the films that were annealed at 200, 300, 400 and 450 °C. The reference diffraction peaks for kesterite CZTS	

(JCPDS no. 26-0575) is also displayed at bottom. ....	98
<b>Figure 5.5.</b> The Raman analysis of the films annealed at 300, 400 and 450 °C. The peak position of 288, 336 and 368 cm <sup>-1</sup> are marked with vertical dotted lines. ....	99
<b>Figure 5.6.</b> Electron micrographs of sample annealed at 400 °C. (a) Top view SEM image of CZTS thin film and (b) cross-sectional view of SEM image. (c) HRTEM image and (d) SAED pattern. ....	100
<b>Figure 5.7.</b> STEM-EDS elemental mapping of the particles obtained from as prepared CZTS film. The distributions of Cu, Zn, Sn and S are presented. ....	100
<b>Figure 5.8.</b> The $(\alpha h\nu)^2$ versus $h\nu$ plots for stoichiometric CZTS and Zn-rich CZTS. The interception of the dotted lines with $h\nu$ axis determines the band gap. ....	103
<b>Figure 5.9.</b> The XRD pattern of CZTS film prepared by annealing the precursor film and CZTSSe film prepared by selenized the precursor film: (a) full scale and (b) magnified version. ....	104
<b>Figure 5.10.</b> The SEM images of the annealed film (a) topography and (b) cross-section, and selenized film (c) topography and (d) cross-section. ....	105
<b>Figure 5.11.</b> (a) The cross-sectional SEM image of CZTSSe TFSC and (b) the J-V curve of the as-prepared CZTSSe solar cells in dark and under AM1.5G illumination. ....	107
<b>Figure 5.12.</b> (a) The EQE of the CZTSSe solar cell, and (b) the corresponding $(E\ln(1-EQE))^2$ vs. $h\nu$ plot where the band gap is determined to be 1.18 eV. ....	108

## List of Tables

<b>Table 3.1</b> The average size and standard derivation of CZTS nanoparticles with respect to reaction time .....	49
<b>Table 4.1</b> A comparison of CB and VB energy level as well as the electrochemical band gap of sample S, DDT and TAA .....	82
<b>Table 5.1</b> Synthesis details for CuS, ZnS and SnS <sub>2</sub> nanoparticles.....	92

## List of Abbreviations

AAO	Anodic aluminum oxide
AM	Air mass
AZO	Aluminum doped zinc oxide
CIGS	Copper indium gallium diselenide
CIS	Copper indium diselenide
CTAB	Cetyl trimethylammonium bromide
CV	Cyclic Voltammetry
CTS	Copper tin sulfide
CZTS	Copper zinc tin sulfide
CZTSSe	Copper zinc tin sulfide selenide
DC	Direct current
DCB	Dichlorobenzene
DDPA	Dodecylphosphonic acid
DDT	Dodecanethiol
DSSC	Dye sensitized solar cell
DTA	Differential thermal analysis
EDS	Energy dispersive X-ray spectroscopy
EPMA	Electron probe micro-analyzer
EQE	External quantum efficiency
FESEM	Field emission scanning electron microscopy
FTO	Fluorine-doped tin oxide
FWHM	Full width at half maximum
GIXRD	Grazing incident X-ray diffraction
HDA	Hexadecylamine
HRTEM	High-resolution transmission electron microscopy

ITO	Indium-doped tin oxide
JCPDS	Joint committee on powder diffraction standards
OA	Oleic acid
OLA	Oleylamine
PCBM	Phenyl c-61 butyric acid methyl ester
PCE	Power conversion efficiency
QDSSC	Quantum dot sensitized solar cell
RF	Radio frequency
S	Sulfur
SAED	Selected area electron diffraction
SEM	Scanning electron microscopy
STEM	scanning transmission electron microscopy
TAA	Thioacetamide
TCO	Transparent conducting oxide
TEM	Transmission electron microscopy
TFSC	Thin film solar cell
TOPAS	Total pattern analysis solution
TOPO	Trioctylphosphonic acid
TRPL	Time-resolved photoluminescence
UPS	Ultraviolet photoelectron spectroscopy
UV-vis-NIR	Ultraviolet-visible-near infrared
XRD	X-ray diffraction

# Chapter 1: Introduction

## 1.1 Research Background and Motivation

Currently, CdTe and  $\text{CuIn}_x\text{Ga}_{1-x}\text{Se}_2$  (CIGS) are the two leading technologies for thin film solar cells (TFSCs). Both technologies have demonstrated high device performance with the record efficiencies of 19.6% (CdTe) and 20.4% (CIGS).<sup>1</sup> CdTe solar cells have been commercialized by First Solar with module efficiency of over 10%, while CIGS solar cells are now starting to move into industrial scale production. However, both technologies have practical limitations: CdTe involves the use of toxic Cd and is thus detrimental to the environment, while CIGS contains rare metal - In and Ga and these elements would greatly limit the production capacity of such cells.<sup>2</sup> Hence, there is an urgent need to find alternative materials for TFSCs which consist of earth-abundant and low toxicity elements.

Quaternary  $\text{Cu}_2\text{ZnSnS}_4$  (CZTS) kesterite is a emerging absorber material for TFSCs. It has a crystal structure similar to that of  $\text{CuInSe}_2$  where Se is substituted by S and In is substituted by Zn and Sn. CZTS possessed good optical properties for photovoltaic applications: (i) optimal band gap for solar cells of 1.5 eV and (ii) large absorption coefficient of more than  $10^4 \text{ cm}^{-1}$ . It is also worth to note that CZTS contains all earth-abundant elements compared with CIGS and CdTe. The earth crust contains 50 ppm Cu, 75 ppm Zn, 2.2 ppm Sn, 260 ppm S, all of which are several orders magnitude higher than the content of Te (0.001 ppm) and In (0.05 ppm).<sup>3</sup> The abundance of these elements suggests a lower materials cost and the potential for large scale production capacity of

CZTS compared to CIGS and CdTe. In addition, CZTS consists of elements that are non-toxic as compared to CdTe.

Conventionally, CZTS based TFSCs were fabricated using vacuum deposition techniques. In one common approach, stacked Cu-, Zn- and Sn-metal layers were deposited through either sputtering or evaporation, and were then subjected to high-temperature annealing in H<sub>2</sub>S environment to form CZTS.<sup>4</sup> The ratio of Cu, Zn and Sn could be tuned by modifying the thickness of each metal layer. Another deposition method makes use of co-evaporation of Cu, Zn, Sn and S on a substrate followed by annealing, which yields a high efficiency of 8.4%.<sup>5</sup> Despite this excellent progress, the vacuum techniques still require high energy input and impose a significant cost on devices. Hence, there is a drive to replace the vacuum deposition techniques with a low-cost solution deposition method.

Solution processable TFSCs allows the use of low-cost processing techniques including the reel-to-reel processes, printing, spin-coating and spraying, which leads to a huge reduction in the production cost.<sup>6,7</sup> As a result, solution processable TFSCs is now being intensively investigated. In the case of CZTS, several solution deposition routes have been reported to prepared CZTS thin film. Guo et al. synthesized CZTS nanoparticles using hot injection method and use the nanoparticles dispersion as an ink to form CZTS thin film.<sup>8</sup> Todorov et al. deposited kesterite CZTS<sub>Se</sub> thin film by spin-coating hybrid solution-particles precursors in hydrazine.<sup>9</sup> Scragg et al. prepared kesterite CZTS thin film using electrodeposition method.<sup>10</sup> Kumar et al. synthesized CZTS thin film by spray pyrolysis technique, where the precursor solution contained Cu-, Zn-, Sn-salts and thiourea.<sup>11</sup> Among the above solution deposition approaches, the CZTS nanoparticles ink



approach and the hydrazine approaches have demonstrated high efficiencies of 7.2% and 11.1% respectively.<sup>12, 13</sup> Despite the good device performance, these two approaches suffer from several disadvantages including the toxic solvents and highly demanding processing conditions. The electrodeposition techniques and spray pyrolysis approaches make use of environmentally friendly water as solvent, however, their device performance remain low compared CZTS nanoparticles ink and hydrazine approaches.

Recently, the preparation of CZTS thin film via nanocrystals dispersion has attracted much attention.<sup>8, 14, 15</sup> Nanocrystals dispersion or inks consists of pre-synthesized nanocrystals usually by hot injection method and they are then deposited using low cost solution-processing techniques such as printing, spraying and spin-coating. The as-deposited nanocrystals film can be either used as deposited or thermally annealed to form larger grains. Using this approach, a very promising solar cell efficiency of 7.2% have been achieved<sup>12</sup>. However, at the time being that this work was carried out, the effects of synthesis parameters on the formation of CZTS nanocrystals are still not clearly understood. The reaction temperature, reaction time, solvent and ligand are the key synthesis parameters in the hot coordinating solvent method, which may have great influences on the size, morphology as well as composition of CZTS nanoparticles. The knowledge on the effects of these parameters is very beneficial on the controlled synthesis of CZTS nanoparticles.

Kesterite and wurtzite are two important structural polytypes of CZTS.<sup>16</sup> The kesterite structure has a tetragonal lattice structure, while the wurtzite structure features a hexagonal unit cell. Several different approaches have been demonstrated to synthesize

kesterite CZTS nanoparticles.<sup>2, 17</sup> The morphology of kesterite CZTS could also be controlled to some extent.<sup>18</sup> Recently, the metastable wurtzite phase has also been reported.<sup>16, 19, 20</sup> Despite the above excellent progress, several critical issues remain unsolved. Firstly, the key factors that determine the formation of each phase need to be uncovered. In addition, the structural difference may translate into property differences.<sup>21-23</sup> Controlled synthesis of kesterite and wurtzite phases as well as elucidation of the properties of each phase could provide a guideline in the application of the different phases of the material.

For CZTS thin film solar cells to be viable, low-cost, environmentally friendly nanocrystals inks are highly desirable. In the previous work, CZTS nanoparticles dispersion was often used as the ink.<sup>12, 14, 15</sup> However, it has two main limitations: (i) the synthesis of CZTS nanoparticles are often involved with expensive, toxic organic solvents such as oleylamine (OLA) and trioctylphosphine oxide (TOPO); (ii) harsh experimental conditions including high reaction temperature, inert gas environment are required during the synthesis. Therefore, novel nanocrystals ink which is synthesized using low-cost methods and environmentally friendly solvents need to be developed.

## 1.2 Objectives and Scope

In view of the challenges mentioned above, the main objectives of this thesis dissertation are summarized as below:

- 1. Understand the effects of the key synthesis parameters on the formation of CZTS nanoparticles.** CZTS nanoparticles are synthesized using hot injection method.

The effects of key reaction parameters including temperature, time, solvent and ligand are investigated in-depth in order to achieve better control over the size, shape and composition of the nanoparticles. The growth mechanism will be proposed based on the research findings.

- 2. Synthesize kesterite, wurtzite as well as mixed kesterite-wurtzite CZTS nanocrystals and understand their formation mechanisms.** CZTS nanoparticles are synthesized using various sulfur sources including elemental sulfur (S), 1-dodecanethiol (DDT) and thioacetamide (TAA) and their crystal structures will be investigated respectively. The formation mechanism of both kesterite and wurtzite phases will be discussed. In addition, the properties including the absorption, energy levels as well as the photoresponse of kesterite and wurtzite are investigated and compared.
- 3. Demonstrate low-cost, environmentally friendly water soluble nanocrystals ink based on CuS, ZnS and SnS<sub>2</sub> nanoparticles.** Instead of quaternary CZTS nanocrystals, the binary CuS, ZnS and SnS<sub>2</sub> nanoparticles are synthesized and used as the ink. The phase formation of CZTS thin film at various temperatures is studied. Lastly, TFSCs are fabricated using the as-developed binary sulfide nanocrystals ink approach and the performance are evaluated and discussed.

### 1.3 Thesis Organization

This thesis is organized as below:

In Chapter 1, a brief introduction of research background has been provided. The research objectives and thesis organization are also presented.

In Chapter 2, the synthesis of CZTS nanoparticles will be briefly reviewed. And various deposition methods for CZTS thin films will also be discussed. In addition, the CZTS based solar cells will also be touched on.

Chapter 3 focuses on the synthesis and characterizations of CZTS nanocrystals using hot coordinating solvent methods. The effects of synthesis parameters such as reaction temperature, reaction time, solvent and ligand will be discussed.

Chapter 4 presents the controlled synthesis of kesterite and wurtzite type CZTS nanocrystals through sulfur source. Detailed investigations are carried out and the growth mechanism of the two structures will be proposed.

Chapter 5 describes the preparations of CZTS thin film using greener approach based on binary sulfides nanoparticles. CZTS based solar cells using this approach are also demonstrated.

Chapter 6 states the overall summary. Future recommendations are also proposed along with the conclusions.

## References

1. Green, M. A.; Emery, K.; Hishikawa, Y.; Warta, W.; Dunlop, E. D., Solar cell efficiency tables (version 42). *Progress in Photovoltaics: Research and Applications* **2013**, 21, (5), 827-837.
2. Mitzi, D. B.; Gunawan, O.; Todorov, T. K.; Wang, K.; Guha, S., The path towards a high-performance solution-processed kesterite solar cell. *Solar Energy Materials and Solar Cells* **2011**, 95, (6), 1421-1436.

3. S.R.Taylor, S. M. M., The continental crust: its composition and evolution: an examination of the geochemical record preserved in sedimentary rocks. *Blackwell Scientific Publication* **1985**, Oxford.
4. Katagiri, H., Cu<sub>2</sub>ZnSnS<sub>4</sub> thin film solar cells. *Thin Solid Films* **2005**, 480-81, (0), 426-432.
5. Shin, B.; Gunawan, O.; Zhu, Y.; Bojarczuk, N. A.; Chey, S. J.; Guha, S., Thin film solar cell with 8.4% power conversion efficiency using an earth-abundant Cu<sub>2</sub>ZnSnS<sub>4</sub> absorber. *Progress in Photovoltaics: Research and Applications* **2011**, 21, (1), 72-76.
6. Butler, D., Thin films: ready for their close-up? *Nature* **2008**, 454.
7. Shah, A.; Torres, P.; Tscharnner, R.; Wyrsh, N.; Keppner, H., Photovoltaic Technology: The Case for Thin-Film Solar Cells. *Science* **1999**, 285, (5428), 692-698.
8. Guo, Q.; Hillhouse, H. W.; Agrawal, R., Synthesis of Cu<sub>2</sub>ZnSnS<sub>4</sub> Nanocrystal Ink and Its Use for Solar Cells. *Journal of the American Chemical Society* **2009**, 131, (33), 11672-11673.
9. Todorov, T. K.; Reuter, K. B.; Mitzi, D. B., High-Efficiency Solar Cell with Earth-Abundant Liquid-Processed Absorber. *Advanced Materials* **22**, (20), E156-+.
10. Scragg, J. J.; Berg, D. M.; Dale, P. J., A 3.2% efficient Kesterite device from electrodeposited stacked elemental layers. *Journal of Electroanalytical Chemistry* **646**, (1-2), 52-59.
11. Kumar, Y. B. K.; Babu, G. S.; Bhaskar, P. U.; Raja, V. S., Preparation and characterization of spray-deposited Cu(2)ZnSnS(4) thin films. *Solar Energy Materials and Solar Cells* **2009**, 93, (8), 1230-1237.
12. Guo, Q.; Ford, G. M.; Yang, W.-C.; Walker, B. C.; Stach, E. A.; Hillhouse, H. W.; Agrawal, R., Fabrication of 7.2% efficient CZTSSe solar cells using CZTS nanocrystals. *Journal of the American Chemical Society* **2010**, 132, (49), 17384-17386.
13. Todorov, T. K.; Tang, J.; Bag, S.; Gunawan, O.; Gokmen, T.; Zhu, Y.; Mitzi, D. B., Beyond 11% efficiency: characteristics of state-of-the-art Cu<sub>2</sub>ZnSn(S,Se)<sub>4</sub> solar cells. *Advanced Energy Materials* **2012**, 3, (1), 34-38.
14. Steinhagen, C.; Panthani, M. G.; Akhavan, V.; Goodfellow, B.; Koo, B.; Korgel, B. A., Synthesis of Cu<sub>2</sub>ZnSnS<sub>4</sub> Nanocrystals for Use in Low-Cost Photovoltaics. *Journal of the American Chemical Society* **2009**, 131, (35), 12554-12555.
15. Riha, S. C.; Parkinson, B. A.; Prieto, A. L., Solution-Based Synthesis and Characterization of Cu<sub>2</sub>ZnSnS<sub>4</sub> Nanocrystals. *Journal of the American Chemical Society* **2009**, 131, (34), 12054-12055.
16. Lu, X.; Zhuang, Z.; Peng, Q.; Li, Y., Wurtzite Cu<sub>2</sub>ZnSnS<sub>4</sub> nanocrystals: a novel quaternary semiconductor. *Chemical Communications* **2011**, 47, (11), 3141-3143.

17. Bucherl, C. N.; Oleson, K. R.; Hillhouse, H. W., Thin film solar cells from sintered nanocrystals. *Current Opinion in Chemical Engineering* **2**, (2), 168-177.
18. Shi, L.; Pei, C.; Xu, Y.; Li, Q., Template-directed synthesis of ordered single-crystalline nanowires arrays of  $\text{Cu}_2\text{ZnSnS}_4$  and  $\text{Cu}_2\text{ZnSnSe}_4$ . *Journal of the American Chemical Society* **2011**, 133, (27), 10328-10331.
19. Chen, S.; Walsh, A.; Luo, Y.; Yang, J.-H.; Gong, X. G.; Wei, S.-H., Wurtzite-derived polytypes of kesterite and stannite quaternary chalcogenide semiconductors. *Physical Review B* **82**, (19), 195203.
20. Regulacio, M. D.; Ye, C.; Lim, S. H.; Bosman, M.; Ye, E.; Chen, S.; Xu, Q.-H.; Han, M.-Y., Colloidal Nanocrystals of Wurtzite-Type  $\text{Cu}_2\text{ZnSnS}_4$ : Facile Noninjection Synthesis and Formation Mechanism. *Chemistry – A European Journal* **18**, (11), 3127-3131.
21. Powell, R. C.; Lee, N. E.; Kim, Y. W.; Greene, J. E., Heteroepitaxial wurtzite and zinc blende structure GaN grown by reactive-ion molecular-beam epitaxy - growth-kinetics, microstructure, and properties. *Journal of Applied Physics* **1993**, 73, (1), 189-204.
22. Herbst, J. F.; Croat, J. J.; Pinkerton, F. E.; Yelon, W. B., RELATIONSHIPS BETWEEN CRYSTAL-STRUCTURE AND MAGNETIC-PROPERTIES IN  $\text{Nd}_2\text{Fe}_{14}\text{B}$ . *Physical Review B* **1984**, 29, (7), 4176-4178.
23. Paier, J.; Asahi, R.; Nagoya, A.; Kresse, G.,  $\text{Cu}_2\text{ZnSnS}_4$  as a potential photovoltaic material: A hybrid Hartree-Fock density functional theory study. *Physical Review B* **2009**, 79, (11).

# Chapter 2: Literature Review

## 2.1 Synthesis of CZTS Nanoparticles

As a promising alternative material for TFSCs, the quaternary  $\text{Cu}_2\text{ZnSnS}_4$  (CZTS) has been studied intensively in the last decade.<sup>1-3</sup> Particularly, the synthesis of CZTS nanocrystals has attracted great attention mainly owing to the ability to be solution-processed into absorber films.<sup>4, 5</sup> Until now, CZTS nanoparticles based TFSCs have demonstrated a very promising solar cell efficiency of 7.2%.<sup>6</sup> And much more research on the synthesis, characterizations, properties and applications of CZTS nanoparticles are on-going.

### 2.1.1 Synthesis methods

The synthesis of CZTS nanoparticles was firstly reported with hot injection method.<sup>7-9</sup> This method features the rapid injection of sulfur precursor into metal precursor at desired temperature. Essentially, the metal precursor was prepared by mixing of Cu, Zn, Sn salts with the coordinating solvent (usually oleylamine) and heated in a three neck flask under inert gas environment. During this incubation process, the stable Cu-, Zn-, Sn-oleylamine coordinating complex will be formed.<sup>9</sup> The sulfur precursor was prepared separately in a 10 ml vial by dissolving elemental S into oleylamine. Figure 2.1 presents the TEM and SEM images of the typical CZTS nanoparticles prepared using this method.<sup>8</sup> As shown in Figure 2.1a and c, well crystalline CZTS nanoparticles with irregular shape and size in the range of a few nanometer to a few tens of nanometers were obtained. The lattice spacing of  $3.1\text{\AA}$  (Figure 2.1b) matched well with the d-spacing of

(112) planes for CZTS kesterite. Later on, Kameyama et al. modified the synthesis with the elimination of injection process.<sup>10</sup> In this case, the Cu, Zn, Sn salts, elemental S and oleylamine were mixed together and heated in one-pot for form CZTS nanoparticles. Furthermore, the continuous production using a flow reactor makes it possible to produce CZTS nanoparticles in large scale.<sup>11</sup>

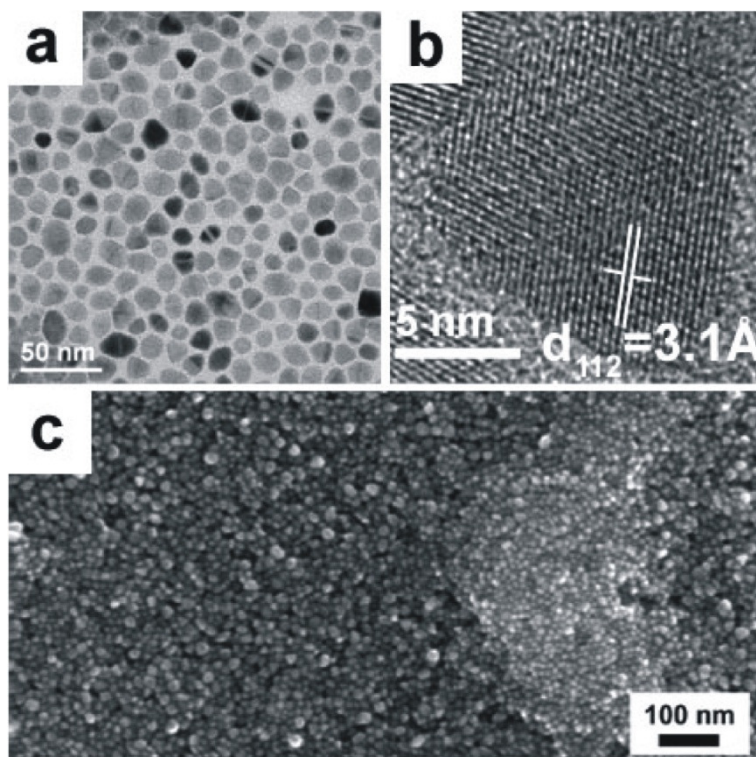


**Figure 2.1.** (a) TEM, (b) HRTEM and (c) SEM images of the CZTS nanoparticles synthesized using hot injection method. The images are reprinted based on the work of Steinhagen et al.<sup>8</sup>

Much progress has also been made in other solvothermal methods. Zhou et al. reported the preparations of CZTS nanostructures in an autoclave using ethylene glycol as the solvent.<sup>12</sup> The as-synthesized CZTS nanocrystals self-assembled into a sphere-like shape with the average size the sphere ranging from 100 to 150 nm. Using ethylenediamine, Cao et al. managed to obtain smaller particles (5 ~ 10nm).<sup>13</sup> Wang et al. prepared CZTS



nanoparticles using two-phase method with 1-octadecene and triethylene glycol.<sup>14</sup> A similar setup to the hot coordinating solvent method was used.

Hydrothermal method, which offer a green option compared with solvothermal method, is highly desirable in the preparations of CZTS nanoparticles. Wang et al. successfully demonstrated CZTS nanostructures using an autoclave with hydrothermal method.<sup>15</sup> The aqueous soluble thiourea was used as the sulfur precursor. Zhao et al. reported hydrophilic CZTS nanocrystals by mixing  $(\text{NH}_4)_2\text{S}$  solution with Cu, Zn, Sn precursor solution at room temperature, which avoids the use of long chain ligands.<sup>16</sup>

In this thesis dissertation, hot injection method will be used to synthesize CZTS nanoparticles. The hot injection method has been proven to be a robust technique to synthesize various semiconductor nanocrystals including CdSe, ZnS, PbS and  $\text{Cu}_2\text{InSe}_2$ .<sup>17-20</sup> The injection process adopted by this method allows separate nucleation and growth steps for nanoparticles, and thus offers narrower size distribution.<sup>21, 22</sup> Moreover, through ligand optimization, the shape of the nanocrystals could be easily controlled.

### 2.1.2 Properties of CZTS kesterite

Quaternary semiconductor  $\text{Cu}_2\text{ZnSnS}_4$  (CZTS) kesterite is a emerging absorber material. The crystal structure of CZTS is very similar to that of  $\text{CuInSe}_2$  (CIS) compound with substitution of atoms.<sup>23, 24</sup> The rare metal In atoms are replaced by earth-abundant Zn and Sn atoms, while Se is substituted by S atoms. CZTS possesses good optical properties to function as absorber material for solar cells, which has a suitable band gap around 1.5 eV

and a high absorption coefficient of more than  $10^4 \text{ cm}^{-1}$ .<sup>1</sup> One major advantage of CZTS over the CIS and CdTe technologies is that it contains all abundant elements in earth crust: Zn (75 ppm), Sn (2.2 ppm) compared to In (0.05 ppm); S (260 ppm) compared to Te (0.001 ppm).<sup>25</sup> This allows CZTS to have a much greater production capacity than the currently commercialized CIS and CdTe. Moreover, CZTS has low toxicity as compared to CdTe (The heavy metal Cd could lead to poisoning on the soil).<sup>26</sup> Given the above facts, CZTS has a huge potential for the application in TFSCs.

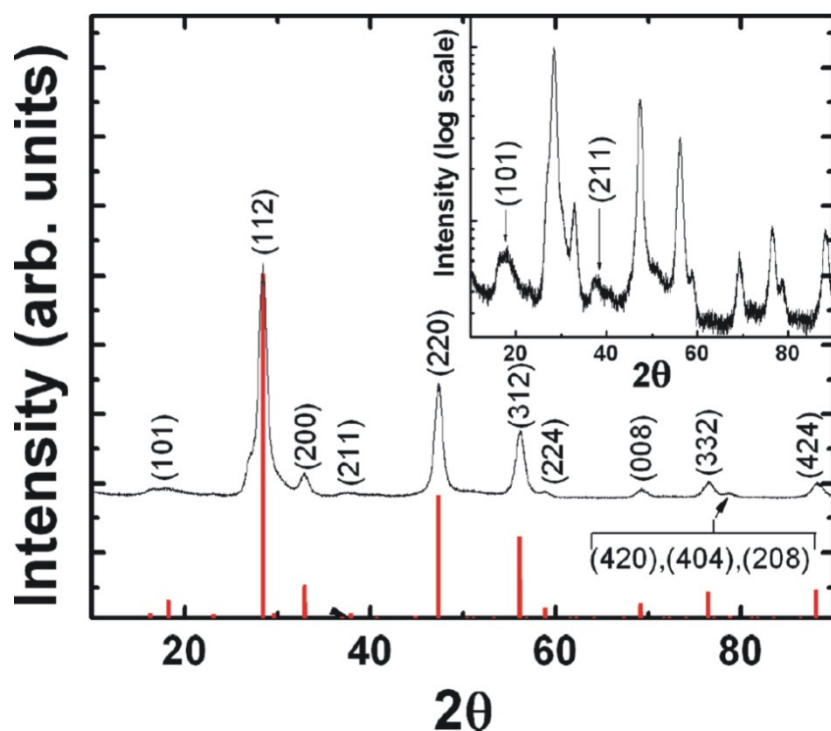


**Figure 2.2.** The typical XRD pattern of CZTS nanoparticles prepared with hot injection method. The red reference pattern was the standard XRD pattern for kesterite CZTS. Inset shows the intensity in log scale. Reprinted from the work of Steinhagen et al.<sup>8</sup>

The crystal structures of CZTS samples can be examined using X-ray diffraction (XRD). Figure 2.2 displays the typical XRD pattern of CZTS nanoparticles.<sup>8</sup> The peaks at  $2\theta$  angle of  $28.5^\circ$ ,  $47.3^\circ$  and  $56.2^\circ$  are prominent and considered as the characteristic peaks

for kesterite CZTS. These three major peaks correspond to the (112), (220) and (312) planes respectively. There are also quite a number of minor peaks which could be found at  $16.4^\circ$ ,  $18.2^\circ$ ,  $23.1^\circ$ ,  $29.7^\circ$ ,  $33.0^\circ$ ,  $37.1^\circ$ ,  $38.0^\circ$ ,  $40.8^\circ$ ,  $45.0^\circ$ ,  $56.9^\circ$ ,  $59.0^\circ$ ,  $64.2^\circ$ ,  $69.3^\circ$ ,  $76.5^\circ$  (for range of  $10^\circ \sim 80^\circ$ ). However, it is sometimes difficult to capture some or even most of above minor peaks due to the low crystallinity of the as-synthesized nanoparticles.

ZnS sphalerite (JCPDS no. 5-0566),  $\text{Cu}_8\text{S}_5$  geerite (JCPDS no. 33-0491) and  $\text{Cu}_2\text{SnS}_3$  (JCPDS no. 27-0198) share very similar crystal structure as well as the XRD pattern with CZTS kesterite. Therefore, in addition to XRD, other characterization techniques are necessary in order to confirm the formation of pure kesterite phase. For example, differential thermal analysis (DTA) was carried out in order to rule out the existence of ZnS and  $\text{Cu}_2\text{SnS}_3$  phases.<sup>9</sup> The fundamentals lying behind are that these materials have different thermal behaviors. ZnS has a phase transition temperature at  $1020^\circ\text{C}$  and will melt at temperature above  $1650^\circ\text{C}$ .<sup>27</sup> The phase transition temperature and the melting temperature of  $\text{Cu}_2\text{SnS}_3$  are  $775^\circ\text{C}$  and  $850^\circ\text{C}$  respectively.<sup>28</sup> By contrast, the quaternary CZTS compound melts at  $990^\circ\text{C}$ .<sup>29</sup> Raman spectroscopy is a more common technique to distinguish CZTS from these compounds.<sup>30, 31</sup> Figure 2.3 shows the Raman spectrum of CZTS under a laser of 488nm reprinted from the work of Fernandes et al.<sup>31</sup> The Raman peaks at the wavelength of  $288\text{ cm}^{-1}$ ,  $338\text{ cm}^{-1}$  and  $368\text{ cm}^{-1}$  could be observed. As a comparison, the Raman peaks for ZnS ( $278$  and  $351\text{ cm}^{-1}$ ),  $\text{Cu}_{2-x}\text{S}$  ( $475\text{ cm}^{-1}$ ) and  $\text{Cu}_2\text{SnS}_3$  ( $298$  and  $356\text{ cm}^{-1}$ ) are distinctly different.<sup>32-34</sup> As a practice, Raman spectroscopy is usually used in combination with XRD to prove the formation of pure CZTS phase.

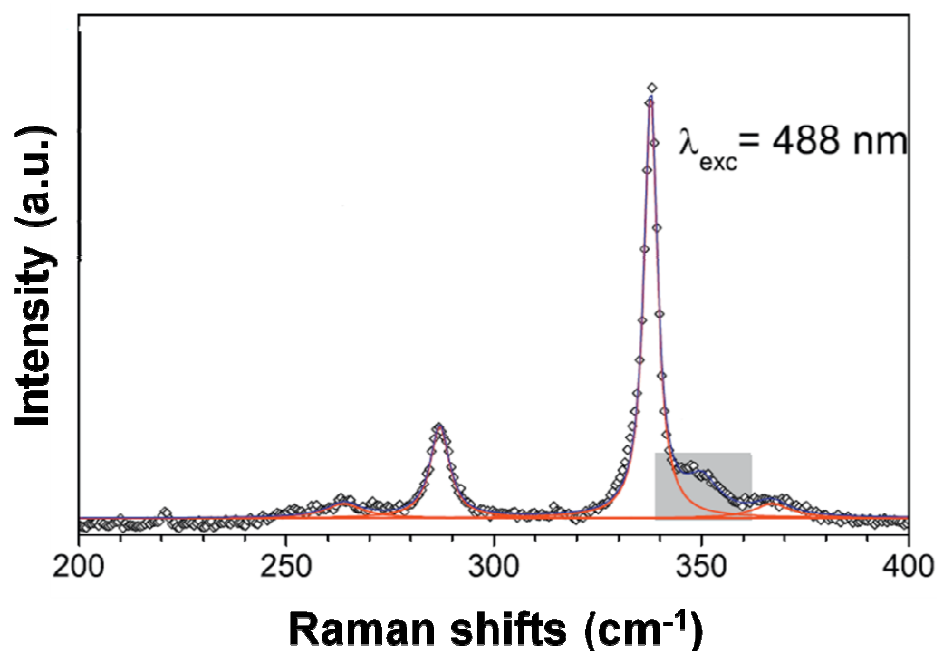


**Figure 2.3.** The Raman spectrum of CZTS under 488 nm laser showing Raman peaks at  $288\text{ cm}^{-1}$ ,  $338\text{ cm}^{-1}$  and  $368\text{ cm}^{-1}$ . The shade area is due to the synergic effect of  $338\text{ cm}^{-1}$  and  $368\text{ cm}^{-1}$ . Reprinted with modification from the work of Fernandes et al.<sup>31</sup>

The composition of CZTS is one key factor to determine the performance of CZTS based TFSCs. In general, a Cu-deficient, Zn-rich composition is favored because it could generate Cu vacancies which are very beneficial for hole transport.<sup>35</sup> Guo et al. employed a precursor combination with S, Cu, Zn and Sn precursors in stoichiometric ratio of 4: 2: 1: 1.<sup>7</sup> The Cu: Zn: Sn: S ratio for as-synthesized CZTS nanoparticles was found to be 2.12: 0.84: 1.06: 4. It could be noticed that the composition of CZTS nanoparticles varies from that of precursors, which is mainly due to the different reactivity associated with Cu, Zn, Sn and S precursors. This composition corresponds to a solar cell efficiency of 0.74%. The composition may be altered by tuning the relative amount of Cu, Zn, Sn and S precursors. With an adjusted recipe that uses less Cu precursor and more Zn precursor, the Cu: Zn: Sn: S ratio could be tuned to 1.31: 0.91: 0.95: 4.<sup>6</sup> The new composition

demonstrated a very high solar cell efficiency of 7.2%, which can be attributed mainly to the Cu-deficient, Zn-rich composition.

The quaternary CZTS has great compositional flexibility, which allows the relative amount of S, Cu, Zn and Sn to be modified in large extent. In CZTS, the cations exist as  $\text{Cu}^+$ ,  $\text{Zn}^{2+}$ ,  $\text{Sn}^{4+}$ , while anions are present in  $\text{S}^{2-}$  form. Therefore, in order to maintain charge neutrality during composition modification, the ratio between Cu and Sn should be kept as 2: 1. Dai et al. reported the synthesis of  $(\text{Cu}_2\text{Sn})_{x/3}\text{Zn}_{1-x}\text{S}$  ( $0 \leq x \leq 0.75$ ) nanoparticles using solvothermal reactions.<sup>36</sup> This chemical formula could be considered as an alloy between ZnS and  $\text{Cu}_2\text{SnS}_3$ . When x value equals to 0.75, the  $\text{Cu}_2\text{ZnSnS}_4$  formula is obtained. Later on, the idea was also demonstrated in an indirect approach. ZnS was coated onto pre-synthesized  $\text{Cu}_2\text{SnS}_3$  nanoparticles, which were then annealed at high temperature to form CZTS nanoparticles.<sup>37</sup>

The energy band gap of near stoichiometric CZTS falls into the range from 1.4 to 1.6 eV.<sup>38, 39</sup> The band gap could be determined with simple UV-vis-NIR measurements. Figure 2.4 presents the reprinted UV-vis-NIR absorption spectrum of CZTS nanocrystals prepared through hot coordinating solvent method.<sup>9</sup> The  $(\alpha h\nu)^2$  vs  $h\nu$  plot was displayed in the inset of Figure 2.4. The band gap could be calculated by drawing a tangent line at the linear region in the  $(\alpha h\nu)^2$  vs  $h\nu$  plot. The cross-section of the tangent line on the  $h\nu$  axis determines the band gap, in this case 1.5 eV. It was reported that CZTS has a band gap highly dependent on the composition. For example, the band gap could be altered from 1.23 eV to 3.48 eV by modifying the relative amount of Cu, Zn and Sn component.<sup>36</sup> During the solar cell fabrication process, Se incorporation is usually

required for high device performance. The substitution of S with Se may also alter the band gap.<sup>40, 41</sup> For near stoichiometric composition ((S+Se): Cu: Zn: Sn:  $\approx$  4: 2: 1: 1), the band gap could be tuned from 0.95 eV for  $[\text{Se}]/([\text{S}]+[\text{Se}]) = 1$  to 1.45 eV for  $[\text{Se}]/([\text{S}]+[\text{Se}]) = 0$ .<sup>42</sup>

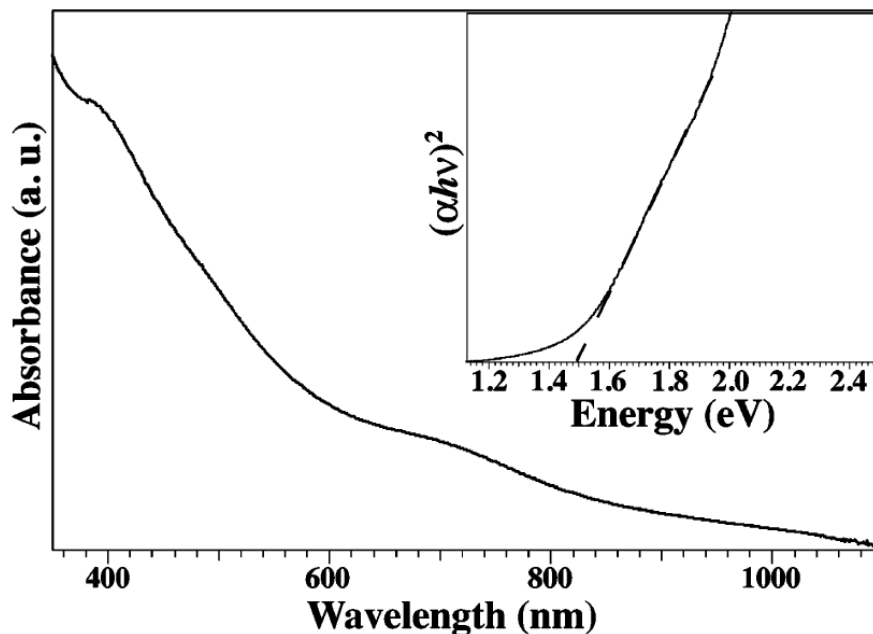


**Figure 2.4.** The typical UV-vis-NIR absorption measurement of CZTS nanocrystals. The inset shows the  $(\alpha h\nu)^2$  vs.  $h\nu$  plot from which band gap was estimated. Reprinted from the work of Riha et al.<sup>9</sup>

The photoresponse of CZTS nanocrystals has also been evaluated through the photoelectrochemical measurements.<sup>43</sup> The as-prepared CZTS nanoparticles were coated onto FTO substrates to form CZTS nanocrystalline thin film. A ligand exchange process was usually carried out on the nanoparticles before film deposition in order to remove the bulky insulating ligands to short chain conducting ligands. Figure 2.5 shows the reprinted J-V curves of the photocurrent response of CZTS nanocrystal thin films. The CZTS nanocrystals display p-type behavior with increased current corresponding to more

negative applied potential. The inset of Figure 2.4 presented the stability test and the photoelectrochemical performance of CZTS nanoparticles film is quite stable.

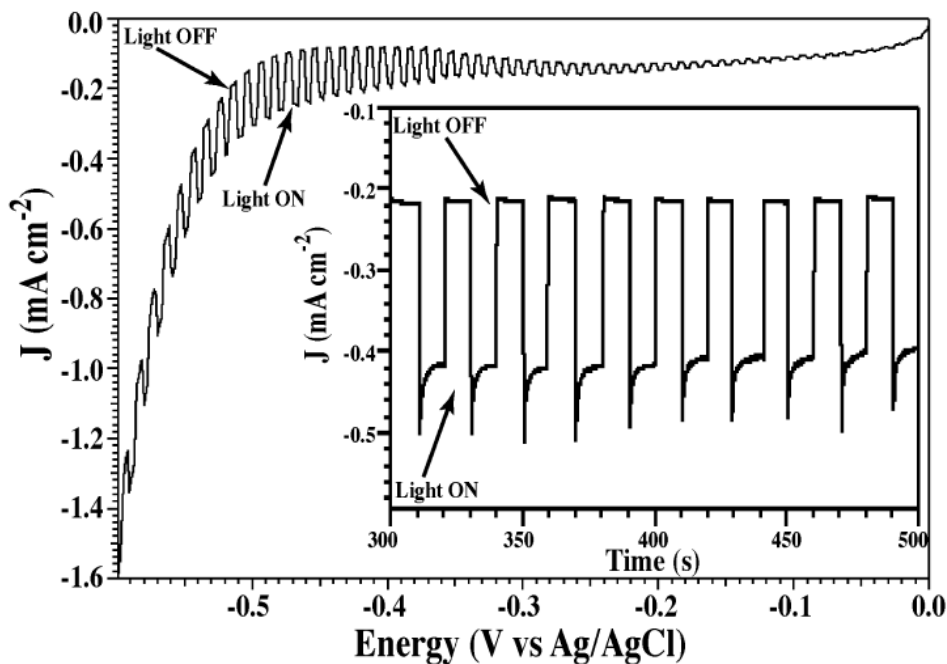


**Figure 2.5.** The photoelectrochemical response of near stoichiometric CZTS nanocrystal thin films. The inset shows the photostability test at negative bias of -500 mV. Reprinted from Riha et al.<sup>43</sup>

### 2.1.3 Size and shape control

The size and shape are two important parameters for nanoparticles because they might determine the properties of the nanoparticles. One classical example could be drawn from CdSe nanocrystals. The absorption edge of CdSe nanocrystals blue shifts as the size increases from 17 Å to 150 Å, showing a decrease in the energy band gap.<sup>44</sup> In this session, we shall review on the size control and shape control of CZTS nanoparticles.

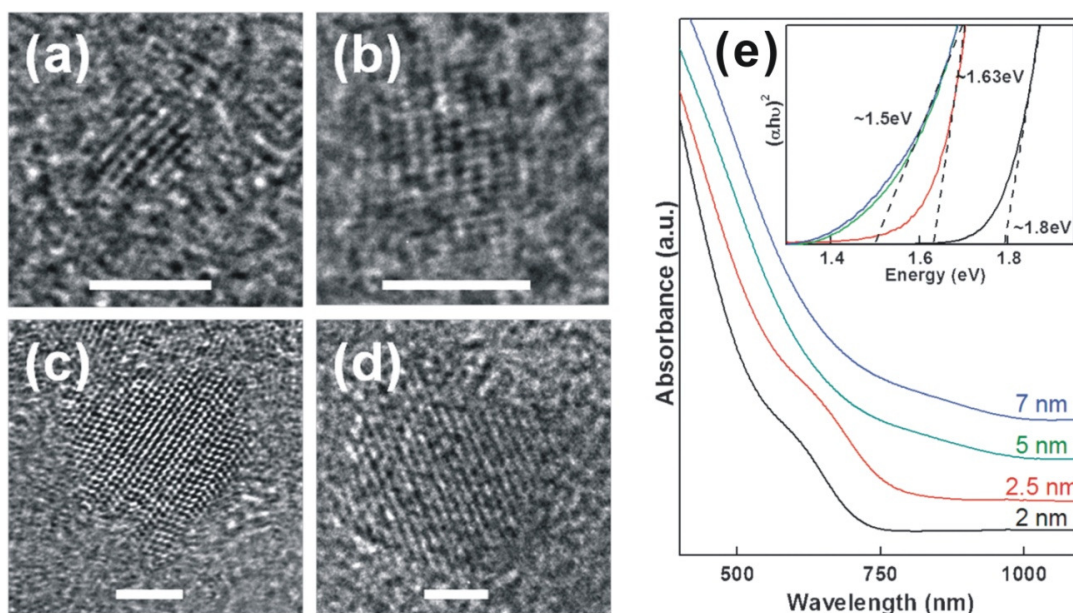


**Figure 2.6.** HRTEM images of synthesized CZTS nanocrystals with diameters of: (a) 2 nm, (b) 2.5 nm, (c) 5 nm, (d) 7 nm. The scale bars in a-d are 2 nm. (e) the UV-vis-NIR absorption measurement CZTS nanoparticles with different size. The inset displays the Tauc plot for the corresponding absorbance curves. Reprinted with modification from the work of Khare et al.<sup>45</sup>

Khare et al. demonstrated the size control of CZTS nanoparticles by tuning the amount of oleylamine and adjusting the reaction temperature.<sup>45</sup> In their work, the Cu, Zn, and Sn diethyl dithiocarbamate complexes were used as the metal precursors. The HRTEM images of show that CZTS nanoparticles with size of 2 nm (Figure 2.6a), 2.5 nm (Figure 2.6b), 5 nm (Figure 2.6c) and 7 nm (Figure 2.6d) were synthesized. Figure 2.6e presents the UV-vis-NIR absorption measurement of CZTS nanoparticles with crystal size corresponding to Figure 2.6a-d. The band gaps are estimated based on the  $(\alpha h\nu)^2$  vs.  $h\nu$  plot in Figure 2.6e to be 1.8 eV (2 nm), 1.63 eV (2.5 nm), 1.5 eV (5 nm) and 1.5 eV (7 nm) respectively. The higher band gap energy than the usual 1.5 eV for particles size of 2 nm and 2.5 nm provides the evidence for quantum confinement.



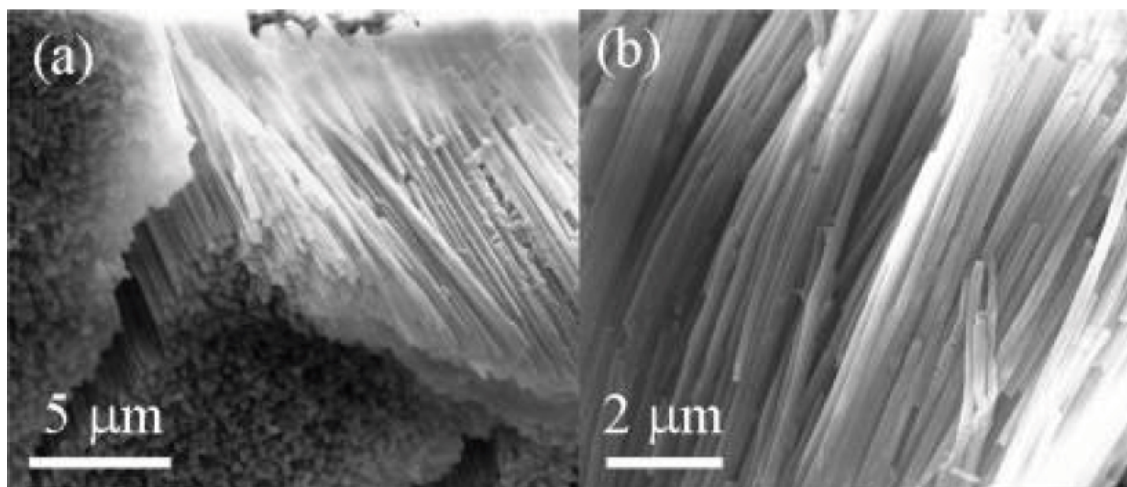


**Figure 2.7.** (a) and (b) the SEM images of the CZTS nanowires array prepared with AAO template. Reprinted from the work of Shi et al.<sup>46</sup>

Shi et al. used the AAO template in their synthesis in an attempt to control the shape of kesterite CZTS nanostructures.<sup>46</sup> The AAO template could be etched off using NaOH solution. Figure 2.7 presents the SEM images of CZTS nanostructures prepared with AAO template. It was found that CZTS nanowires arrays were successfully synthesized. Beside kesterite structure, CZTS can also crystallize into wurtzite structure. The details on the two structures will be discussed in Chapter 4. Several research groups have reported the synthesis of wurtzite structures. Lu et al. prepared wurtzite CZTS nanoparticles in nanoprisms and nanoplates shape.<sup>47</sup> Singh et al. managed to form mono-dispersed wurtzite CZTS nanorods.<sup>48</sup> The size and shape control of CZTS wurtzite are generally easier than the kesterite phase, which is believed to be due to slow reaction dynamics for the formation of wurtzite structure.

Despite the excellent progress of in the synthesis of CZTS nanoparticles as discussed in session 2.1, several critical issues remain unsolved. The effects of experimental

parameters such as temperature, reaction time, solvent and ligand are still not clearly understood. The controlled synthesis of CZTS kesterite and wurtzite as well as their growth mechanisms are not yet reported. In addition, the evaluation of the key properties of the two structures is in urgent need. In this thesis dissertation, the above issues will be studied and discussed in Chapter 3 and Chapter 4.

### **2.2 CZTS Thin Film Deposition Approaches**

The formation of high quality CZTS thin film is crucial for its application. In this part, various CZTS thin film deposition techniques will be reviewed. These techniques are classified into two groups: vacuum deposition techniques and non-vacuum deposition techniques.

#### **2.2.1 Vacuum deposition techniques**

To date, several approaches have been developed for CZTS thin film deposition. Among them, the vacuum deposition approaches have been most intensively studied. As early as 1988, Ito and Nakazawa reported the deposition of CZTS thin film for the first time, which involved the argon beam sputtering.<sup>38</sup> Recent improvements have been made by using sequentially deposited metal layers through either sputtering or evaporation,<sup>3</sup> which are then subjected to high temperature annealing in sulfur-containing environment to form the desired phase.

The atomic ratio of S, Cu, Zn and Sn plays an important role on the solar cell performance. For the sequentially deposited metal layers approach, the ratio of Cu, Zn and Sn can be tuned through modifying the thickness of each metal layer. The Cu-

deficient, Zn-rich samples tend to yield high efficiency devices. High efficiencies are reported within a narrow composition range ( $[\text{Cu}]/([\text{Zn}]+[\text{Sn}]) \sim 0.9$ ,  $[\text{Zn}]/[\text{Sn}] \sim 1.25$ ).<sup>35</sup> The knowledge of the effect of atomic ratio on device performance, together with the optimization of annealing processes, has led to great improvements on the device performance. An encouraging efficiency of 6.77% has been achieved by Katagiri group with open circuit voltage ( $V_{\text{oc}}$ ) of 610 mV, short circuit current ( $J_{\text{sc}}$ ) of  $17.9 \text{ mA/cm}^2$ , and fill factor (FF) of 62%.<sup>49</sup> Later on, Shin et al. pushed the efficiency to an even higher value of 8.4%, which is by far the highest efficiency achieved using a pure sulfide CZTS.<sup>50</sup>

### 2.2.2 Non-vacuum deposition techniques

Although vacuum based approaches can offer high quality and well controlled thin film, they are often less favored for mass production due to the high fabrication cost. Therefore, there is a trend to replace the vacuum deposition techniques with low-cost solution-processable fabrication methods including electrodeposition, spray pyrolysis and “ink”-based approach.

Electrodeposition has been adopted in the synthesis of CZTS thin films. The early work of electrodeposition of CZTS was based on electroplating of Cu-, Zn- and Sn- stacked metal layers, which was then annealed in a  $\text{H}_2\text{S}$  gas environment.<sup>51</sup> Some examples of sequence of metal layers include Zn/Sn/Cu and Zn/Cu/Sn/Cu stacking. As for Zn/Cu/Sn/Cu stacking, an improve process employs aqueous KCN solution to etch away Cu-rich phase, yielding a device efficiency of 3.2%.<sup>52</sup> Later, the co-electrodeposition of Cu-, Zn- and Sn- metal precursors has been developed by precisely tuning of the

concentration of each precursors.<sup>53</sup> The most recent achievement was a single-step deposition of the metal precursors and sulfur precursor.<sup>54</sup>

Spray pyrolysis is also a low-cost solution-processable fabrication approach. Typically, the precursor solution contains Cu, Zn and Sn chlorides in stoichiometric ratio, and also an excess of thiourea to compensate sulfur loss and prevent oxidation. The proposed chemical reaction was described in equation 1.<sup>55</sup>



The “ink”-based approach has been of particular interest in recent years. It allows the use of cost-effective, high-throughput deposition method including printing, spin-coating and spraying.<sup>56</sup> The “ink” can be solution, nanoparticles dispersion and mixed solution-particle precursors.

Sol-gel method has been demonstrated in the preparations of CZTS thin film.<sup>57</sup> The precursor contains Cu-, Zn-, Sn- salts, 2-methoxyethanol solvents and monoethanolamine stabilizer. Subsequently, the film is annealed in H<sub>2</sub>S environment to form CZTS. In another contribution, pyridine was used as the solvent and thioacetamide was used as the sulfur source.<sup>58</sup> The as-prepared film then underwent thermal treatment to form CZTS film.

Besides the pure solution base approaches, the quaternary CZTS nanocrystals ink has also been investigated.<sup>7,9</sup> Figure 2.8 illustrate the general overview of the nanocrystal ink approach which is reprinted from Bucherl et al.<sup>4</sup> In this method, the nanocrystals were first synthesized in solution, and purified through centrifuge processes. The as-prepared

nanocrystals were then dissolved in proper solvent to form the nanocrystal ink. Subsequently, the ink could be deposited onto a substrate using various solution deposition techniques including blade coating, spin-coating and spraying. The nanoparticles thin film was then annealed or selenized to form dense absorber layer. Then the solar cells could be fabricated using the as-prepared absorber layer. As for CZTS, the CZTS nanocrystals dispersion is commonly used as the ink. However, the choices of ink are not limited to CZTS nanocrystals only. Recently, Cao et al. demonstrated high efficiency CZTSSe solar cells making use of well dispersed binary and ternary sulfides nanoparticles.<sup>13</sup>

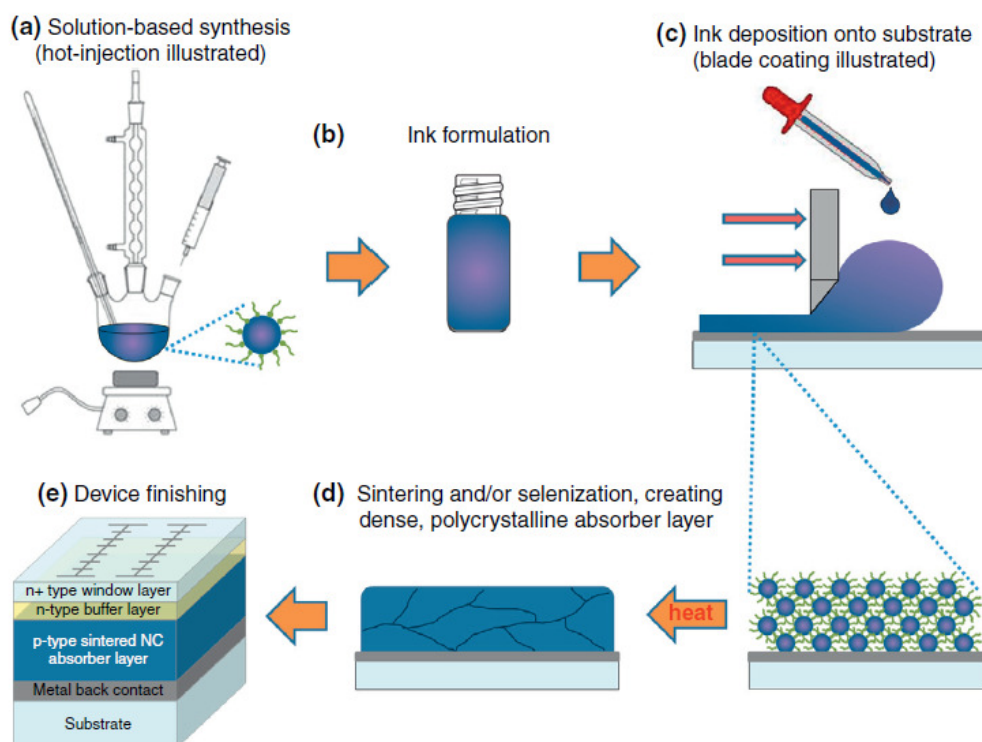


**Figure 2.8.** Overview of solar cell fabrication using nanoparticles “ink” approach. (a) synthesis of nanoparticles, (b) nanoparticles ink formation, (c) film deposition, (d) heat treatment of as deposited film and (e) Device fabrication. Reprinted from the work of Bucherl et al.<sup>4</sup>

In addition to the above two ink approaches, a new type of inks containing both solution and nanoparticles has been developed. Todorov et al. prepared the  $\text{Cu}_2\text{ZnSn}(\text{S},\text{Se})_4$  (CZTSSe) absorber layer using ink comprised of Cu-, Sn- sulfide /selenide solution in hydrazine and readily dispersible particle-based Zn-sulfide/selenide precursor in hydrazine.<sup>59</sup> Thin film solar cells using this approach have reached a very high PCE of 9.66%. Recently, the efficiency has been increased to more than 11% using such method.<sup>60</sup>

The ink-based approaches are very promising considering their high device performance. However, the use of expensive, toxic solvents (e.g. oleylamine for CZTS nanocrystals ink, hydrazine for hybrid solution-particles ink) may hinder their large scale production. In this regard, inks which are low-cost and environmentally friendly are highly desirable. In this thesis dissertation, the novel ink based on binary sulfides nanoparticles which makes use of greener solvents such as water and ethanol is developed and will be discussed in Chapter 5.

### 2.3 CZTSSe Based Solar Cells

The applications of CZTS have been mainly focused on TFSCs. Until now, the efficiency has been increased to 8.4% for pure sulfide system and 11.1% for mixed sulfur-selenium system.<sup>50, 60</sup> In this part, the recently development and progress of CZTSSe TFSCs will be reviewed.

The composition of CZTS is crucial for the device performance. Figure 2.9 shows the reprinted ternary phase diagram of CZTS at equilibrium temperature of 400 °C.<sup>61</sup> It provides a guideline to understand the formation of CZTS as well as secondary phases,

although a change in the equilibrium temperature might lead to slight variation to the phase diagram. As shown in Figure 2.9, the quaternary CZTS phase is stable within a small compositional range where Cu: Zn: Sn ratio is around 2: 1: 1. A number of secondary phases including binary sulfides ( $\text{Cu}_2\text{S}$ ,  $\text{ZnS}$ ), ternary sulfides ( $\text{Cu}_2\text{SnS}_3$ ,  $\text{Cu}_4\text{SnS}_4$ ) as well as quaternary sulfides ( $\text{Cu}_2\text{ZnSn}_3\text{S}_8$ ) may form depending on the ratio of Cu: Zn: Sn. The above secondary phases are considered to be harmful to the performance of CZTS solar cells. Therefore, the composition of CZTS should be adjusted cautiously.

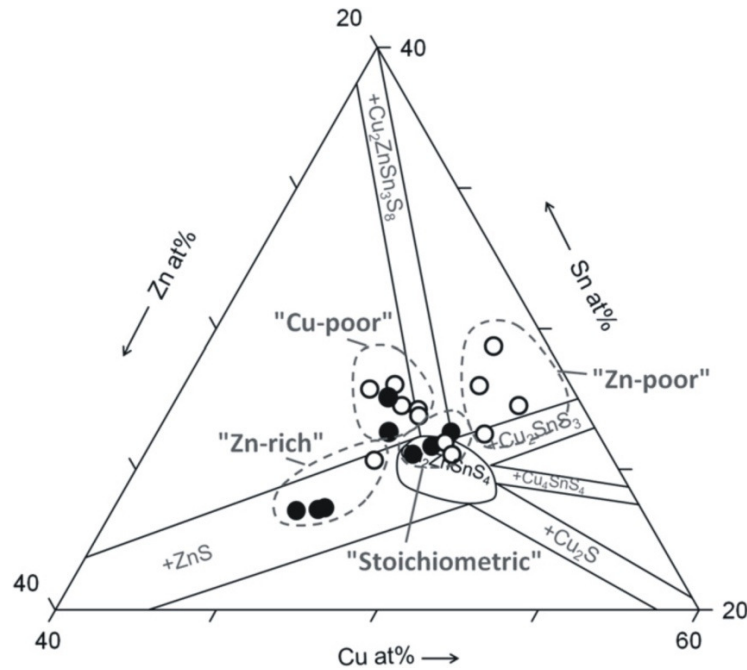


**Figure 2.9.** Ternary phase diagram of CZTS prepared by sulfidizing stacked metal layers. Reprinted from the work of Platzer-Björkman et al.<sup>61</sup>

Although the overall ratio of Cu: Zn: Sn could be managed easily, it might be difficult to avoid localized secondary phases mainly due to the non-uniform mixing of precursors. In such case, the localized secondary phases might lead to the poor device performance. To

tackle this issue, the chemical etching processes are usually carried out for CZTS thin film. The KCN etching was previously proved to enhance the performance of  $\text{CuIn}_x\text{Ga}_{1-x}(\text{S}, \text{Se})_2$  solar cells.<sup>62</sup> It was also adopted to eliminate the Cu-rich phases such as  $\text{Cu}_2\text{S}$ ,  $\text{Cu}_2\text{SnS}_3$  in CZTS thin film.<sup>63</sup> The HCl etching was reported to be effective in removing ZnS. The solar cells demonstrated an increase in efficiency from 2.7% to 5.2% with HCl etching.<sup>64</sup>

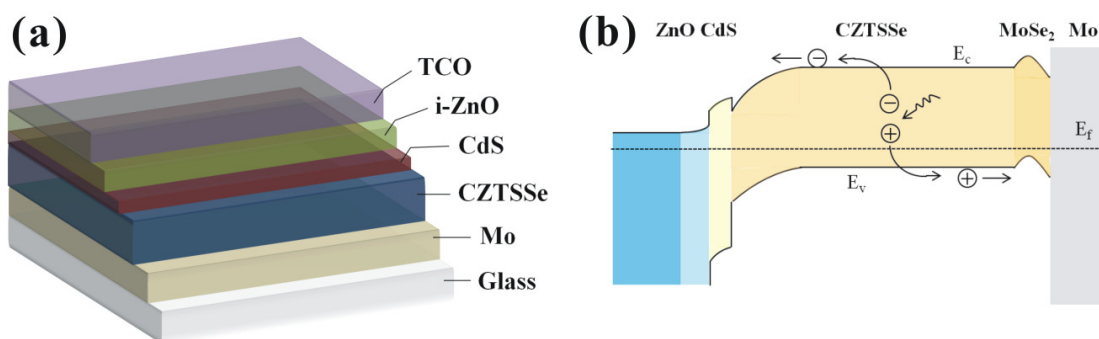


**Figure 2.10.** (a) the architecture of CZTSSe based TFSCs and (b) its energy band diagram under zero-bias.

Figure 2.10a shows the typical structure of CZTSSe based TFSCs with Glass/Mo/CZTSSe/CdS/i-ZnO/TCO architecture. Sodium lime glass is usually used as the substrate. And the 1  $\mu\text{m}$  thick Mo electrode is deposited using sputtering. Subsequently, the CZTS absorber layer can be coated through various thin film deposition techniques as discussed in session 2.2. The thickness of CZTS layer may vary from a few hundred nanometers to several micrometers. Sometimes the CZTS layer undergoes the selenization process to form dense CZTSSe thin film. After that, the buffer layer of 50 nm CdS will be deposited on top of CZTSSe layer through chemical bath deposition technique. Following that are 50 nm intrinsic zinc oxide (i-ZnO) layer and 450 nm



transparent conducting oxide (TCO) layer, which are sequentially deposited by radio-frequency sputtering. The Al-doped ZnO (AZO) and In-doped SnO<sub>2</sub> (ITO) are two TCO materials that are commonly used. Lastly, the top contact of a 500 nm thick Ni/Al is deposited using thermal evaporation.

The energy band diagram of CZTSSe TFSC is illustrated in Figure 2.10b. When light is shining through front contact onto CZTSSe absorber layer, photons with energy larger than the band gap energy of CZTSSe will be absorbed. This promotes one electron to jump from valence band to conduction band, which creates an electron-hole pair. The excited electrons will then move to anode (front metal contact) and holes move to cathode (Mo layer) according to the internal electric field. The complete circuit will be formed when the two electrodes are connected.

Bag et al. reported a high efficiency CZTSSe TFSC using hydrazine method.<sup>65</sup> Figure 2.11a shows the reprinted IV curve of as-prepared CZTS thin film solar cell, which has efficiency ( $\eta$ ) of 10.1% ( $J_{sc} = 38.7 \text{ mA/cm}^2$ ,  $V_{oc} = 422.8 \text{ mV}$ ,  $FF = 61.9\%$ ). Figure 2.11b presents the external quantum efficiency (EQE), which is very high (more than 80%) at wavelength between 500 to 1000 nm. The main reason for the success of the hydrazine approach could be attributed to the high-quality absorber layer. As shown in Figure 2.12a, the CZTSSe film consists of large grain penetrating from the top to Mo electrode. The large-grain structure is highly beneficial for the transport of charge carriers due to the low density of grain boundaries. The EDX line scan in Figure 2.12b shows that the composition is very uniform across the CZTSSe film.

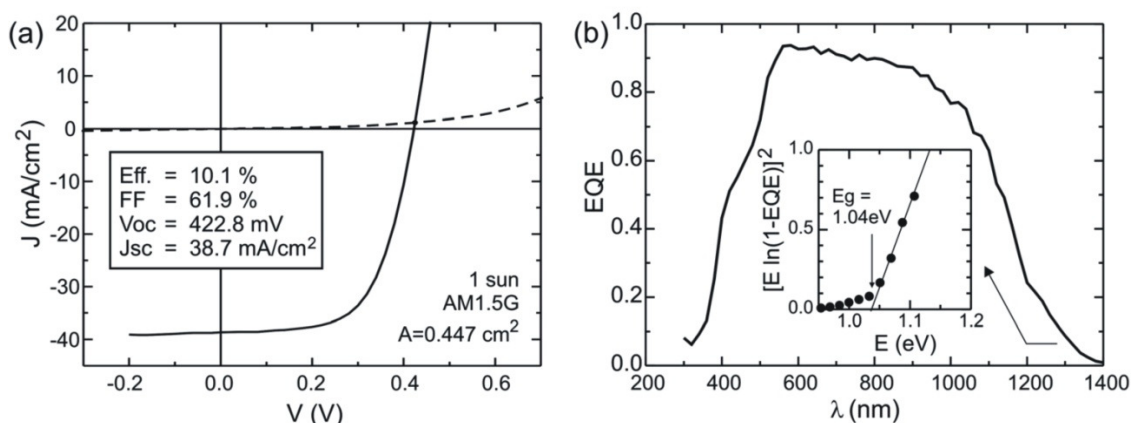


**Figure 2.11.** (a) J–V curve under light and dark condition. (b) EQE curve of the cell. Inset: band gap determination of the cell from the EQE data. Reprinted from the work of Bag et al.<sup>65</sup>

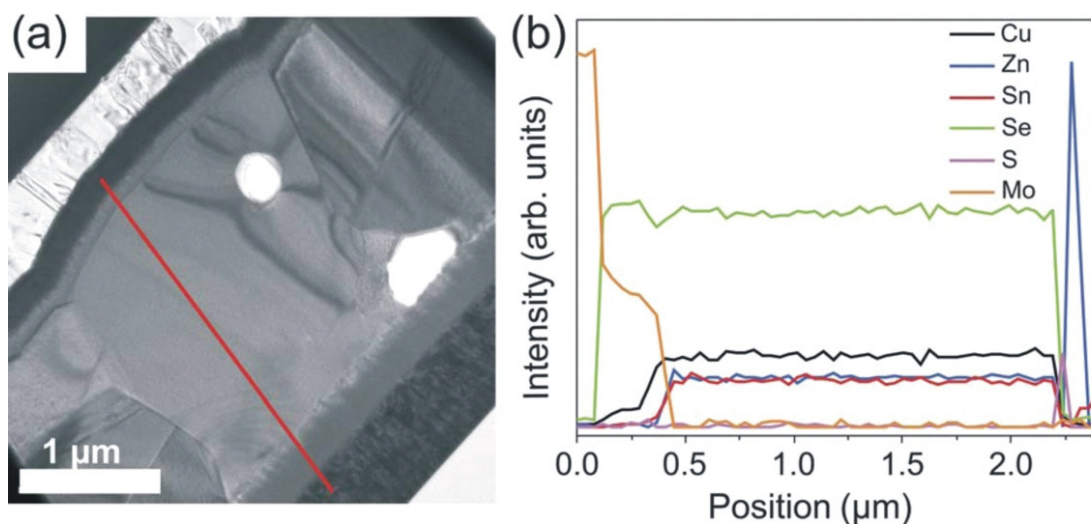


**Figure 2.12.** Cross-sectional (a) TEM image and (b) EDX line scan of CZTSSe solar cell prepared using hydrazine method. Reprinted from the work of Bag et al.<sup>65</sup>

Besides thin film solar cells, CZTS may also be used in other types of solar cells. For example, Saha et al. fabricated CZTS/PCBM bilayer solar cells with an efficiency of  $0.9\%$ .<sup>66</sup> Dai et al. used CZTS nanocrystals as sensitizer in the quantum dot sensitized solar cells (QDSSC).<sup>36</sup> In dye sensitized solar cells (DSSC), the use of CZTS

nanocrystals thin film to replace precious Pt as the counter electrode has also been reported.<sup>67</sup>

### References

1. Katagiri, H., Cu<sub>2</sub>ZnSnS<sub>4</sub> thin film solar cells. *Thin Solid Films* **2005**, 480-481, (0), 426-432.
2. Katagiri, H.; Saitoh, K.; Washio, T.; Shinohara, H.; Kurumadani, T.; Miyajima, S., Development of thin film solar cell based on Cu<sub>2</sub>ZnSnS<sub>4</sub> thin films. *Solar Energy Materials and Solar Cells* **2001**, 65, (1-4), 141-148.
3. Mitzi, D. B.; Gunawan, O.; Todorov, T. K.; Wang, K.; Guha, S., The path towards a high-performance solution-processed kesterite solar cell. *Solar Energy Materials and Solar Cells* **2011**, 95, (6), 1421-1436.
4. Bucherl, C. N.; Oleson, K. R.; Hillhouse, H. W., Thin film solar cells from sintered nanocrystals. *Current Opinion in Chemical Engineering* **2013**, 2, (2), 168-177.
5. Stolle, C. J.; Harvey, T. B.; Korgel, B. A., Nanocrystal photovoltaics: a review of recent progress. *Current Opinion in Chemical Engineering* **2013**, 2, (2), 160-167.
6. Guo, Q.; Ford, G. M.; Yang, W.-C.; Walker, B. C.; Stach, E. A.; Hillhouse, H. W.; Agrawal, R., Fabrication of 7.2% efficient CZTSSe solar cells using CZTS nanocrystals. *Journal of the American Chemical Society* **2010**, 132, (49), 17384-17386.
7. Guo, Q.; Hillhouse, H. W.; Agrawal, R., Synthesis of Cu<sub>2</sub>ZnSnS<sub>4</sub> nanocrystal ink and its use for solar cells. *Journal of the American Chemical Society* **2009**, 131, (33), 11672-11673.
8. Steinhagen, C.; Panthani, M. G.; Akhavan, V.; Goodfellow, B.; Koo, B.; Korgel, B. A., Synthesis of Cu<sub>2</sub>ZnSnS<sub>4</sub> nanocrystals for use in low-cost photovoltaics. *Journal of the American Chemical Society* **2009**, 131, (35), 12554-12555.
9. Riha, S. C.; Parkinson, B. A.; Prieto, A. L., Solution-Based Synthesis and Characterization of Cu<sub>2</sub>ZnSnS<sub>4</sub> Nanocrystals. *Journal of the American Chemical Society* **2009**, 131, (34), 12054-12055.
10. Kameyama, T.; Osaki, T.; Okazaki, K.-i.; Shibayama, T.; Kudo, A.; Kuwabata, S.; Torimoto, T., Preparation and photoelectrochemical properties of densely immobilized Cu<sub>2</sub>ZnSnS<sub>4</sub> nanoparticle films. *Journal of Materials Chemistry* **2010**, 20, (25), 5319-5324.

11. Shavel, A.; Cadavid, D.; Ibanez, M.; Carrete, A.; Cabot, A., Continuous production of  $\text{Cu}_2\text{ZnSnS}_4$  nanocrystals in a flow reactor. *Journal of the American Chemical Society* **2012**, 134, (3), 1438-1441.
12. Zhou, Y.-L.; Zhou, W.-H.; Du, Y.-F.; Li, M.; Wu, S.-X., Sphere-like kesterite  $\text{Cu}_2\text{ZnSnS}_4$  nanoparticles synthesized by a facile solvothermal method. *Materials Letters* **2011**, 65, (11), 1535-1537.
13. Cao, M.; Shen, Y., A mild solvothermal route to kesterite quaternary  $\text{Cu}_2\text{ZnSnS}_4$  nanoparticles. *Journal of Crystal Growth* **2011**, 318, (1), 1117-1120.
14. Xiuying Wang, Z. S., Cong Shao, Daniel M Boye and Jialong Zhao, A facile and general approach to polynary semiconductor nanocrystals via a modified two-phase method. *Nanotechnology* **2011**, 22.
15. Wang, C. C., Chen; Cao, Yun; Fang, Wei; Zhao, Lijuan; Xu, Xiaofeng Synthesis of  $\text{Cu}_2\text{ZnSnS}_4$  nanocrystallines by a hydrothermal route. *Japanese Journal of Applied Physics* **2011**, 50, (6).
16. Zhao, Y.; Zhou, W.-H.; Jiao, J.; Zhou, Z.-J.; Wu, S.-X., Aqueous synthesis and characterization of hydrophilic  $\text{Cu}_2\text{ZnSnS}_4$  nanocrystals. *Materials Letters* **2013**, 96, (0), 174-176.
17. Murray, C. B.; Norris, D. J.; Bawendi, M. G., Synthesis and characterization of nearly monodisperse CdE (E = sulfur, selenium, tellurium) semiconductor nanocrystallites. *Journal of the American Chemical Society* **1993**, 115, (19), 8706-8715.
18. Yu, J. H.; Joo, J.; Park, H. M.; Baik, S.-I.; Kim, Y. W.; Kim, S. C.; Hyeon, T., Synthesis of quantum-sized cubic ZnS nanorods by the oriented attachment mechanism. *Journal of the American Chemical Society* **2005**, 127, (15), 5662-5670.
19. Hines, M. A.; Scholes, G. D., Colloidal PbS nanocrystals with size-tunable near-infrared emission: observation of post-synthesis self-narrowing of the particle size distribution. *Advanced Materials* **2003**, 15, (21), 1844-1849.
20. Tang, J.; Hinds, S.; Kelley, S. O.; Sargent, E. H., Synthesis of colloidal  $\text{CuGaSe}_2$ ,  $\text{CuInSe}_2$ , and  $\text{Cu(InGa)Se}_2$  nanoparticles. *Chemistry of Materials* **2008**, 20, (22), 6906-6910.
21. Yin, Y.; Alivisatos, A. P., Colloidal nanocrystal synthesis and the organic-inorganic interface. *Nature* **2005**, 437, (7059), 664-670.
22. de Mello Donegá, C.; Liljeroth, P.; Vanmaekelbergh, D., Physicochemical Evaluation of the Hot-Injection Method, a Synthesis Route for Monodisperse Nanocrystals. *Small* **2005**, 1, (12), 1152-1162.

23. Walsh, A.; Chen, S.; Wei, S.-H.; Gong, X.-G., Kesterite thin-film solar cells: advances in materials modelling of  $\text{Cu}_2\text{ZnSnS}_4$ . *Advanced Energy Materials* **2012**, 2, (4), 400-409.
24. Chen, S.; Gong, X. G.; Walsh, A.; Wei, S.-H., Crystal and electronic band structure of  $\text{Cu}_2\text{ZnSnX}_4$  (X = S and Se) photovoltaic absorbers: First-principles insights. *Applied Physics Letters* **2009**, 94, (4), 041903-3.
25. Taylor S. R., M. S. M., The continental crust: its composition and evolution: an examination of the geochemical record preserved in sedimentary rocks. *Blackwell Scientific Publication* **1985**, Oxford, 1-312.
26. Kasuya, M., Recent epidemiological studies on itai-itai disease as a chronic cadmium poisoning in Japan *Water Science & Technology* **2000**, 42.
27. Qadri, S. B.; Skelton, E. F.; Hsu, D.; Dinsmore, A. D.; Yang, J.; Gray, H. F.; Ratna, B. R., Size-induced transition-temperature reduction in nanoparticles of ZnS. *Physical Review B* **1999**, 60, (13), 9191-9193.
28. Fiechter, S.; Martinez, M.; Schmidt, G.; Henrion, W.; Tomm, Y., Phase relations and optical properties of semiconducting ternary sulfides in the system Cu-Sn-S. *Journal of Physics and Chemistry of Solids* **2003**, 64, (9-10), 1859-1862.
29. Matsushita, H.; Ichikawa, T.; Katsui, A., Structural, thermodynamical and optical properties of  $\text{Cu}_2\text{-II-IV-VI}_4$  quaternary compounds. *Journal of Materials Science* **2005**, 40, (8), 2003-2005.
30. Cheng, A. J.; Manno, M.; Khare, A.; Leighton, C.; Campbell, S. A.; Aydil, E. S., Imaging and phase identification of  $\text{Cu}_2\text{ZnSnS}_4$  thin films using confocal Raman spectroscopy. *Journal of Vacuum Science & Technology A: Vacuum, Surfaces, and Films* **2011**, 29, (5), 051203-11.
31. Fernandes, P. A.; Salome, P. M. P.; da Cunha, A. F., Study of polycrystalline  $\text{Cu}_2\text{ZnSnS}_4$  films by Raman scattering. *Journal of Alloys and Compounds* **2011**, 509, (28), 7600-7606.
32. Cheng, Y. C.; Jin, C. Q.; Gao, F.; Wu, X. L.; Zhong, W.; Li, S. H.; Chu, P. K., Raman scattering study of zinc blende and wurtzite ZnS. *Journal of Applied Physics* **2009**, 106, (12), 123505-5.
33. Fernandes P. A., S. P. M. P., Cunha, A. F. , A study of ternary  $\text{Cu}_2\text{SnS}_3$  and  $\text{Cu}_3\text{SnS}_4$  thin films prepared by sulfurizing stacked metal precursors *Journal of Physics D: Applied Physics* **2010**, 43.

34. Munce, C. G.; Parker, G. K.; Holt, S. A.; Hope, G. A., A Raman spectroelectrochemical investigation of chemical bath deposited  $\text{Cu}_x\text{S}$  thin films and their modification. *Colloids and Surfaces A: Physicochemical and Engineering Aspects* **2007**, 295, (1-3), 152-158.
35. Katagiri H., J. K., Tahara M., Araki H. and Oishi K. , The influence of the composition ratio on CZTS-based thin film solar cells. *MRS Proceedings* **2009**.
36. Dai, P.; Shen, X.; Lin, Z.; Feng, Z.; Xu, H.; Zhan, J., Band-gap tunable  $(\text{Cu}_2\text{Sn})_{x/3}\text{Zn}_{1-x}\text{S}$  nanoparticles for solar cells. *Chemical Communications* **2010**, 46, (31), 5749-5751.
37. Park, J.; Song, M.; Jung, W. M.; Lee, W. Y.; Kim, H.; Kim, Y.; Hwang, C.; Shim, I.-W., Syntheses of  $\text{Cu}_2\text{SnS}_3$  and  $\text{Cu}_2\text{ZnSnS}_4$  nanoparticles with tunable Zn/Sn ratios under multibubble sonoluminescence conditions. *Dalton Transactions* **2013**, 42, (29), 10545-10550.
38. Kentaro Ito, T. N., Electrical and optical properties of stannite-type quaternary semiconductor thin films. *The Japan Society of Applied Physics* **1988**, 27.
39. Ennaoui, A.; Lux-Steiner, M.; Weber, A.; Abou-Ras, D.; Kotschau, I.; Schock, H. W.; Schurr, R.; Holzinger, A.; Jost, S.; Hock, R.; Vob, T.; Schulze, J.; Kirbs, A.,  $\text{Cu}_2\text{ZnSnS}_4$  thin film solar cells from electroplated precursors: Novel low-cost perspective. *Thin Solid Films* **2009**, 517, (7), 2511-2514.
40. Fan, F.-J.; Wu, L.; Gong, M.; Liu, G.; Wang, Y.-X.; Yu, S.-H.; Chen, S.; Wang, L.-W.; Gong, X.-G., Composition- and band-gap-tunable synthesis of wurtzite-derived  $\text{Cu}_2\text{ZnSn}(\text{S}_{1-x}\text{Se}_x)_4$  nanocrystals: theoretical and experimental insights. *ACS Nano* **2013**, 7, (2), 1454-1463.
41. Riha, S. C.; Parkinson, B. A.; Prieto, A. L., Compositionally tunable  $\text{Cu}_2\text{ZnSn}(\text{S}_{1-x}\text{Se}_x)_4$  nanocrystals: probing the effect of Se-inclusion in mixed chalcogenide thin films. *Journal of the American Chemical Society* **2011**, 133, (39), 15272-15275.
42. Haight, R.; Barkhouse, A.; Gunawan, O.; Shin, B.; Copel, M.; Hopstaken, M.; Mitzi, D. B., Band alignment at the  $\text{Cu}_2\text{ZnSn}(\text{S}_x\text{Se}_{1-x})_4/\text{CdS}$  interface. *Applied Physics Letters* **2011**, 98, (25), 253502-3.
43. Riha, S. C.; Fredrick, S. J.; Sambur, J. B.; Liu, Y.; Prieto, A. L.; Parkinson, B. A., Photoelectrochemical characterization of nanocrystalline thin-film  $\text{Cu}_2\text{ZnSnS}_4$  photocathodes. *ACS Applied Materials & Interfaces* **2010**, 3, (1), 58-66.
44. Murray, C. B.; Kagan, C. R.; Bawendi, M. G., Synthesis and characterization of monodisperse nanocrystals and close-packed nanocrystal assemblies. *Annual Review of Materials Science* **2000**, 30, (1), 545-610.

45. Khare, A.; Wills, A. W.; Ammerman, L. M.; Norris, D. J.; Aydil, E. S., Size control and quantum confinement in  $\text{Cu}_2\text{ZnSnS}_4$  nanocrystals. *Chemical Communications* **2011**, 47, (42), 11721-11723.
46. Shi, L.; Pei, C.; Xu, Y.; Li, Q., Template-directed synthesis of ordered single-crystalline nanowires arrays of  $\text{Cu}_2\text{ZnSnS}_4$  and  $\text{Cu}_2\text{ZnSnSe}_4$ . *Journal of the American Chemical Society* **2011**, 133, (27), 10328-10331.
47. Lu, X.; Zhuang, Z.; Peng, Q.; Li, Y., Wurtzite  $\text{Cu}_2\text{ZnSnS}_4$  nanocrystals: a novel quaternary semiconductor. *Chemical Communications* **2011**, 47, (11), 3141-3143.
48. Singh, A.; Geaney, H.; Laffir, F.; Ryan, K. M., Colloidal synthesis of wurtzite  $\text{Cu}_2\text{ZnSnS}_4$  nanorods and their perpendicular assembly. *Journal of the American Chemical Society* **2012**, 134, (6), 2910-2913.
49. Hironori Katagiri, K. J., Satoru Yamada, Tsuyoshi Kamimura, Win Shwe Maw, Tatsuo Fukano, Tadashi Ito, and Tomoyoshi Motohiro, Enhanced conversion efficiencies of  $\text{Cu}_2\text{ZnSnS}_4$ -based thin film solar cells by using preferential etching technique. *Appl. Phys. Express* **2008**, 1.
50. Shin, B.; Gunawan, O.; Zhu, Y.; Bojarczuk, N. A.; Chey, S. J.; Guha, S., Thin film solar cell with 8.4% power conversion efficiency using an earth-abundant  $\text{Cu}_2\text{ZnSnS}_4$  absorber. *Progress in Photovoltaics: Research and Applications* **2011**, 21, (1), 72-76.
51. Scragg, J. J.; Dale, P. J.; Peter, L. M.; Zoppi, G.; Forbes, I., New routes to sustainable photovoltaics: evaluation of  $\text{Cu}_2\text{ZnSnS}_4$  as an alternative absorber material. *physica status solidi (b)* **2008**, 245, (9), 1772-1778.
52. Scragg, J. J.; Berg, D. M.; Dale, P. J., A 3.2% efficient Kesterite device from electrodeposited stacked elemental layers. *Journal of Electroanalytical Chemistry* **2010**, 646, (1-2), 52-59.
53. Araki, H.; Kubo, Y.; Jimbo, K.; Maw, W. S.; Katagiri, H.; Yamazaki, M.; Oishi, K.; Takeuchi, A., Preparation of  $\text{Cu}_2\text{ZnSnS}_4$  thin films by sulfurization of co-electroplated Cu-Zn-Sn precursors. *physica status solidi (c)* **2009**, 6, (5), 1266-1268.
54. Pawar, S. M.; Pawar, B. S.; Moholkar, A. V.; Choi, D. S.; Yun, J. H.; Moon, J. H.; Kolekar, S. S.; Kim, J. H., Single step electrosynthesis of  $\text{Cu}_2\text{ZnSnS}_4$  (CZTS) thin films for solar cell application. *Electrochimica Acta* **2010**, 55, (12), 4057-4061.
55. Kamoun, N.; Bouzouita, H.; Rezig, B., Fabrication and characterization of  $\text{Cu}_2\text{ZnSnS}_4$  thin films deposited by spray pyrolysis technique. *Thin Solid Films* **2007**, 515, (15), 5949-5952.
56. Todorov, T.; Mitzi, D. B., Direct liquid voating of vhalcopyrite light-absorbing layers for photovoltaic devices. *European Journal of Inorganic Chemistry* **2009**, 2010, (1), 17-28.



57. Tanaka, K.; Moritake, N.; Uchiki, H., Preparation of thin films by sulfurizing sol-gel deposited precursors. *Solar Energy Materials and Solar Cells* **2007**, 91, (13), 1199-1201.
58. Fischereder, A.; Rath, T.; Haas, W.; Amenitsch, H.; Albering, J.; Meischler, D.; Larissegger, S.; Edler, M.; Saf, R.; Hofer, F.; Trimmel, G., Investigation of  $\text{Cu}_2\text{ZnSnS}_4$  formation from metal salts and thioacetamide. *Chemistry of Materials* **2010**, 22, (11), 3399-3406.
59. Todorov, T. K.; Reuter, K. B.; Mitzi, D. B., High-efficiency solar cell with earth-abundant liquid-processed absorber. *Advanced Materials* **2010**, 22, (20), E156-E159.
60. Todorov, T. K.; Tang, J.; Bag, S.; Gunawan, O.; Gokmen, T.; Zhu, Y.; Mitzi, D. B., Beyond 11% efficiency: characteristics of state-of-the-art  $\text{Cu}_2\text{ZnSn}(\text{S},\text{Se})_4$  solar cells. *Advanced Energy Materials* **2012**, 3, (1), 34-38.
61. Platzer-Bjorkman, C.; Scragg, J.; Flammersberger, H.; Kubart, T.; Edoff, M., Influence of precursor sulfur content on film formation and compositional changes in  $\text{Cu}_2\text{ZnSnS}_4$  films and solar cells. *Solar Energy Materials and Solar Cells* **2012**, 98, (0), 110-117.
62. Niki, S.; Fons, P. J.; Yamada, A.; Lacroix, Y.; Shibata, H.; Oyanagi, H.; Nishitani, M.; Negami, T.; Wada, T., Effects of the surface  $\text{Cu}_2\text{Se}$  phase on the growth and properties of  $\text{CuInSe}_2$  films. *Applied Physics Letters* **1999**, 74, (11), 1630-1632.
63. Bar, M.; Schubert, B. A.; Marsen, B.; Krause, S.; Pookpanratana, S.; Unold, T.; Weinhardt, L.; Heske, C.; Schock, H. W., Impact of KCN etching on the chemical and electronic surface structure of  $\text{Cu}_2\text{ZnSnS}_4$  thin-film solar cell absorbers. *Applied Physics Letters* **2011**, 99, (15), 152111-3.
64. Fairbrother, A.; Garcia-Hemme, E.; Izquierdo-Roca, V.; Fontane, X.; Pulgarin-Agudelo, F. A.; Vigil-Galan, O.; Perez-Rodriguez, A.; Saucedo, E., Development of a selective chemical etch To improve the conversion efficiency of Zn-rich  $\text{Cu}_2\text{ZnSnS}_4$  solar cells. *Journal of the American Chemical Society* **2012**, 134, (19), 8018-8021.
65. Bag, S.; Gunawan, O.; Gokmen, T.; Zhu, Y.; Todorov, T. K.; Mitzi, D. B., Low band gap liquid-processed CZTSe solar cell with 10.1% efficiency. *Energy & Environmental Science* **5**, (5), 7060-7065.
66. Saha, S. K.; Guchhait, A.; Pal, A. J.,  $\text{Cu}_2\text{ZnSnS}_4$  (CZTS) nanoparticle based nontoxic and earth-abundant hybrid pn-junction solar cells. *Physical Chemistry Chemical Physics* **2012**, 14, (22), 8090-8096.
67. Xin, X.; He, M.; Han, W.; Jung, J.; Lin, Z., Low-cost copper zinc tin sulfide counter electrodes for high-efficiency dye-sensitized solar cells. *Angewandte Chemie International Edition* **2011**, 50, (49), 11739-11742.



# Chapter 3: Controlled Synthesis and Characterizations of $\text{Cu}_2\text{ZnSnS}_4$ Nanoparticles

## 3.1 Introduction

Nanoparticles have been intensively studied ever since its discovery due to the potential applications in electrical, optical and biomedical fields.<sup>1, 2</sup> Owing to the quantum confinement effect, both optical and electrical properties of materials, such as Au and CdSe, at nanometer size range can vary with respect to the sizes.<sup>3</sup> For instance, the absorption edge of CdSe nanocrystals blue shifts as the size increases from 17Å to 150Å, showing a decrease in the energy band gap.<sup>4</sup> Hence, to be able to control the size of the nanoparticles is of significant importance.

Nanoparticles can be used as the building blocks for micro-size grains and thin films, and thermal treatments are usually employed to enhance the crystal growth.<sup>5</sup> This idea was successfully demonstrated in photovoltaics devices by Gur et al.<sup>6</sup> In their work, CdSe and CdTe nanocrystals were prepared in solution separately, and then spin-coated to form CdSe donor layer and CdTe acceptor layer. The as-fabricated solar cell showed an encouraging efficiency of 2.9%. Guo et al. made use of the idea in the preparation of  $\text{Cu}_2\text{ZnSnS}_4$  (CZTS) based TFSCs.<sup>7</sup> A dispersion of pre-synthesized CZTS was used as the ink and sprayed onto substrate to form nanoparticles film. The CZTS film was then annealed in Se vapor and the device achieved a very promising efficiency of 7.2%.

The possibility of using CZTS nanocrystals dispersion as ink for the preparation of CZTS thin film has sparked a great deal of research efforts on CZTS nanoparticles. The

synthesis of CZTS nanoparticles was first reported using hot injection method.<sup>8-10</sup> This method features a rapid injection of sulfur precursor into Cu-, Zn-, Sn-precursor at elevated temperatures. Solvothermal synthesis route were also reported with different variation in solvents and surfactants.<sup>11-13</sup> More recently, Wang et al. adopted a more environmentally friendly route and synthesized CZTS nanostructures using a hydrothermal method.<sup>14</sup>

Among the synthesis methods discussed so far, the hot injection method offers good size, shape and compositional control. It allows the nucleation and growth steps of nanoparticles to be separated and thus offers narrower size distribution. Moreover, through ligand optimization, the size as well as the shape of the nanocrystals could be controlled.<sup>15</sup> This method has been widely used in the synthesis of semiconductor nanocrystals including CdSe, PbS, Sb<sub>2</sub>S<sub>3</sub>, Cu<sub>2</sub>InSe<sub>2</sub> and CZTS<sup>4, 10, 16-18</sup> In the case of CZTS, near mono-disperse nanoparticles with size ranging from 10 nm to 50 nm could be obtained.<sup>8, 9</sup> The composition of nanoparticles could also be adjusted by modifying relative amount of Cu-, Zn-, Sn- and S- precursors.<sup>7</sup>

Despite the above progress on the synthesis of CZTS nanoparticles, several issues remain to be solved. First of all, the growth mechanism including the nucleation and growth processes is still not clearly understood. In addition, the size and shape control of CZTS nanocrystals remain to be quite challenging. The knowledge of the growth mechanism and the size-, shape-control of CZTS nanocrystals would be very beneficial for their application in solar cells or other potential applications. In this chapter, CZTS nanoparticles are prepared using the hot injection method. The metal precursors used are

generally Cu-, Zn-, Sn-chlorides/acetates/acetylacetonates. Prior to the reaction to form CZTS, coordinating complex of Cu, Zn and Sn are first formed and then heated to the reaction temperature before sulfur precursor was injected. Kesterite-type CZTS nanoparticles are synthesized and studied in this chapter. We will investigate in-depth the synthesis of CZTS nanoparticles using hot injection method. The growth mechanism for CZTS nanoparticles is also proposed. The size and shape of CZTS nanoparticles will be controlled through the optimizations of solvent and ligands.

### 3.2 Experimental Procedures

#### *Chemicals*

Copper (II) acetate ( $\text{Cu}(\text{OAc})_2$ , Aldrich, 98%), zinc chloride anhydrous ( $\text{ZnCl}_2$ , Sigma-Aldrich, 99.99%), tin (IV) chloride pentahydrate ( $\text{SnCl}_4 \cdot 5\text{H}_2\text{O}$ , Sigma-Aldrich, 98%), elemental sulfur (S, Aldrich), oleylamine (OLA, Aldrich, 70%), toluene (Aik Moh Paints & Chemicals), methanol (Aik Moh Paints & Chemicals, 95%), ethanol (Aik Moh Paints & Chemicals, 95%) and Milli-Q water (Millipore, 18.5  $\text{M}\Omega\text{cm}$  at 25 °C) were purchased and used as received.

#### *Experiment*

The CZTS nanoparticles were prepared using hot injection method. The experimental setup is shown in Figure 3.1. In a typical synthesis, 0.5 mmol  $\text{Cu}(\text{OAc})_2$ , 0.25 mmol  $\text{ZnCl}_2$ , 0.25 mmol  $\text{SnCl}_4 \cdot 5\text{H}_2\text{O}$  and 5 ml OLA were mixed into a three neck flask. The mixture was then gradually heated up under vacuum condition to remove moisture and oxygen. At around 100 °C, the reaction setup was purged with  $\text{N}_2$  gas. After that, the reaction mixture was heated to 150 °C and incubated at this temperature for 30 min.

During the incubation at 150 °C, the solution color turned from dark blue to yellow, indicating the formation of the Cu-, Zn-, and Sn-OLA complex. And the Cu-, Zn- and Sn-OLA complex will be denoted as the metal precursor. After that, the mixture was rapidly heated to the reaction temperature, where sulfur precursor which contains 1 mmol S dissolved in 1 ml OLA was rapidly injected. The solution mixture was maintained at the reaction temperature for 1 hour. After that, the reaction system was cooled down in air to room temperature. The as-prepared CZTS nanoparticles were washed four times using toluene and ethanol. The nanocrystals dispersion can then be used for CZTS thin film deposition.

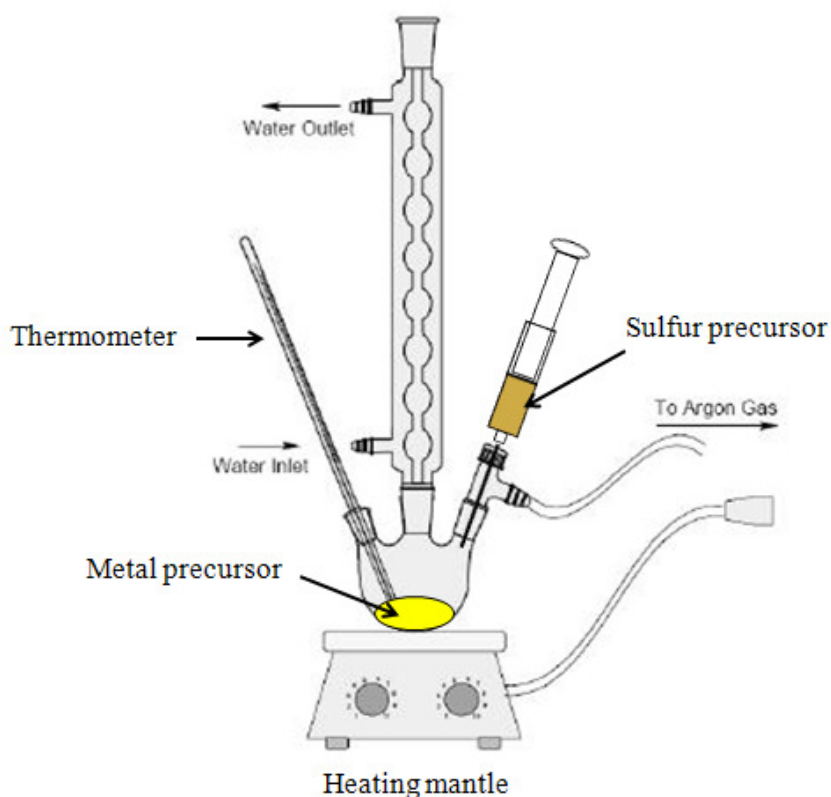


**Figure 3.1:** A brief illustration of experimental setup for the synthesis of CZTS nanocrystals using hot injection method. The metal precursor contains Cu-, Zn- and Sn-OLA complex.

### *Characterizations*

The Grazing Incidence X-ray diffraction (GIXRD) patterns were collected using Bruker D8 Advance equipped with Cu K $\alpha$  radiation ( $\lambda = 1.54 \text{ \AA}$ ). The diffraction was taken at a fixed incident angle of  $1^\circ$ , and collected from  $20^\circ$  to  $80^\circ$  in steps of  $0.05^\circ$ . Rietveld refinement was performed using TOPAS V3 software with fundamental parameter peak profile for CZTS sample. A five-coefficient Chebychev polynomial and  $1/x$  background, a zero error, scale factor, lattice parameters and crystal size were successively refined. SEM images were captured on a JEOL JSM 7600F FESEM at an accelerating voltage of 5 kV. The FESEM is equipped with an Oxford X-MAX energy dispersive X-ray spectroscopy (EDS) detector, which was used to estimate the atomic ratio of CZTS thin film. The EDS data were acquired at accelerating voltage of 20 kV. The film was deposited on Si substrate to reduce the sample charging during imaging and EDX measurement. The TEM analysis was performed using JEOL JSM – 2100F equipped with EDAX EDS detector. The voltage used for imaging and elemental mapping was 200 kV. The UV-Vis-NIR absorption measurements were performed using a Shimadzu UV-Vis-NIR PerkinElmerLambda 900 spectrophotometer.

### **3.3 Results and Discussion**

In order to achieve good control over the synthesis of CZTS nanoparticles, it is important to understand the effects of several critical factors in synthesis of these nanoparticles. These factors include reaction temperature, reaction time, solvents and surfactants. The reaction temperature may affect the phase formation of CZTS and with this knowledge we will be able to figure out an optimum reaction temperature for pure CZTS. The time-

dependent studies can help us to gain an in-depth understanding of the nucleation and growth processes. In addition, the formation mechanism of CZTS nanocrystals is proposed. Lastly, through the solvent-ligand optimization, it is possible to control the size and shape of CZTS nanoparticles.

### 3.3.1 Effect of reaction temperature

The reaction temperature strongly influences the reaction kinetics of the synthesis process.<sup>19, 20</sup> In this section, the reaction temperatures from 180 to 260 °C were investigated. The reaction time was fixed at 1 hour for all temperatures. Figure 3.2 presents the XRD patterns of samples synthesized at 180, 200, 220, 240 and 260 °C. All the XRD patterns exhibit 2 $\theta$  peaks at 28.5°, 33°, 47.3°, 56.2°, 69.3° and 76.5°. The above six diffraction peaks match well with the CZTS kesterite database (JCPDS no. 26-0575), indicating the formation of CZTS kesterite at all five reaction temperatures. It is also noticed that for samples prepared at 180 °C, a strong diffraction peak around 46.4° together with minority peaks at 49.4° and 54.8° were also detected. These three peaks can be assigned to Cu<sub>9</sub>S<sub>5</sub> (JCPDS no. 47-1748). The observation of Cu<sub>2-x</sub>S phases at reaction temperature below 180 °C in the synthesis of CZTS agrees well with the other reports on secondary phases obtained in non-injection synthesis.<sup>19</sup> Although the XRD patterns of the samples (except those samples prepared at 180 °C which contains Cu<sub>9</sub>S<sub>5</sub>) matched well with CZTS kesterite database, it is difficult to confirm the formation of CZTS kesterite based on the XRD data. The reason is that CZTS kesterite shares very similar crystallographic structures and thus the XRD patterns with a few binary and ternary impurity phases including Cu<sub>2</sub>S (JCPDS no. 4-15-2234), ZnS (JCPDS no. 5-0566) and

$\text{Cu}_2\text{SnS}_3$  (CTS) (JCPDS no. 1-089-4714). Hence, besides XRD, a more differentiating study of the nanoparticles synthesized is required to exclude the existence of the above binary and ternary phases.

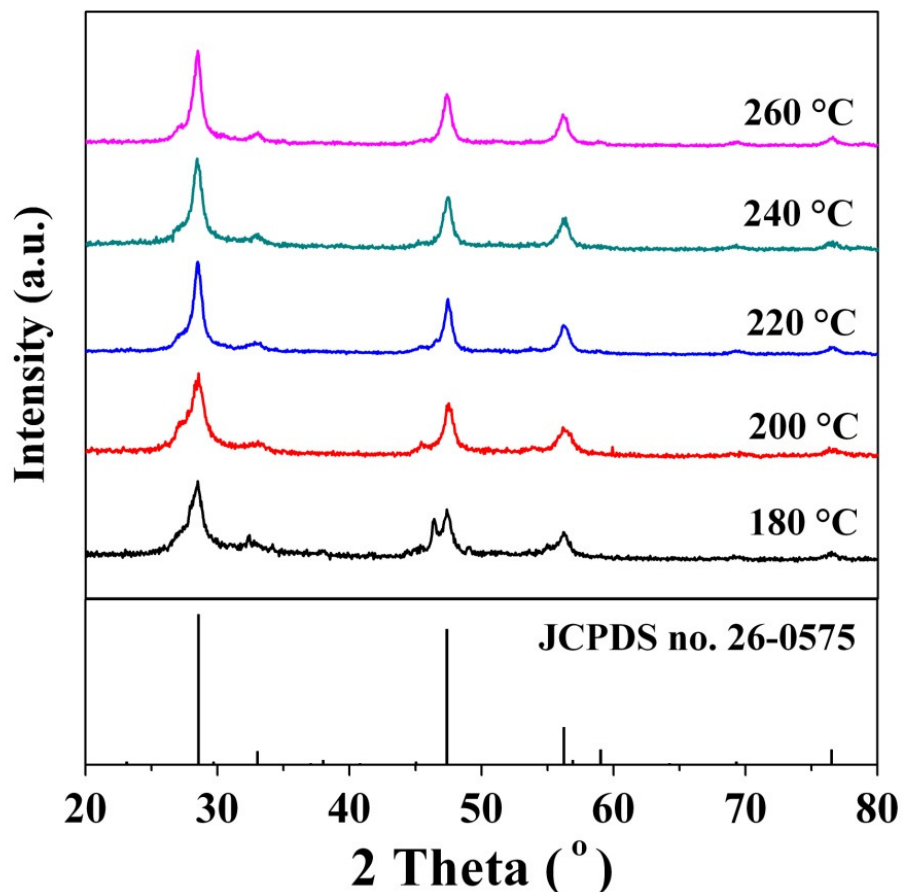


**Figure 3.2.** The XRD diffraction patterns of samples prepared at different reaction temperatures of 180, 200, 220, 240 and 260 °C. The standard diffraction peaks for kesterite CZTS (JCPDS no. 26-0575) is provided.

Raman spectroscopy is useful in detecting the vibrational, rotational, as well as other low-frequency modes in materials. The Raman shifts for CZTS ( $288\text{ cm}^{-1}$ ,  $338\text{ cm}^{-1}$ ,  $368\text{ cm}^{-1}$ ) and  $\text{Cu}_{2-x}\text{S}$  ( $264\text{ cm}^{-1}$  and  $475\text{ cm}^{-1}$ ), ZnS ( $278\text{ cm}^{-1}$  and  $351\text{ cm}^{-1}$ ), orthorhombic CTS ( $318\text{ cm}^{-1}$ ) as well as tetragonal CTS ( $298\text{ cm}^{-1}$  and  $356\text{ cm}^{-1}$ ) are distinct, and thus

Raman spectroscopy are usually used to differentiate these compounds or identify impurity phases.<sup>21-25</sup> Figure 3.2 presents the Raman analysis for CZTS samples synthesized at the five different temperatures. As shown in Figure 3.3, the Raman shifts exhibit a major peak at  $338\text{ cm}^{-1}$  for all temperatures, which corresponds to the Raman A mode of CZTS.<sup>26</sup> Besides, two weak shoulder peaks at  $288$  and  $368\text{ cm}^{-1}$  could also be noticed. In some cases, these shoulder peaks are not quite distinct due to the following two reasons: (i) the influence of surfactants and (ii) the broadening of  $338\text{ cm}^{-1}$  peak at nanometer size. The Raman peaks of  $288$ ,  $338$  and  $368\text{ cm}^{-1}$  matched well with CZTS, indicating the formation of CZTS phase. As for samples synthesized at  $180\text{ }^{\circ}\text{C}$ , two additional peaks at  $264\text{ cm}^{-1}$  and  $318\text{ cm}^{-1}$  could also be noticed. The peak at  $264\text{ cm}^{-1}$  originates from the  $\text{Cu}_{2-x}\text{S}$  impurity phase, which is in good agreement with the observation of  $\text{Cu}_9\text{S}_5$  from the XRD studies. The peak at  $318\text{ cm}^{-1}$  could be attributed to orthorhombic CTS. The Raman data suggests that the binary  $\text{Cu}_{2-x}\text{S}$ , ternary CTS and quaternary CZTS co-exist in the samples synthesized at  $180\text{ }^{\circ}\text{C}$ . Similarly, the sample prepared at  $200\text{ }^{\circ}\text{C}$  was found to contain a mixture of CZTS and CTS. For samples synthesized at  $220$ ,  $240$  and  $260\text{ }^{\circ}\text{C}$ , no other peaks could be observed except peaks related to CZTS ( $288$ ,  $338$  and  $368\text{ cm}^{-1}$ ), which indicates pure CZTS phase were obtained. The absence of the binary and ternary phases at these temperatures suggests quaternary CZTS phase are favored at high temperature. It is also noticed that the peak at  $338\text{ cm}^{-1}$  becomes broader with the increase in temperature from  $220\text{ }^{\circ}\text{C}$  to  $260\text{ }^{\circ}\text{C}$ , which could be attributed to the decrease in nanoparticles size with the increasing reaction temperature. The increase in reaction temperature greatly decreases the stability of precursors and increases the energy for reaction thus resulting in fast nucleation and



growth of nanocrystals.<sup>27</sup> This will lead to more nuclei at high reaction temperature and thus a decrease the average size of nanoparticles.

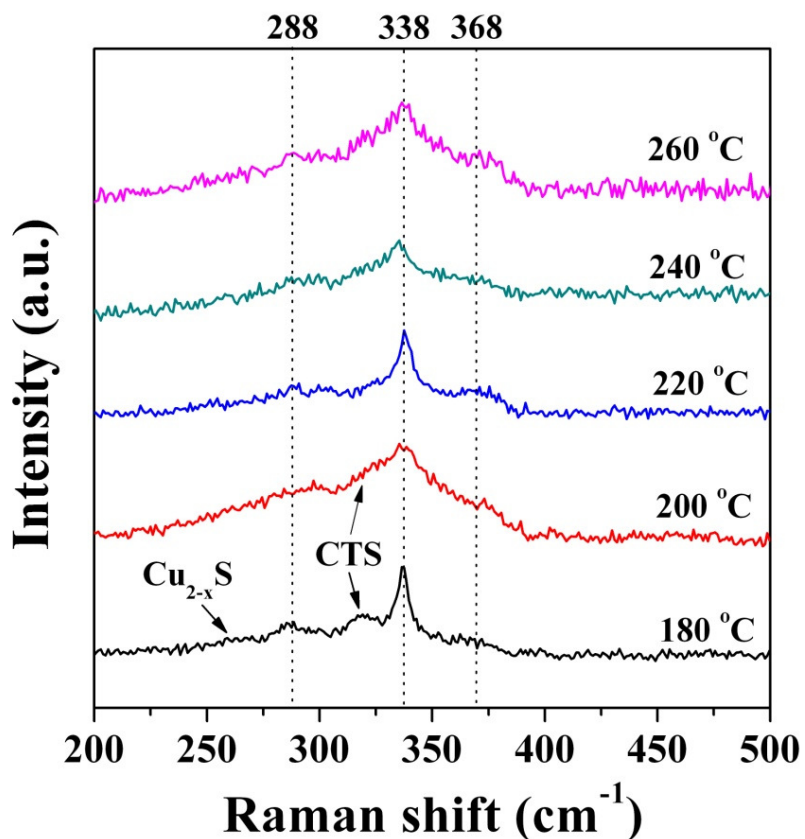


**Figure 3.3.** The Raman analysis of samples prepared at different reaction temperatures of 180, 200, 220, 240 and 260 °C. The peak positions of 288, 338 and 368 cm<sup>-1</sup> are labeled with vertical dotted lines.

Based on the results from temperature studies, pure kesterite CZTS nanoparticles were definitely formed at 240 °C. The nanoparticles prepared at 240 °C were further investigated using XRD, EDX, TEM and UV-vis-NIR spectroscopy. Figure 3.4 displays the rietveld refinement XRD data obtained from samples prepared at 240 °C. A long 2 $\theta$  range of XRD scan from 10° to 120° was used. The peaks at 18.2°, 28.5°, 33.0°, 38.0°, 45.0°, 47.4°, 56.3°, 59.0°, 69.3°, 76.5°, 88.2°, 95.2°, 107.0° and 114.4° could be observed

from the XRD measurements. All these peaks match well with the simulated CZTS XRD pattern, with the observed peaks corresponding to (101), (112), (200), (211), (105), (220), (312/303), (224), (008), (332), (228), (512), (440) and (532) planes respectively. The results from rietveld refinement indicate pure CZTS kesterite was synthesized.

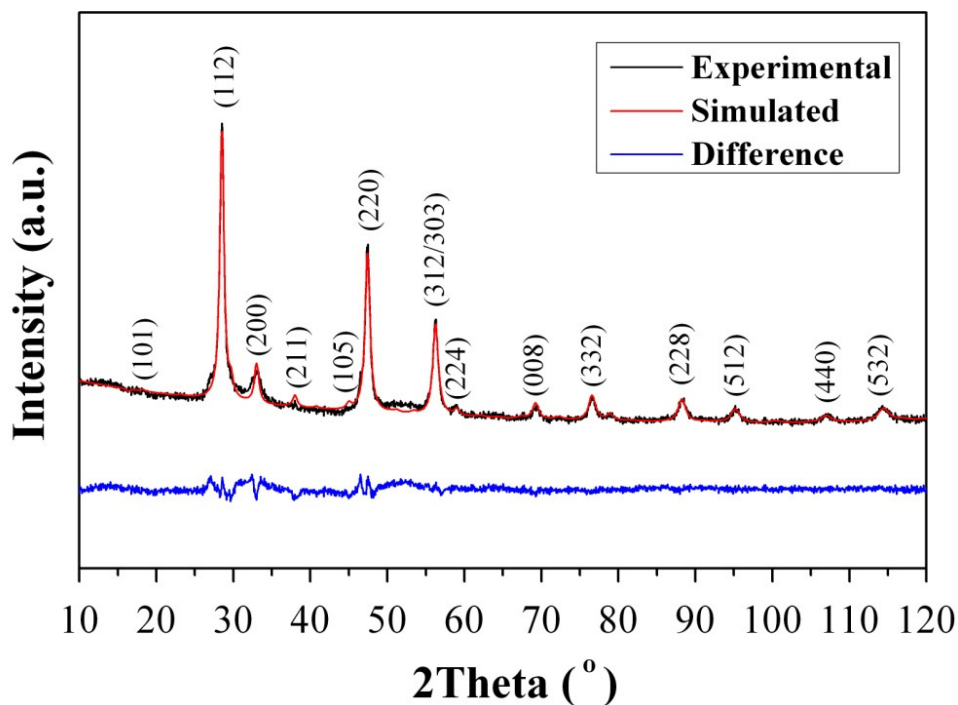


**Figure 3.4.** The rietveld refinement XRD data obtained from samples prepared at 240 °C. A five-coefficient Chebychev polynomial and 1/x background, a zero error, scale factor, lattice parameters, crystal size and preferred orientation were successively refined.

The average composition of CZTS nanoparticles was determined by Energy Dispersive X-ray Spectroscopy (EDS) installed in a FESEM (JEOL 7600F). The samples were prepared by drop-casting CZTS nanoparticles dispersion in toluene onto a sodium lime glass substrate. The percentages of S, Cu, Zn and Sn for five different spots were measured. And then the average percentages of all four elements were determined. The ratio for each element was calculated by dividing each percentage with 12.5%

respectively. In the stoichiometric CZTS, the Cu, Zn, Sn and S ratio is 2: 1: 1: 4, and therefore  $100\%/(2+1+1+4) = 12.5\%$  is used. The average ratio of Cu, Zn, Sn and S was determined to be 1.96: 0.80: 1.05: 4.19 and thus the chemical formula could be written as  $\text{Cu}_{1.96}\text{Zn}_{0.80}\text{Sn}_{1.05}\text{S}_{4.19}$ . The details of EDX results could be found in Appendix A. It could also be noticed that the composition of as-synthesized CZTS nanoparticles is slightly Zn-poor. The reason is due to the relatively low reactivity of Zn precursor compared with other precursors.<sup>28</sup> The Zn-poor issue could be solved by using a more reactive Zn-precursor, for example,  $\text{ZnI}_2$ .

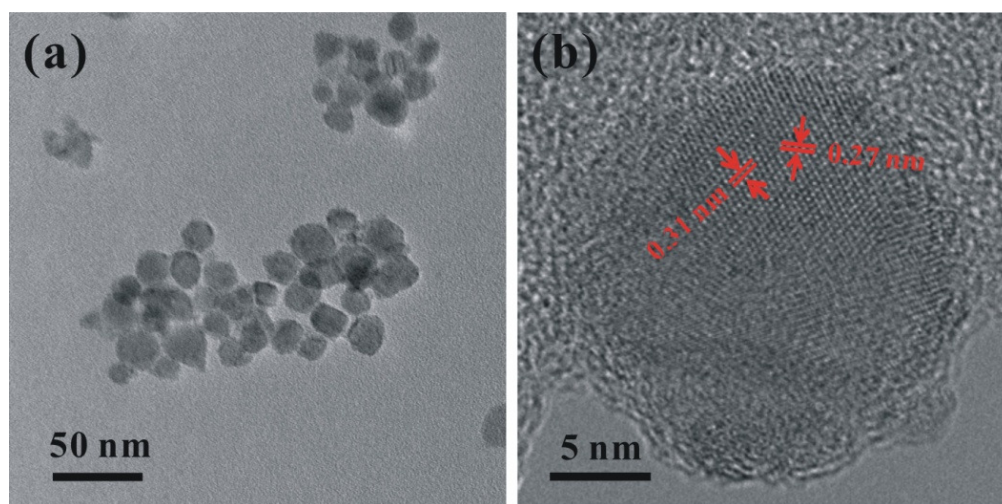


**Figure 3.5.** (a) TEM and (b) HRTEM images of as-synthesized CZTS. The TEM sample was prepared by dropping casting CZTS nanoparticles suspension onto a Ni-grid.

Figure 3.5 shows transmission electron microscopy (TEM) images of the as-synthesized CZTS nanoparticles. As shown in Figure 3.5a, CZTS nanoparticles have near spherical shape and the average size of the nanoparticles is estimated to be around  $19.8 \pm 3.9$  nm. The HRTEM image is displayed in Figure 3.5b and the lattice spacings of 0.31 nm and 0.27 nm were measured, which corresponds to (112) and (020) planes respectively. In

order to determine the distribution of Cu, Zn, Sn and S in CZTS nanoparticles, the scanning transmission electron microscopy – energy dispersive X-ray spectroscopy (STEM-EDS) elemental mapping was performed as shown in Figure 3.6. It could be noticed that all the elements (Cu, Zn, Sn and S) were distributed uniformly within the inspected CZTS nanoparticles, which serves as another evidence for the formation of pure CZTS.

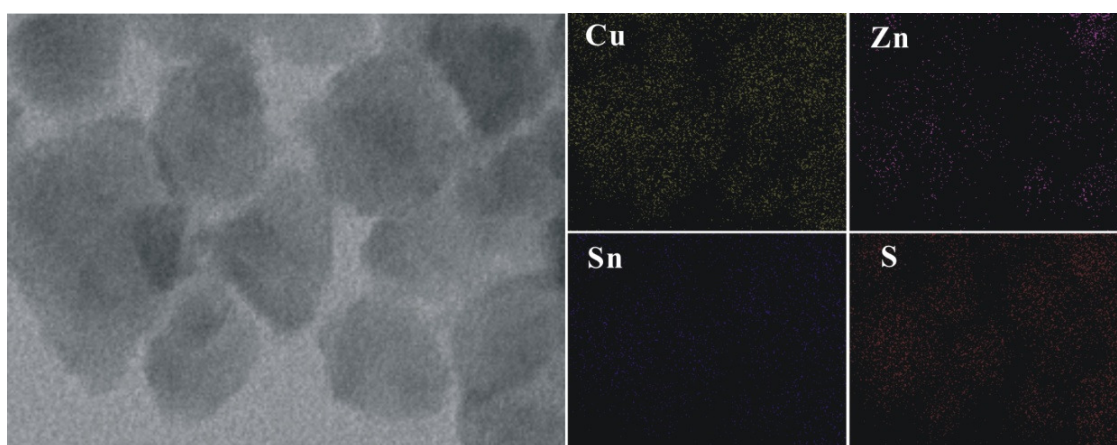


**Figure 3.6.** STEM-EDS elemental mapping of as-synthesized CZTS nanocrystals. The distributions of Cu, Zn, Sn and S were presented.

Figure 3.7 shows the UV-vis-NIR absorption spectrum (1200 nm to 400 nm) of the nanoparticles synthesized at 240 °C. The onset of absorption is found to be about 800 nm. The inset of Figure 3.7 shows the of  $(\alpha h\nu)^2$  vs.  $h\nu$  plot, from which the band gap can be calculated using the intercepts on the  $h\nu$  axis by elongating the linear region of the curve. In this case, the band gap of CZTS nanoparticles was determined to be 1.55 eV, which matched well with the band gap for near stoichiometric composition published previously.

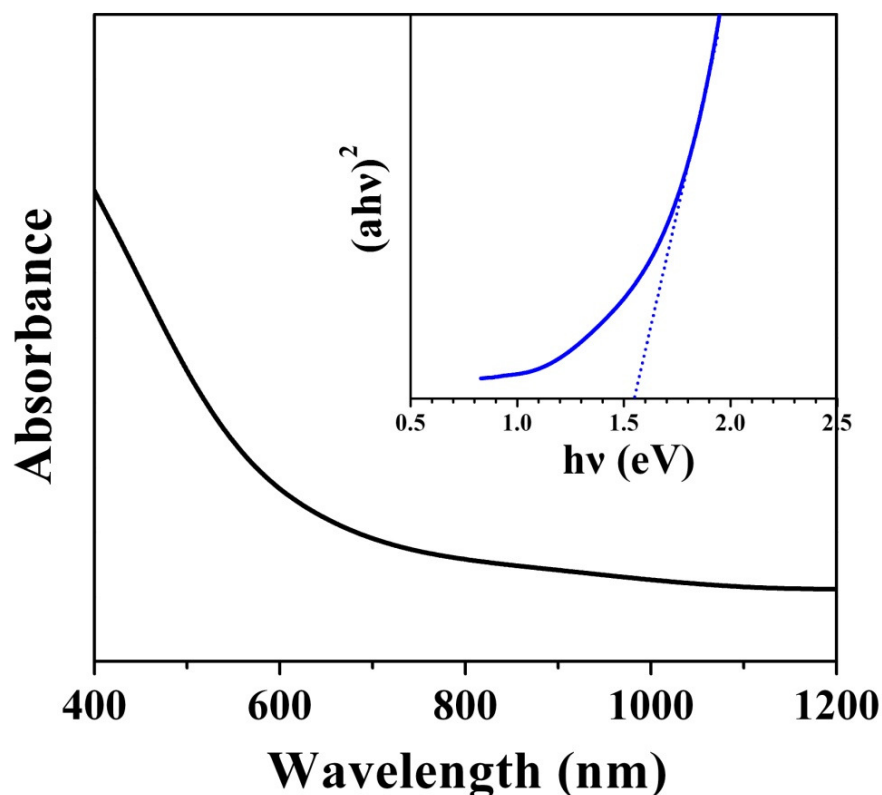
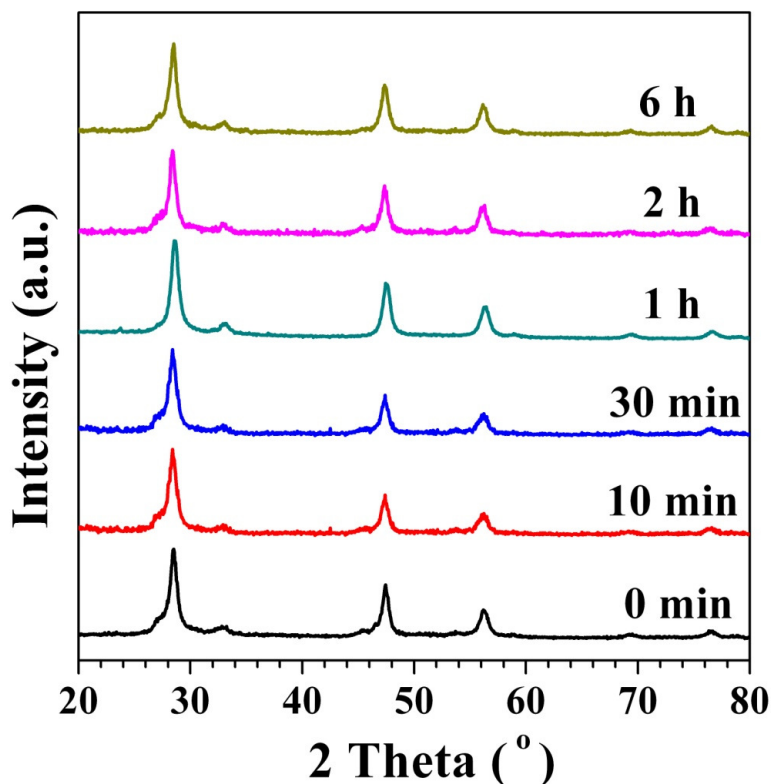


**Figure 3.7:** UV-vis absorption spectrum of as synthesized CZTS nanocrystals. Inset shows the  $h\nu$  vs.  $(\alpha h\nu)^2$  and the band gap is calculated to be 1.55 eV.

### 3.3.2 Effects of reaction time – A study on the growth mechanism

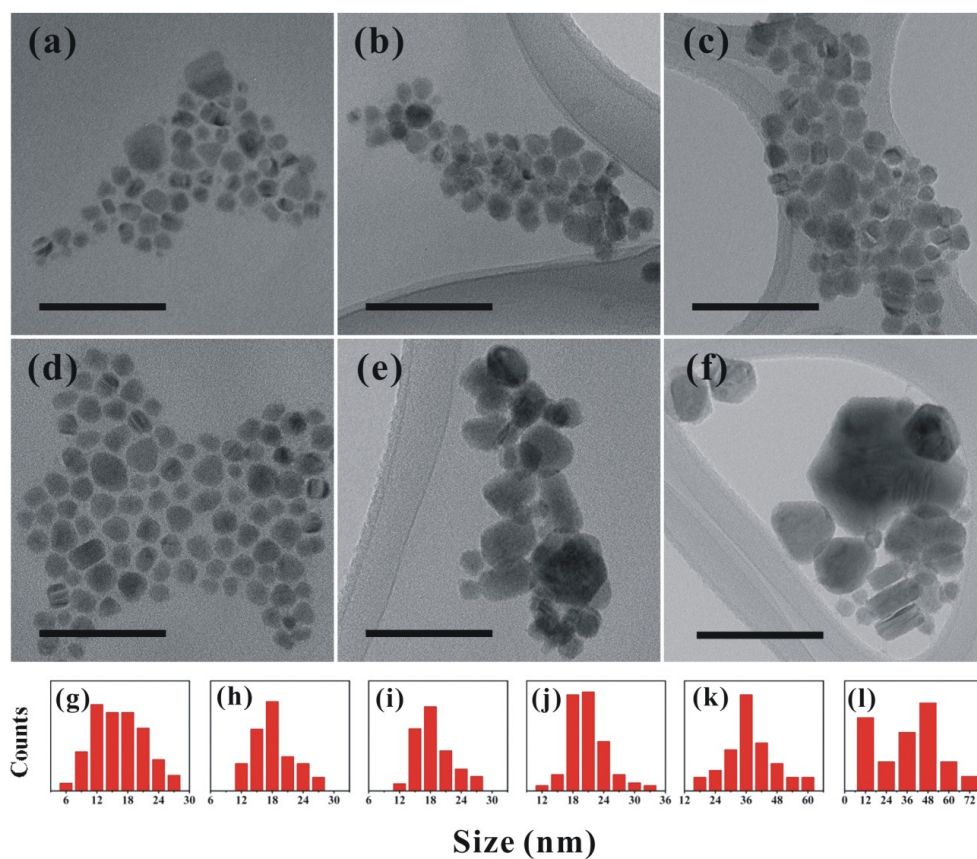
The effects of reaction time were investigated to understand the nucleation and growth process during the synthesis. This will allow better control of the size and stoichiometry development during the synthesis. The reaction temperature was fixed at 240 °C. During the reaction, aliquots of 1 ml were extracted immediately after injection (0 min) and at different time intervals thereafter (10 min, 30 min, 1 hour, 2 hour and 6 hour). Each aliquot was subsequently quenched to room temperature and the products are studied using XRD and TEM.

Figure 3.8 shows the XRD patterns of CZTS extracted at the different time intervals. It could be noticed that the six CZTS nanoparticles samples synthesized at different reaction time exhibit almost identical XRD patterns. The three major peaks at  $28.5^\circ$ ,  $47.6^\circ$  and  $56.3^\circ$  are the characteristic peaks for kesterite CZTS and are observed at all different reaction times. These findings indicate that well crystalline kesterite CZTS nanoparticles formed very soon after injection of sulfur precursor and the kesterite CZTS phase was maintained throughout the investigated time interval. It is also worth to note that no intermediate products or impurity phases can be detected throughout the duration investigated.



**Figure 3.8:** The XRD patterns of CZTS nanoparticles synthesized at different reaction time of 0 min, 10 min, 30 min, 1 h, 2 h and 6 h.





**Figure 3.9.** The TEM images of CZTS nanoparticles synthesized at 240 °C with different reaction time of (a) 0 min, (b) 10 min, (c) 30 min, (d) 1 h, (e) 2 h, and (f) 6 h. The scale bar stands for 100 nm for all. (g-l) presents the size distribution for (a-f) sequentially.

**Table 3.2** The average size and standard derivation of CZTS nanoparticles with respect to reaction time

size	0 min	10 min	30 min	1 hour	2 hour	6 hour
<b>Ave. size (nm)</b>	15.6	17.5	18.0	19.8	31.4	44.3
<b>Std. Dev. (nm)</b>	5.0	4.2	3.7	3.9	9.4	22.3

Figure 3.9 shows the TEM images of CZTS nanoparticles collected at different stages during the reaction and also their respective size distributions. As shown in Figure 3.9a (0

min), nanoparticles were formed immediately after injection of sulfur precursor, indicating a fast reaction rate. The size of the nanoparticles is between a few nanometers to a few tens of nanometers. And the shapes of the nanoparticles are generally irregular with near spherical, triangular, elongated shapes. The average size of the pictured nanoparticles (Table 3.2) was determined to be  $15.6 \pm 5.0$  nm. As the reaction time increases to 10 min (Figure 3.9b), the ratio of small particles ( $< 10$  nm) decreased, implying the crystal growth of small particles. The average crystal size increased to  $17.5 \pm 4.2$  nm. In addition, the shapes of nanoparticles became more spherical. At reaction time of 30 min (Figure 3.9c), the nanoparticles continue to grow and the average crystal size increased to  $18.0 \pm 3.7$  nm and the size distribution became narrower. The shapes of nanoparticles became near spherical and were more uniform than 0 and 10 min. At 1 h (Figure 3.9d), the nanoparticles continued to grow to 19.8 nm, however the size distribution became slightly poorer. The near spherical shape of the nanoparticles maintained. After 2 h (Figure 3.9e), the average crystal size increases significantly to 31.4 nm. In addition, the size distribution became much poorer with some particles larger than 50 nm while some are smaller than 10 nm. At 6 h (Figure 3.9f), the average size of nanoparticles continue to grow to 44.3 nm, while the size distribution become even poorer than 2 h. The results of time dependent studies are in good agreements with earlier work.<sup>9</sup>

From 30 min onwards, the nanoparticles growth follows a similar process to that of Ostwald ripening, for which the large particles grow at the expense of the dissolution of smaller particles. In a classic Ostwald ripening model, the average radius ( $R$ ) is proportional to time in the power of  $1/3$  ( $t^{1/3}$ ). Figure 3.10 presents average size vs.  $t^{1/3}$



plot. It is found that the average sizes of nanoparticles are linearly dependent on  $t^{1/3}$  from 30 min onward. These results show that the nanoparticles growth followed an Ostwald ripening process. It happens when the concentration of precursors drop to a critical level that further growth of nanoparticles requires the dissolution of small particles to provide additional precursors. Due to the Ostwald ripening, the size distribution becomes poorer with the increase of reaction time.

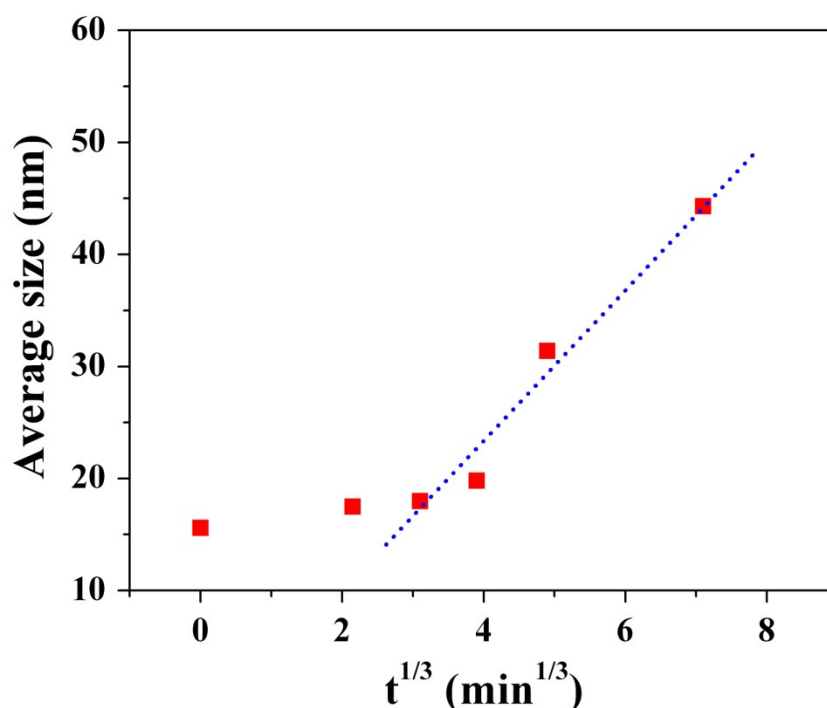


**Figure 3.10.** The average size of nanoparticles vs.  $t^{1/3}$  plot where  $t$  is the reaction time. The near linear relationship is observed from 30 min onward.

The growth mechanism of CZTS nanoparticles can be proposed based on results from time-dependent studies. Before the injection of S precursor, the metal precursor form stable yellowish Cu-, Zn-, Sn- OLA complexes at elevated temperature.<sup>9</sup> In the earlier reports, it was found that the sulfur precursor form alkylammonium polysulfides at room

temperature.<sup>31, 32</sup> Upon injection of cold sulfur precursor into hot metal precursor, the temperature of sulfur precursor is suddenly raised to above 200 °C and H<sub>2</sub>S is produced.<sup>33</sup> In the reaction mixture, the S, Cu, Zn and Sn species suddenly reach supersaturation stage, and therefore precipitate out as CZTS nanoparticles. The Cu, Zn and Sn form similar bonding with OLA with comparable high reaction rates at the reaction temperature of 240 °C. That is why pure kesterite CZTS is formed with no noticeable binary or ternary impurity phases. The formation of nanoparticles usually consists of nucleation stage and growth stage.<sup>27</sup> In the case of CZTS nanoparticles, the nucleation occurs so fast that we were not able to capture the nucleation stage. As discussed in previous paragraph, well crystalline CZTS nanoparticles with average size of 15.6 nm formed immediately after injection. The size of nanoparticles increases as reaction time increasing from 0 min to 6 h.

It is noticed that the size distribution first become narrower from 0 min to 30 min, and then become wider from 30 min to 6 h. This observation is understandable. From 0 min to 30 min, the nanoparticles grow with the consumption of precursors in solution. The small particles have high surface energy and thus are preferred to grow. At around 30 min, the precursor concentration is reduced to a critical level, where the precipitation and dissolution of CZTS nanoparticles are in equilibrium. Further growth of CZTS nanoparticles requires the dissolution of some nanoparticles, similar to the phenomenon of Ostwald ripening. Small particles are less stable and therefore dissolve and re-precipitate onto large particles. The average size of nanoparticles increases at the expense of size distribution.

### 3.3.3 Effect of solvent and ligand

It is well known that the solvent and surfactant have great influences over the final size and shape of the nanoparticles.<sup>34, 35</sup> In the above synthesis, OLA serves both as solvent and surfactant. It is therefore difficult to distinguish the relative amount of solvent as well as surfactant. As a result, the size and shape control becomes challenging. One way to overcome this issue is to separate the function of the solvent and ligand by using two chemicals instead of only OLA. And one chemical will behave solely as solvent and another chemical as the ligand.

Panthani et al. reported the synthesis of CuInS<sub>2</sub> (CIS) nanoparticles with dichlorobenzene (DCB) as solvent and OLA as ligand.<sup>5</sup> In our modified synthesis, 1,2-dichlorobenzene (DCB) was introduced as the new solvent and OLA was used as the ligand. Copper acetylacetonate, zinc acetylacetonate, tin bis(acetylacetonate) dichloride and elemental sulfur were used as the precursors. All above precursors could dissolve very well in DCB. Thus, unlike the typical synthesis where OLA serves as both solvent and ligand, the functions of solvent and ligand are separated in the modified synthesis. The similar experimental procedures were used in the modified synthesis. 10 ml of DCB were used in the synthesis and the amount from OLA varied from 0 ml, 1 ml and 2ml. The reaction was kept at 180 °C for 1 hour. The reaction temperature of 180 °C rather than higher temperature was used is because the boiling point of DCB is around 180 °C.

Figure 3.11a presents the XRD pattern of as-synthesized CZTS nanoparticles with 1 ml OLA. The XRD pattern matched well with CZTS database (JCPDS no. 26-0575). The peaks at 2 Theta angle of 28.5°, 33.0°, 47.3°, 56.2°, 59.0°, 69.3° and 76.5° correspond to

(112), (200), (220), (312/303), (224), (008) and (332) planes respectively. The Raman peaks at 288, 338 and 368  $\text{cm}^{-1}$  (Figure 3.11b) provides additional evidence for the formation of CZTS phase. It is worth highlighting that in the system where OLA serves as both solvent and ligand, in addition to CZTS,  $\text{Cu}_{2-x}\text{S}$  and CTS impurity phases were also formed. On the other hand, in the system with DCB solvent and OLA ligand, pure CZTS phase was produced. One possible reason could be due to  $\text{sp}^2$  orbital associated with DCB, which changes the reaction kinetics compared with that of OLA solvent-ligand system. In OLA solvent, the Cu- and Sn- species have relative high reaction rate compared to others, therefore Cu-, Sn- rich phases were formed. While in DCB solvent, the Cu-, Zn- and Sn- species have comparable reaction rate, leading to formation of quaternary CZTS phases.

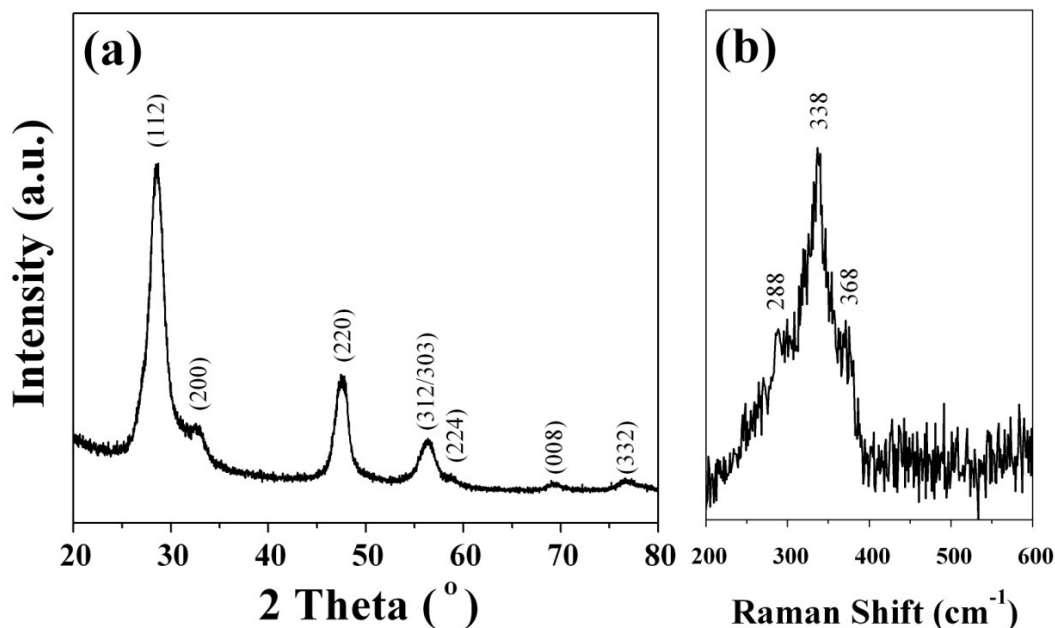


**Figure 3.11.** (a) The XRD pattern and (b) the Raman analysis of CZTS nanoparticles synthesized with DCB solvent and 1 ml OLA as surfactant.

When the function of solvent and ligand is separated, it is possible to investigate how the amount of ligands can control morphological development. Hence the effect of the amount of OLA on the size and shape of CZTS nanoparticles were also investigated. Figure 3.11 shows the CZTS nanoparticles synthesized with 0 ml, 0.5 ml, 1 ml and 2 ml OLA respectively. As shown in Figure 3.12a, the CZTS form sub-micrometer size cluster without OLA. The nanoparticles are inherently instable due to the high ratio of surface atoms. Therefore, they tend to aggregate into large clusters without the passivation of surface atoms either by surfactants or electrical charge. In Figure 3.12b, highly mono-disperse nanocrystals were obtained with the addition of 0.5 ml OLA surfactant. The nanoparticles show an average size of 6.2 nm and exhibit a near-spherical shape. As the amount of surfactants increases to 1 ml (Figure 3.12c), the nanoparticles show faceted edge and the average size increased to about 9.3 nm. With further increase in the amount of surfactants to 2 ml (Figure 3.12d), the nanoplates were produced. The majority low contrast nanoparticles show the lying nanoplates while the occasional high contrast site picturing the standing nanoplates. These nanoplates have an average thickness of 3.7 nm and an average length of 12.6 nm. Figure 3.12 e and f display the high resolution TEM images of CZTS nanoparticles synthesized with 1 ml and 2 ml of OLA respectively. In both images, the lattice spacings of 0.31 nm and 0.27 nm are measured, which correspond to the (112) and (020) planes for kesterite CZTS. Particularly, the lying nanoplates investigated in Figure 3.12d show the lattice spacings compatible with (112) and (020) planes. These observations indicate that the growth of (112) and (020) planes is favored, while the growth in the direction of corresponding zone-axis, or [201] is strongly inhibited. The above results explain why the faceted and nanoplates shapes are formed.

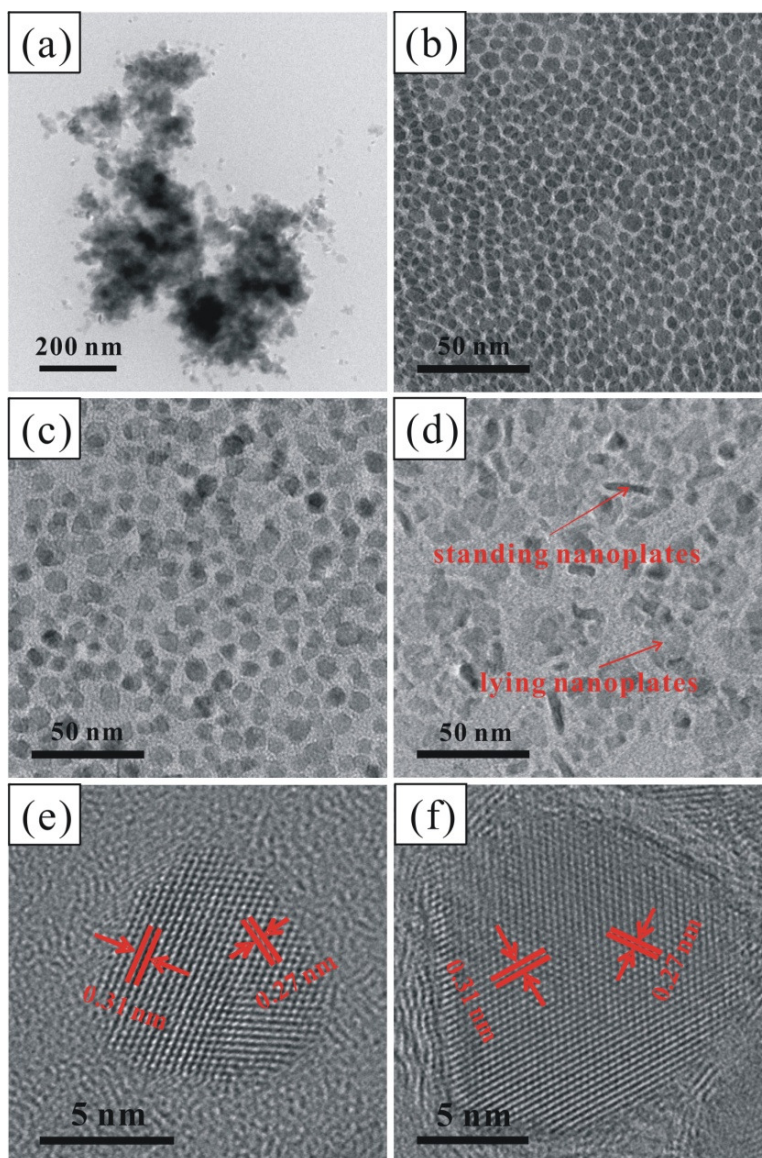


**Figure 3.12.** TEM images of CZTS nanoparticles with (a) 0 ml, (b) 0.5 ml, (c) 1 ml, (d) 2ml OLA, and HRTEM images of CZTS nanoparticles with (e) 1 ml OLA and (f) 2 ml OLA.

From the TEM micrographs shown in Figure 3.12, there is a significant change in the size and shape of the nanoparticles with respect to the amount of surfactant. The reason for this can be understood by looking at the dynamics of surfactants in the reaction mixture. It was well known that the surfactant plays a critical role in determining the size and shape of the nanostructures.<sup>27, 36, 37</sup> The packing density of the ligand on the nanoparticles

surface determines the growth rate of that surface. At low packing density, the surface could be easily exposed to the reaction environment therefore that surface is more reactive. At high packing density, the surface is well protected by abundant ligands, and that the growth on that surface is inhibited. At low surfactant supply, in this case 0.5 ml OLA, the ligands are relative uniformly distributed on all the CZTS surfaces and not sufficient to fully inhibit growth on any facet. As a result, the near spherical shape will be obtained. As the amount of OLA increases to 1 ml, the supply of ligands became abundant. Instead of distributing uniformly on all surfaces, additional OLA favors certain surfaces, which results in the inhibition of growth on these surfaces. Therefore, the surfaces that are favored by OLA grow slowly and facets are formed. Based on high-resolution TEM images, it was found the crystal growth along  $[20\bar{1}]$  direction is inhibited, which suggests that the OLA surfactants pack in highest density in its corresponding lattice planes than other planes. As the amount of OLA increases further to 2 ml, the selectivity of ligand on nanoparticles surface are further enhanced, with much more ligand on just the one plane, leading to the formation of nanoplates.

The major advantage of the separation in the role of solvent and ligand is that it offer better size and shape control than the OLA synthesis. In this work, we managed to some extent to control the shape of CZTS nanoparticles by tuning the amount of surfactants: aggregated form (0 ml OLA), spherical (0.5 ml OLA), faceted (1 ml OLA) and nanoplates (2 ml OLA). Further studies may focus on other solvent-ligand combination to achieve other morphologies. The selection of solvent may include hexadecane ( $C_{16}H_{34}$ )



and octadecane ( $C_{18}H_{38}$ ). And the selection of surfactant may include hexadecylamine (HDA), trioctylphosphine (TOP) and trioctylphosphine oxide (TOPO).

### 3.4 Conclusions

In conclusion, CZTS nanoparticles were successfully synthesized using hot injection method. It was found that at low reaction temperature, the binary  $Cu_{2-x}S$  and ternary CTS were synthesized together with quaternary CZTS phases. At reaction temperature of 220 °C and above, pure CZTS phases are favored. Detailed XRD analysis of CZTS nanoparticles synthesized at 240 °C confirmed that pure kesterite CZTS were indeed formed at this temperature. The average ratio of Cu, Zn, Sn and S was estimated to be 1.96: 0.80: 1.05:4.19. The average size of CZTS nanoparticles was determined to be 19.8 nm. The STEM-EDS analysis shows that the Cu, Zn, Sn and S are distributed uniformly in the nanoparticles. The optical band gap of the CZTS nanoparticles was estimated to be 1.55 eV based on UV-vis-NIR absorption measurements. The reaction time will greatly affect the size of nanoparticles. CZTS nanoparticles formed immediately after injection of S precursor. From 0 min to 30 min, the average size of the nanoparticles gradually increased and the size distribution became narrower. With longer reaction time, the nanoparticles show the phenomenon of Ostwald ripening. The size and shape of nanoparticles could be controlled through solvent-ligand optimization. With DCB as the solvent and OLA as the ligand, sub-micrometer size clusters (0 ml OLA), near-spherical shape (0.5 ml OLA), faceted (1 ml OLA), and nanoplates (2 ml OLA) CZTS nanostructures were synthesized.



### References

1. Daniel, M.-C.; Astruc, D., Gold nanoparticles: assembly, supramolecular chemistry, quantum-size-related properties, and applications toward biology, catalysis, and nanotechnology. *Chemical Reviews* **2003**, 104, (1), 293-346.
2. Shipway, A. N.; Katz, E.; Willner, I., Nanoparticle arrays on surfaces for electronic, optical, and sensor Applications. *ChemPhysChem* **2000**, 1, (1), 18-52.
3. Burda, C.; Chen, X.; Narayanan, R.; El-Sayed, M. A., Chemistry and properties of nanocrystals of different shapes. *Chemical Reviews* **2005**, 105, (4), 1025-1102.
4. Murray, C. B.; Kagan, C. R.; Bawendi, M. G., Synthesis and characterization of monodisperse nanocrystals and close-packed nanocrystals assemblies. *Annual Review of Materials Science* **2000**, 30, (1), 545-610.
5. Panthani, M. G.; Akhavan, V.; Goodfellow, B.; Schmidtke, J. P.; Dunn, L.; Dodabalapur, A.; Barbara, P. F.; Korgel, B. A., Synthesis of  $\text{CuInS}_2$ ,  $\text{CuInSe}_2$ , and  $\text{Cu}(\text{In}_x\text{Ga}_{1-x})\text{Se}_2$  (CIGS) nanocrystal "inks" for printable photovoltaics. *Journal of the American Chemical Society* **2008**, 130, (49), 16770-16777.
6. Gur, I.; Fromer, N. A.; Geier, M. L.; Alivisatos, A. P., Air-stable all-inorganic nanocrystal solar cells processed from solution. *Science* **2005**, 310, (5747), 462-465.
7. Guo, Q.; Ford, G. M.; Yang, W.-C.; Walker, B. C.; Stach, E. A.; Hillhouse, H. W.; Agrawal, R., Fabrication of 7.2% efficient CZTSSe solar cells using CZTS nanocrystals. *Journal of the American Chemical Society* **2010**, 132, (49), 17384-17386.
8. Steinhagen, C.; Panthani, M. G.; Akhavan, V.; Goodfellow, B.; Koo, B.; Korgel, B. A., Synthesis of  $\text{Cu}_2\text{ZnSnS}_4$  nanocrystals for use in low-cost photovoltaics. *Journal of the American Chemical Society* **2009**, 131, (35), 12554-12555.
9. Riha, S. C.; Parkinson, B. A.; Prieto, A. L., Solution-based synthesis and characterization of  $\text{Cu}_2\text{ZnSnS}_4$  nanocrystals. *Journal of the American Chemical Society* **2009**, 131, (34), 12054-12055.
10. Guo, Q.; Hillhouse, H. W.; Agrawal, R., Synthesis of  $\text{Cu}_2\text{ZnSnS}_4$  nanocrystal ink and its use for solar cells. *Journal of the American Chemical Society* **2009**, 131, (33), 11672-11673.
11. Kameyama, T.; Osaki, T.; Okazaki, K.-i.; Shibayama, T.; Kudo, A.; Kuwabata, S.; Torimoto, T., Preparation and photoelectrochemical properties of densely immobilized  $\text{Cu}_2\text{ZnSnS}_4$  nanoparticle films. *Journal of Materials Chemistry* **20**, (25), 5319-5324.

12. Zhou, Y.-L.; Zhou, W.-H.; Du, Y.-F.; Li, M.; Wu, S.-X., Sphere-like kesterite  $\text{Cu}_2\text{ZnSnS}_4$  nanoparticles synthesized by a facile solvothermal method. *Materials Letters* **65**, (11), 1535-1537.
13. Cao, M.; Shen, Y., A mild solvothermal route to kesterite quaternary  $\text{Cu}_2\text{ZnSnS}_4$  nanoparticles. *Journal of Crystal Growth* **318**, (1), 1117-1120.
14. Wang, C. C., Chen; Cao, Yun; Fang, Wei; Zhao, Lijuan; Xu, Xiaofeng Synthesis of  $\text{Cu}_2\text{ZnSnS}_4$  Nanocrystallines by a Hydrothermal Route. *Japanese Journal of Applied Physics* **2011**, 50, (6).
15. Xi, L.; Lam, Y. M., Controlling Growth of CdSe Nanowires through Ligand Optimization. *Chemistry of Materials* **2009**, 21, (15), 3710-3718.
16. Panthani, M. G.; Akhavan, V.; Goodfellow, B.; Schmidtke, J. P.; Dunn, L.; Dodabalapur, A.; Barbara, P. F.; Korgel, B. A., Synthesis of  $\text{CuInS}_2$ ,  $\text{CuInSe}_2$ , and  $\text{Cu}(\text{In}_x\text{Ga}_{1-x})\text{Se}_2$  (CIGS) Nanocrystal "inks" for Printable Photovoltaics. *Journal of the American Chemical Society* **2008**, 130, (49), 16770-16777.
17. Acharya, K. P.; Hewa-Kasakarage, N. N.; Alabi, T. R.; Nemitz, I.; Khon, E.; Ullrich, B.; Anzenbacher, P.; Zamkov, M., Synthesis of  $\text{PbS}/\text{TiO}_2$  colloidal heterostructures for photovoltaic applications. *Journal of Physical Chemistry C* **2010**, 114, (29), 12496-12504.
18. Deng, Z. T.; Mansuripur, M.; Muscat, A. J., Simple colloidal synthesis of single-crystal Sb-Se-S nanotubes with composition dependent band-gap energy in the near-infrared. *Nano Letters* **2009**, 9, (5), 2015-2020.
19. Kameyama, T.; Osaki, T.; Okazaki, K.-i.; Shibayama, T.; Kudo, A.; Kuwabata, S.; Torimoto, T., Preparation and photoelectrochemical properties of densely immobilized  $\text{Cu}_2\text{ZnSnS}_4$  nanoparticle films. *Journal of Materials Chemistry* **2010**, 20, (25), 5319-5324.
20. Scragg, J. J., Studies of  $\text{Cu}_2\text{ZnSnS}_4$  films prepared by sulphurisation of electrodeposited precursors. *University of Bath* **2010**, Diss.
21. Cheng, A. J.; Manno, M.; Khare, A.; Leighton, C.; Campbell, S. A.; Aydil, E. S., Imaging and phase identification of  $\text{Cu}_2\text{ZnSnS}_4$  thin films using confocal Raman spectroscopy. *Journal of Vacuum Science & Technology A: Vacuum, Surfaces, and Films* **2011**, 29, (5), 051203-11.
22. Altosaar, M.; Raudoja, J.; Timmo, K.; Danilson, M.; Grossberg, M.; Krustok, J.; Mellikov, E.,  $\text{Cu}_2\text{Zn}_{1-x}\text{Cd}_x\text{Sn}(\text{Se}_{1-y}\text{S}_y)_4$  solid solutions as absorber materials for solar cells. *physica status solidi (a)* **2008**, 205, (1), 167-170.

23. Munce, C. G.; Parker, G. K.; Holt, S. A.; Hope, G. A., A Raman spectroelectrochemical investigation of chemical bath deposited  $\text{Cu}_x\text{S}$  thin films and their modification. *Colloids and Surfaces A: Physicochemical and Engineering Aspects* **2007**, 295, (1-3), 152-158.
24. Cheng, Y. C.; Jin, C. Q.; Gao, F.; Wu, X. L.; Zhong, W.; Li, S. H.; Chu, P. K., Raman scattering study of zinc blende and wurtzite  $\text{ZnS}$ . *Journal of Applied Physics* **2009**, 106, (12), 123505-5.
25. Guan, H.; Shen, H.; Gao, C.; He, X., Structural and optical properties of  $\text{Cu}_2\text{SnS}_3$  and  $\text{Cu}_3\text{SnS}_4$  thin films by successive ionic layer adsorption and reaction. *Journal of Materials Science: Materials in Electronics* **2013**, 24, (5), 1490-1494.
26. Sarswat, P. K.; Free, M. L.; Tiwari, A., Temperature-dependent study of the Raman A mode of  $\text{Cu}_2\text{ZnSnS}_4$  thin films. *physica status solidi (b)* **2011**, 248, (9), 2170-2174.
27. Yin, Y.; Alivisatos, A. P., Colloidal nanocrystal synthesis and the organic-inorganic interface. *Nature* **2005**, 437, (7059), 664-670.
28. Rath, T.; Haas, W.; Pein, A.; Saf, R.; Maier, E.; Kunert, B.; Hofer, F.; Resel, R.; Trimmel, G., Synthesis and characterization of copper zinc tin chalcogenide nanoparticles: Influence of reactants on the chemical composition. *Solar Energy Materials and Solar Cells* 101, (0), 87-94.
29. Woo, K.; Kim, Y.; Moon, J., A non-toxic, solution-processed, earth abundant absorbing layer for thin-film solar cells. *Energy & Environmental Science* **2012**, 5, (1), 5340-5345.
30. Katagiri, H.,  $\text{Cu}_2\text{ZnSnS}_4$  thin film solar cells. *Thin Solid Films* **2005**, 480-81, (0), 426-432.
31. Davis, R. E.; Nakshbendi, H. F., Sulfur in amine solvents. *Journal of the American Chemical Society* **1962**, 84, (11), 2085-2090.
32. Hodgson, W. G.; Buckler, S. A.; Peters, G., Free radicals in amine solutions of elemental sulfur. *Journal of the American Chemical Society* **1963**, 85, (5), 543-546.
33. Thomson, J. W.; Nagashima, K.; Macdonald, P. M.; Ozin, G. A., From sulfur-amine solutions to metal sulfide nanocrystals: peering into the oleylamine-sulfur black box. *Journal of the American Chemical Society* **2011**, 133, (13), 5036-5041.
34. Manna, L.; Scher, E. C.; Alivisatos, A. P., Synthesis of soluble and processable rod-, arrow-, teardrop-, and tetrapod-shaped  $\text{CdSe}$  nanocrystals. *Journal of the American Chemical Society* **2000**, 122, (51), 12700-12706.
35. Johnson, C. J.; Dujardin, E.; Davis, S. A.; Murphy, C. J.; Mann, S., Growth and form of gold nanorods prepared by seed-mediated, surfactant-directed synthesis. *Journal of Materials Chemistry* **2002**, 12, (6), 1765-1770.

36. Heinz, H.; Vaia, R. A.; Farmer, B. L., Relation between packing density and thermal transitions of alkyl chains on layered silicate and metal surfaces. *Langmuir* **2008**, 24, (8), 3727-3733.
37. Möbius, D. M., R.; Fainerman, V. R., Surfactants: chemistry, interfacial properties, applications. *Elsevier Science* **2002**, 13, 1-661

# Chapter 4: Controlled synthesis of kesterite and wurtzite CZTS nanoparticles through sulfur precursor

## 4.1 Introduction

As discussed in the previous in Chapter 3, the size, shape and stoichiometry of kesterite CZTS nanocrystals can be controlled generally through the understanding and controlling the reaction kinetics. On top of these, it is also possible to alter the crystal structures by taking into account of the reactivity of precursors. In this chapter, the synthesis and characterization of kesterite, wurtzite, mixed kesterite-wurtzite phases will be presented. In an earlier work, Xu et al. reported that the wurtzite structure of CIS shows better electron excitation and transport properties than the chalcopyrite structure (similar crystal structure with CZTS kesterite structure).<sup>1</sup> These findings suggest that the changing of crystal structures might result in variations in material properties. Therefore, in this work, the optical and electrical properties of CZTS kesterite and wurtzite structures are also evaluated and compared.

The ternary or quaternary semiconductor compounds can be considered as the derivatives of binary semiconductor compound with a series of cation substitutions.<sup>2-4</sup> This suggests that the crystal structures of the ternary or quaternary semiconductor compounds could derive from the binary compounds. Essentially, the rule is that the total charges of all cations after the substitutions must be equivalent with that before substitution in order to

maintain charge neutrality of the compound. For instance, two  $B^{2+}$  ions from the Periodic Table group II may be replaced by one  $A^+$  ion from group I and one  $C^{3+}$  ion from group III; two  $C^{3+}$  ions (group III) could also be substituted by one  $B^{2+}$  ion (group II) and one  $D^{4+}$  ion (group IV).

Figure 4.1 describes the cation substitutions of binary ZnS compound to form ternary CuInS<sub>2</sub> and quaternary Cu<sub>2</sub>ZnSnS<sub>4</sub> compounds. ZnS (II-VI) consists of Zn<sup>2+</sup> cation and S<sup>2-</sup> anion. With the cation substitutions, two Zn<sup>2+</sup> ions can be replaced by one Cu<sup>+</sup> ion and one In<sup>3+</sup> ion to form ternary CuInS<sub>2</sub> (I-III-VI<sub>2</sub>) compound. Similarly, the quaternary Cu<sub>2</sub>ZnSnS<sub>4</sub> (I<sub>2</sub>-II-IV-VI<sub>2</sub>) compound could be obtained by cation substitution of ternary CuInS<sub>2</sub> (I-III-VI<sub>2</sub>) compound. The substitution is performed by replacing two In<sup>3+</sup> ions with one Zn<sup>2+</sup> ion and one Sn<sup>4+</sup> ion. Therefore, the ternary CuInS<sub>2</sub> and quaternary Cu<sub>2</sub>ZnSnS<sub>4</sub> are derived from ZnS through cation substitutions. In addition, the effective ionic radius of Zn<sup>2+</sup> (74 pm), Cu<sup>+</sup> (77 pm), In<sup>3+</sup> (80 pm) and Sn<sup>4+</sup> (69 pm) are very similar.<sup>5</sup> Therefore, it is very likely for CuInS<sub>2</sub> as well as Cu<sub>2</sub>ZnSnS<sub>4</sub> to adopt the crystal structure of ZnS with the relevant cation substitutions.

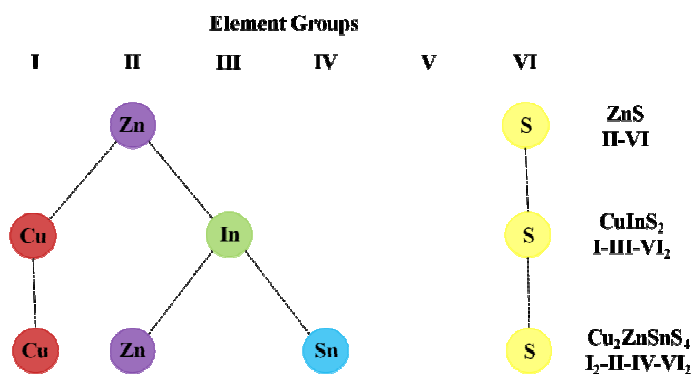


**Figure 4.1.** Close relationship of ternary CuInS<sub>2</sub> and quaternary Cu<sub>2</sub>ZnSnS<sub>4</sub> to binary ZnS with cation substitutions.

ZnS compound crystallizes mainly in two polymorphs: zinc blende and wurtzite structures.<sup>6-8</sup> Similarly, the crystal structures of  $\text{CuInS}_2$  and  $\text{Cu}_2\text{ZnSnS}_4$  could also be categorized into zinc blende type and wurtzite type. As there are more cations in the case of the ternary and quaternary compounds, the crystal structures of ternary  $\text{CuInS}_2$  and quaternary  $\text{Cu}_2\text{ZnSnS}_4$  have an additional complication related to the orderings of cations. For example, in the zinc blende type  $\text{CuInS}_2$ , the ordering of cation layers and anion layers may alternate either as  $\text{CuIn/SS/CuIn/SS}$  (Chalcopyrite) or as  $\text{CuCu/SS/InIn/SS}$  (CuAu-like) along the crystallographic c-direction to form two distinctly different crystal structures.<sup>9</sup> For  $\text{Cu}_2\text{ZnSnS}_4$ , the number of cations increases to three (Cu, Zn, Sn) compared to two (Cu, In) for  $\text{CuInS}_2$ . As a result, more variations of atom orderings as well as crystal structures could be expected.

Until now, the kesterite, stannite, wurtzite, wurtzite-kesterite and wurtzite-stannite structures of CZTS have been reported.<sup>10-12</sup> In the early works, CZTS was demonstrated to crystallize in zinc blend type structures, of which kesterite and stannite are the two low-energy polytypes.<sup>10, 13, 14</sup> These two polytypes have different cation orderings: the kesterite lattice has a tetragonal unit cell with alternating cation and anion layers in the ordering of  $\text{CuZn/SS/CuSn/SS}$  along crystallographic c-direction, while for the stannite lattice this ordering changes to  $\text{CuCu/SS/ZnSn/SS}$ .<sup>15</sup> Recently, the wurtzite type CZTS has been reported by several different research groups. Lu and co-workers synthesized wurtzite CZTS nanostructures, which adopted a hexagonal unit cell.<sup>11</sup> The synthesis of wurtzite CZTS nanorods were also reported.<sup>16</sup> More recently, wurtzite-related phases, or more accurately wurtzite-kesterite and wurtzite-stannite phases, were reported.<sup>12, 17</sup> Lu et

al. attributed the reason for the formation of wurtzite phase to the use of dodecanethiol, while Regulacio et al. claimed it was due to the influence of surfactant.<sup>11, 17</sup>

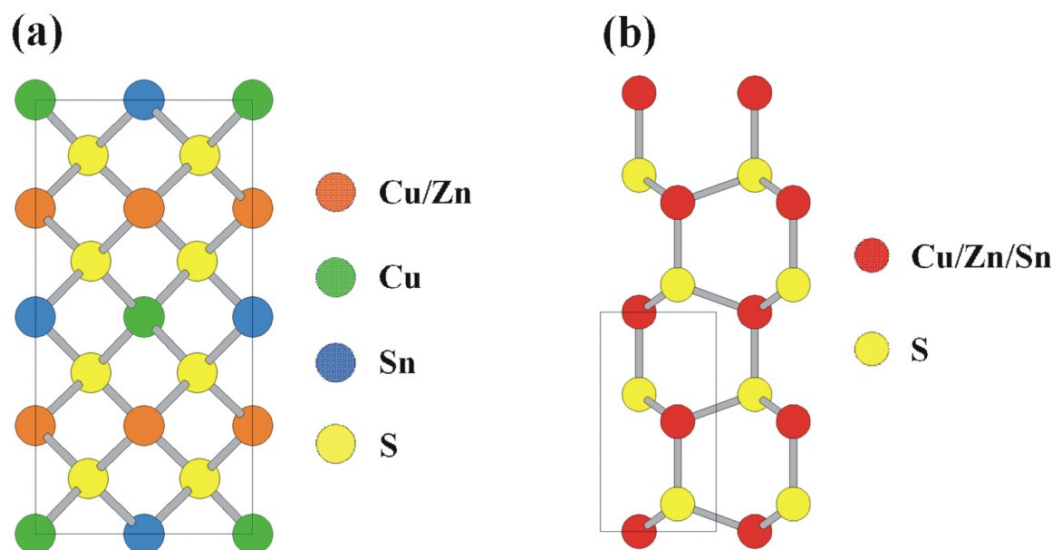


**Figure 4.2.** The unit cell structure of CZTS (a) kesterite (in the Cu-Zn layer, the Cu and Zn ions have equal occupancy of 0.5) and (b) wurtzite (the red ion represent Cu, Zn or Sn ions with the 0.5 occupancy of Cu ion, 0.25 occupancy of Zn ion and 0.25 occupancy of Sn ions).

Kesterite and wurtzite are two common CZTS crystal structures and have been intensively studied. Figure 4.2 shows the unit cell structures of CZTS - kesterite and wurtzite. The kesterite structure (Figure 4.2a) has a tetrahedral crystal structure similar to the zinc blende structures. The cation layers and anion layers alternates as CuSn/SS/CuZn/SS. In the Cu-Zn layer, due to the small energy differences, the positions of Cu and Zn are interchangeable, and the Cu and Zn ions can be considered as randomly distributed in this layer. The wurtzite structure (Figure 4.2b) takes the hexagonal closed packed crystal structure with Cu, Zn and Sn ions residing in the interstices between S ions. The ratio of Cu, Zn and Sn ions are maintained at 2: 1: 1. The difference in crystal



structure may have great effect on material property. For examples, studies based on density functional theory show that the kesterite structure is more thermodynamically stable than stannite polytypes of CZTS.<sup>14, 18</sup> The wurtzite structures of CZTS were only reported not long ago, and thus little was known about its optical and electrical properties.

Various synthesis methods have been developed to synthesize the two crystal structures. Guo et al. synthesized kesterite CZTS nanoparticles using the hot injection method and demonstrated their solar cell performance.<sup>10</sup> Todorov et al. deposited kesterite CZTSSe thin film by spin-coating hybrid solution-particles precursors in hydrazine.<sup>19</sup> The nanoparticles ink approach and hydrazine approach obtained high efficiencies due to the high quality of CZTSSe film prepared using respective methods.<sup>20, 21</sup> Scragg et al. prepared kesterite CZTS thin film using electrodeposition method.<sup>22</sup> Recently, Lu et al. synthesized wurtzite CZTS nanoparticles for the first time.<sup>11</sup> Not long ago, the synthesis of wurtzite CZTS nanorods were reported.<sup>16</sup> Despite excellent progress in the synthesis of CZTS kesterite and wurtzite, the key factors that determine the formation of the two phases are still not quite clear. In order to effectively control the phases, it is important to understand the formation mechanisms of the two phases. In addition, a detailed study of how the crystal structures may alter the optical and electrical properties of the two phases will be very useful for their application in thin film solar cells.

In this work, we demonstrated that it is possible to control the synthesis of kesterite, wurtzite and mixed kesterite-wurtzite CZTS nanoparticles by simply tuning the sulfur sources. This is due to a variation in the reactivity of the various sulfur sources. Three sulfur sources were used and they are elemental sulfur (S), 1-dodecanethiol (DDT) and

thioacetamide (TAA). The formation mechanism of CZTS kesterite and wurtzite were also investigated and discussed. The effects of the crystal structures on the optical absorbance, conduction band and valence band energy levels as well as the photoresponse were also studied.

### 4.2 Experimental details

**Materials:** Copper (II) acetate ( $\text{Cu}(\text{OAc})_2$ , Aldrich, 98%), zinc chloride anhydrous ( $\text{ZnCl}_2$ , Sigma-Aldrich, 99.99%), tin (IV) chloride pentahydrate ( $\text{SnCl}_4 \cdot 5\text{H}_2\text{O}$ , Sigma-Aldrich, 98%), elemental sulfur (S, Aldrich), oleylamine (OLA, Aldrich, 70%), 1-dodecanethiol (DDT, Aldrich, 98%), thioacetamide (TAA, Sigma-Aldrich, 98%), toluene (Aik Moh Paints & Chemicals) and ethanol (Aik Moh Paints & Chemicals, 95%) were purchased and used as received.

**Synthesis:** The synthesis was carried out using hot injection method with the similar experimental procedures to those Chapter 3. The reaction temperature was set at 235 °C and a fixed reaction time of 1 hour was used. The sulfur precursor was prepared by dissolving or mixing 1 mmol sulfur source with 1 ml of OLA at room temperature. In this work, three types of sulfur source were used, and they are elemental sulfur (S), 1-dodecanethiol (DDT) as well as thioacetamide (TAA). The reaction temperature was maintained at 235 °C for 1 hour before cooling down to room temperature. The as-prepared CZTS nanoparticles were washed three times using toluene and ethanol. In the following session, the final product obtained synthesized from elemental S, DDT and TAA will be denoted as sample S, sample DDT and sample TAA respectively.

**Characterizations:** The Grazing Incidence X-ray diffraction (GIXRD) patterns were collected using Bruker D8 Advance equipped with Cu K $\alpha$  radiation ( $\lambda = 1.54 \text{ \AA}$ ). The diffraction was taken at a fixed incident angle of  $1^\circ$ , and collected from  $20^\circ$  to  $70^\circ$  in steps of  $0.05^\circ$ . Rietveld refinement was performed using TOPAS V3 software with fundamental parameter peak profile for CZTS sample. A five-coefficient Chebychev polynomial and  $1/x$  background, a zero error, scale factor, lattice parameters and crystal size were successively refined. The Raman analysis was performed using a WITec Confocal Raman Spectroscopy with a 488 nm laser. The atomic ratio of Cu, Zn, Sn and S was measured with an accelerating voltage of 20 keV using an Oxford X-MAX energy dispersive X-ray spectroscopy (EDS) detector which is equipped on a JEOL JSM 7600F FESEM. The transmission electron microscopy (TEM) analysis was performed using a JOEL JSM – 2100F TEM at accelerating voltage of 200 kV. The UV-Vis absorption spectra were obtained using a Shimadzu UV-Vis-NIR PerkinElmerLambda 900 spectrophotometer. Cyclic voltammetry (CV) measurements were performed on an Autolab PG302N electrochemical workstation. Carbon, gold and Ag/AgCl electrodes were used as working electrode, counter electrodes and reference electrode respectively.

### 4.3 Results and Discussion

The effect of CZTS crystal structures on the optical and electrical properties can only be investigated if the crystal structures can be synthesized. Therefore, the controlled synthesis of the kesterite, wurtzite and mixed kesterite-wurtzite structures will be presented first. Next, the three crystal structures are investigated using XRD, Raman spectroscopy and high-resolution TEM. Following that the formation mechanisms for

kesterite and wurtzite phases will be proposed based on time-dependent studies. Finally, the impact of the structures on the optical and electrical properties will be examined.

### 4.3.1 Synthesis of CZTS nanoparticles with different phases

In the synthesis of CZTS nanoparticles, the precursors may have strong effect on the phase formed. In general, kesterite structures are obtained when elemental S is used as the sulfur source, whereas the wurtzite structures are mostly produced with alkyl thiols as sulfur source.<sup>10, 11, 13, 15, 17</sup> However, for these synthesis of kesterite and wurtzite discussed in literatures, other experimental parameters, such as solvents, surfactants, concentration, reaction temperature and time, are also varied. These variables make it difficult to conclusively determine the key parameter that determines the formation of kesterite and wurtzite. We think that the crystal structures obtained is highly dependent on the reactivity of the precursors and in order to show this, in this work, we fixed all other experimental conditions and only vary the sulfur source. The three common sulfur sources - elemental sulfur (S), 1-dodecanthiol (DDT) and thioacetamide (TAA) were used.

Figure 4.3 presents the XRD patterns of CZTS nanoparticles synthesized using various precursors (S, DDT and TAA) with  $2\theta$  ranging from  $20^\circ$  to  $70^\circ$ . They are denoted using the sulfur precursors used in the synthesis for convenience, i.e., sample S, sample DDT and sample TAA. It was found that the XRD pattern of sample S matched very well with kesterite CZTS database (JCPDS no. 26-0575). The XRD pattern shows three major peaks at  $28.5^\circ$ ,  $47.6^\circ$  and  $56.3^\circ$ , corresponding to (112), (220) and (312) lattice planes respectively. And the minor peaks at  $23.1^\circ$ ,  $33.0^\circ$ ,  $59.0^\circ$  and  $69.3^\circ$  could also be noticed

and all of them could be attributed to kesterite CZTS. These results indicate the formation of pure kesterite phase using elemental S as the sulfur source. For sample DDT, a completely different XRD pattern is obtained. The major XRD peaks at  $26.9^\circ$ ,  $28.3^\circ$ ,  $30.2^\circ$ ,  $39.5^\circ$ ,  $47.6^\circ$ ,  $51.0^\circ$  and  $56.2^\circ$  were observed. All these peaks match well with wurtzite CZTS, which indicates that wurtzite CZTS was produced with DDT as the sulfur source. It is also noticed that  $23.3^\circ$ ,  $33.8^\circ$  and  $38.1^\circ$  could be observed, which could be attributed to  $\text{Cu}_7\text{S}_4$  (JCPDS no. 23-0958) binary phase. The XRD results suggest that sample DDT consists of a majority of wurtzite CZTS phase with a minority of  $\text{Cu}_7\text{S}_4$  binary phase. The rietveld refinement of sample DDT could be found in Appendix B. The XRD pattern of sample TAA shows peak positions at  $26.9^\circ$ ,  $28.4^\circ$ ,  $30.2^\circ$ ,  $33.1^\circ$ ,  $39.5^\circ$ ,  $47.6^\circ$ ,  $51.0^\circ$ ,  $56.2^\circ$  and  $69.3^\circ$ . These peak positions agree well the combination of kesterite and wurtzite CZTS diffraction peaks, which implies that sample TAA may contains a mixture of kesterite and wurtzite phases. In order to figure out the relative amount of each phase, rietveld refinement was performed (Appendix B). It is found that 50.3 wt% of kesterite and 49.7 wt% of wurtzite were formed.

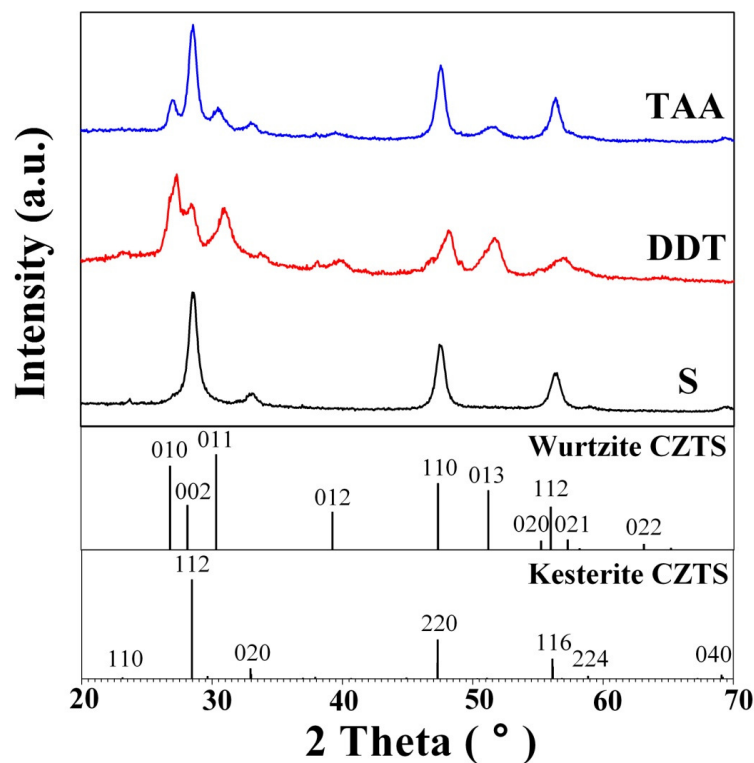


**Figure 4.3.** The XRD patterns of as synthesized samples using elemental S, DDT and TAA as the sulfur source respectively. The XRD database for kesterite CZTS and wurtzite CZTS are also presented and indexed for comparison.

Beside structural analysis using XRD, Raman spectroscopy was also performed to confirm the formation of CZTS phases. The Raman shifts of kesterite CZTS were reported to be  $288\text{ cm}^{-1}$ ,  $338\text{ cm}^{-1}$ , and  $368\text{ cm}^{-1}$ , where the  $338\text{ cm}^{-1}$  peak is the strongest peak. A slight shift in Raman peak position can often be observed which may be due to differences in preparation methods, composition and so on.<sup>23</sup> The wurtzite CZTS were published to have similar Raman shifts to that of the kesterite structure. Singh et al. reported a strong Raman peak at  $333\text{ cm}^{-1}$  for wurtzite CZTS nanorods.<sup>16</sup> As shown in Figure 4.4, the Raman shifts of sample S exhibits a strong single peak at  $336\text{ cm}^{-1}$ , which is indicative of kesterite CZTS. The two shoulder peaks at around  $288$  and  $368\text{ cm}^{-1}$  could

also be noticed, which also match well to kesterite CZTS. For sample DDT, the major peak at  $334\text{ cm}^{-1}$  agrees well with CZTS. The two shoulder peaks in this case are not very obvious. Combining the XRD with Raman results, it can be concluded that wurtzite CZTS phase were formed when DDT is used. A strong peak at  $336\text{ cm}^{-1}$  is also observed for sample TAA. In the case of TAA, both kesterite CZTS and wurtzite CZTS phases can be observed. For all three precursors, the Raman results confirm the formation of quaternary CZTS phases rather than binary or ternary phases.

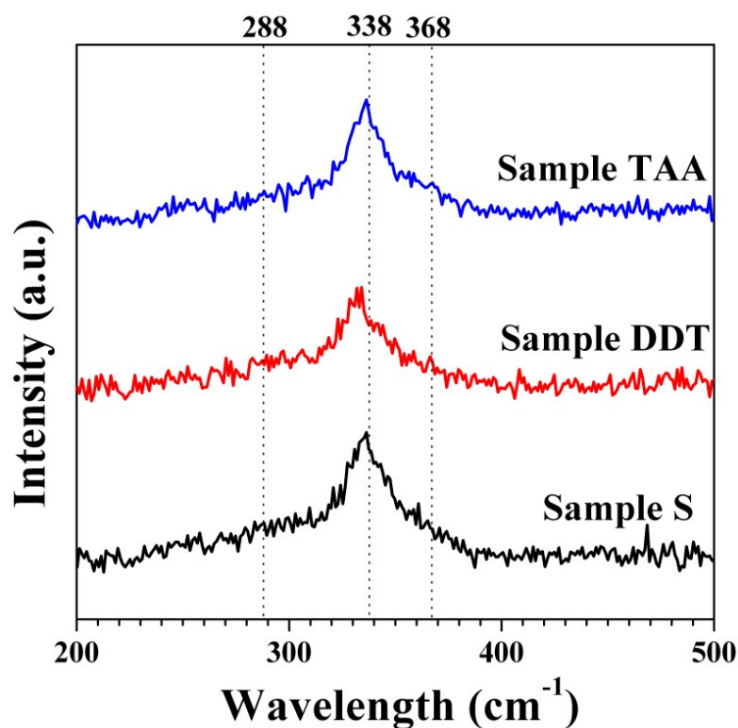


**Figure 4.4.** The Raman shifts of sample S, sample DDT and sample TAA. The peak positions of  $288$ ,  $338$  and  $368\text{ cm}^{-1}$  are marked by dotted lines.

Figure 4.5 shows the TEM and HRTEM images of the as-synthesized CZTS nanoparticles. TEM micrographs of CZTS nanoparticles synthesized using elemental S as the sulfur source (kesterite) are shown in Figure 4.5a and b. It was found that the

nanoparticles have irregular shapes and the average size of the nanoparticles was found to be  $9.8 \pm 6.5$  nm. Lattice spacings of 0.31 nm and 0.27 nm were determined which corresponds to the d-spacings of (112) planes and (020) planes respectively for kesterite CZTS. In Figure 4.5c, the TEM images of CZTS nanoparticles using DDT (wurtzite) is shown. The nanoparticles are nearly spherical with an average size of  $12.9 \pm 1.2$  nm.

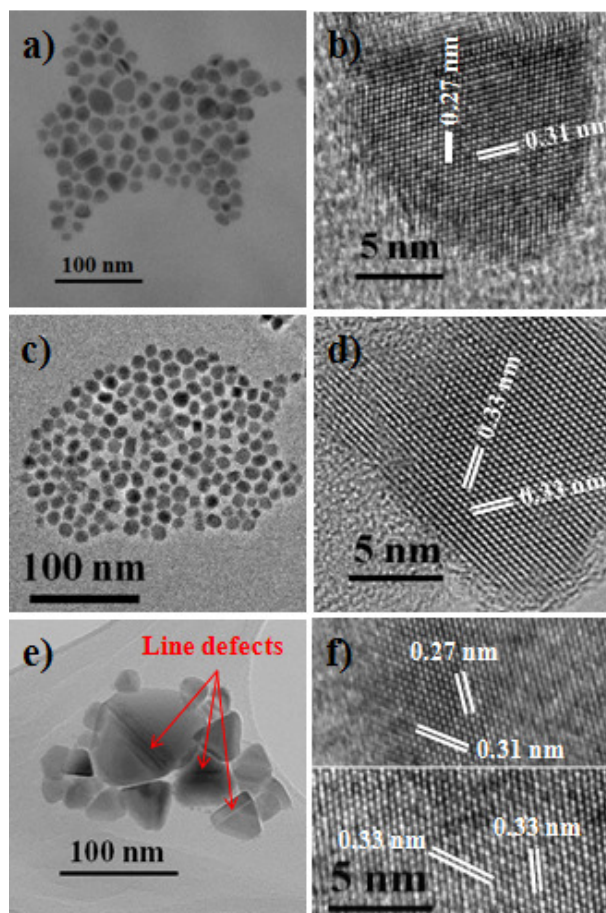


**Figure 4.5:** The TEM images of (a) sample S, (c) sample DDT, (e) sample TAA, and the high-resolution TEM images of (b) sample S, (d) sample DDT, (f) sample TAA. The lattice spacing is calculated and labeled in the high resolution images.

From the HRTEM shown in Figure 4.5d, it is possible to again determine two lattice spacings of 0.33 nm each, which is consistent with the d-spacings of (110) planes and



(100) planes for wurtzite type CZTS. TEM micrographs of CZTS nanoparticles synthesized using TAA (mixture of kesterite and wurtzite) can be seen in Figure 4.5e and f show. Interestingly for this sample, line defects can be clearly seen in these nanoparticles, which suggests a rapid crystal growth process. In the high-resolution TEM images as shown in Figure 4.5f, the kesterite and wurtzite CZTS nanoparticles can be observed to be two separate nanoparticles. In another work, Fan et al. also reported the formation of mixed kesterite and wurtzite CZTS, whereas their kesterite and wurtzite phases co-exist on the same particle.<sup>24</sup> It is also worth noting that the kesterite CZTS nanoparticles (Figure 4.5a) generally have a polydisperse size distribution, which is probably because the reaction is too fast and it is difficult to separate the nucleation and growth stages so that both nucleation and growth happened at the same time. On the other hand, the wurtzite CZTS nanoparticles (Figure 4.5c) show a mono-dispersed size distribution, which suggests a slow reaction dynamics.

### 4.3.2 Growth mechanisms for kesterite and wurtzite

In order to control the development of kesterite and wurtzite phases, it is important to understand the growth mechanisms of the two phases. Time-dependent studies were performed for sample S and sample DDT. Figure 4.6 shows the XRD patterns for sample S at 10 min, 30 min, 60 min and 120 min after the injection of sulfur source. The XRD pattern of the sample after 10 min has three major peaks at  $28.5^\circ$ ,  $47.6^\circ$  and  $56.3^\circ$  which are the characteristic peaks for kesterite CZTS. The XRD results indicate that well crystalline kesterite CZTS has already formed after 10 min. When the reaction time was increased to 30 min, 60 min and 120 min, no significant changes of the XRD patterns

could be noticed and all XRD patterns matched well with kesterite CZTS. It is worth to note that no intermediate products or impurity phases can be detected throughout the time investigated. These findings suggest that the formation of kesterite CZTS occurred rapidly and there is very little control possible.

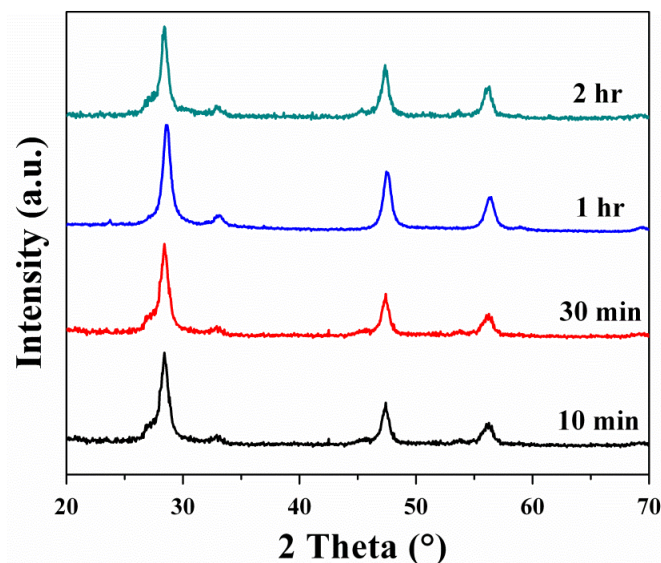


**Figure 4.6:** The XRD patterns of CZTS nanoparticles synthesized using elemental S as the sulfur source with different reaction timings of 10 min, 30 min, 60 min and 120 min.

Figure 4.7 presents the XRD patterns for sample DDT reacted for 10 min, 30 min, 60 min and 120 min. (Please refer to Appendix C for the TEM images) The XRD pattern for 10 min matches well with  $\text{Cu}_7\text{S}_4$  binary sulfide phase, indicating the selective reaction of DDT with Cu species. As the reaction time increases to 30 min, in addition to the dominant  $\text{Cu}_7\text{S}_4$  phase, the XRD peaks at  $26.9^\circ$ ,  $30.2^\circ$ , and  $51.0^\circ$  are observed, which suggests the formation of wurtzite CZTS phases. At 60 min, the major XRD peaks at  $26.9^\circ$ ,  $28.3^\circ$ ,  $30.2^\circ$ ,  $39.5^\circ$ ,  $47.6^\circ$ ,  $51.0^\circ$  and  $56.2^\circ$  matched well with wurtzite CZTS. In addition, the minor peaks at  $34.2^\circ$  and  $37.8^\circ$  corresponding to  $\text{Cu}_7\text{S}_4$  could also be

observed. When the reaction time further increases to 120 min, the XRD pattern appears very similar to that of 60 min with both wurtzite CZTS and  $\text{Cu}_7\text{S}_4$  as well. Contrary to the synthesis of kesterite CZTS nanoparticles when at 10 min, the nanoparticles are already formed, using DDT, a slow and gradual phase evolution process is observed for wurtzite CZTS nanoparticles. The binary  $\text{Cu}_7\text{S}_4$  phase was formed at the initial stage of the reaction. And it was then consumed to give rise to wurtzite CZTS phase with the increase of reaction time as shown from the XRD results. The formation of intermediate  $\text{Cu}_7\text{S}_4$  phase and gradual development into wurtzite phase indicate that using DDT as the sulfur source will result in slower reaction rate resulting in a better controlled nanoparticles.

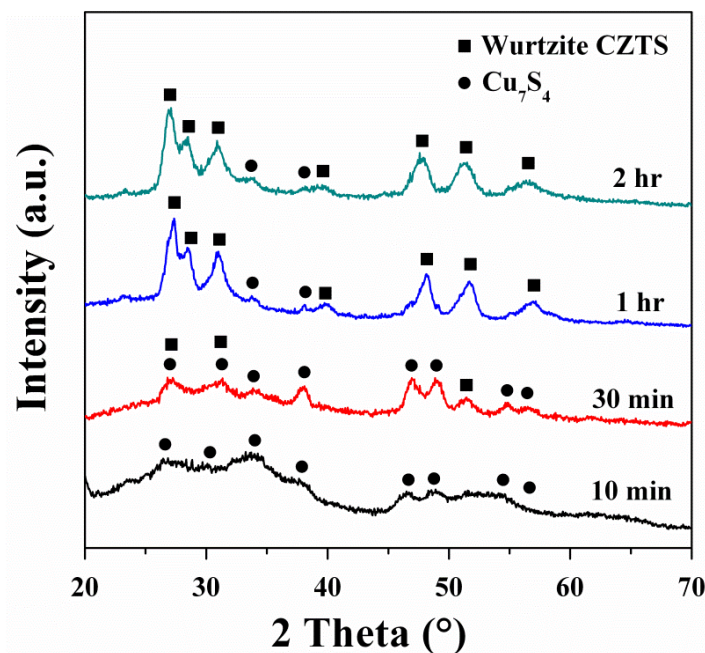


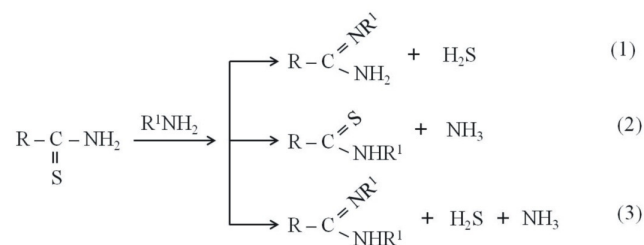
**Figure 4.7:** The XRD patterns of sample DDT at reaction timing of 10 min, 30 min, 1 hour and 2 hours.

The growth mechanisms of kesterite and wurtzite phases are proposed based on the reactivity of sulfur precursors. It is clear that based on the results of the time-dependent

studies, the elemental S and DDT as sulfur source exhibit different reactivity. The highly reactive elemental S yields a fast formation of kesterite CZTS phase, while DDT results in a slow and gradual formation of wurtzite CZTS phase starting with the formation of  $\text{Cu}_7\text{S}_4$ . In an earlier work<sup>25</sup>, it was found that sulfur and amine group could react and form alkylammonium polysulfides at room temperature. At elevated temperature, the polysulfide ions can easily react with excess amine to release  $\text{H}_2\text{S}$ . After the injection, the temperature of OLA-S mixture was increased very quickly from room temperature to above 200 °C, resulting in the formation of  $\text{H}_2\text{S}$  in the reaction mixture indicated by the bubbling in the reaction solution. The color of solution mixture turned dark immediately, indicating the fast formation of kesterite CZTS. The formation of kesterite CZTS can be considered as the rapid precipitation between  $\text{H}_2\text{S}$  with adjacent Cu, Zn and Sn species. Although the reaction rates of Cu, Zn and Sn species may vary, no noticeable binary or ternary sulfides compound could be observed from XRD. As the reaction is very rapid, it is difficult to separate the nucleation and growth processes, which resulted in a wide size distribution.

The DDT molecule contains a twelve carbon chain with a thiol head group. The thiol is the S source in this reaction for the formation of CZTS nanoparticles. S is covalent bonded to one C and one H at each side, making it a rather stable as compared to small molecule,  $\text{H}_2\text{S}$ . After the injection of OLA-DDT mixture, the reaction mixture turned gradually from yellow to black in about ten minutes. This is indicative of a slower reaction rate for DDT compared to elemental S. This is because energy is required to break the C-S-H covalent bonds to release S. When the reaction rate of sulfur precursor is limited, it will selectively react with the most reactive species among Cu-, Zn- and Sn-

precursors. As shown in the XRD patterns in Figure 4.7, the  $\text{Cu}_7\text{S}_4$  phase was first formed in this reaction. Subsequently, Zn species, Sn species and the remaining DDT reacted with  $\text{Cu}_7\text{S}_4$  seed. Due to the  $\text{Cu}_7\text{S}_4$  seed, the CZTS nanoparticles gradually evolved into the wurtzite phase. These results are in good agreement with previous the reports on wurtzite CZTS with DDT as sulfur source.<sup>17</sup> With the low reaction rate of DDT, the growth process is controlled by the bond breaking to release S, therefore a near mono-dispersed size distribution was obtained. As for the case of TAA, it was reported that TAA could react with OLA to produce  $\text{H}_2\text{S}$  and long chain N-substituted thioamides.<sup>26</sup> As shown in the following reactions, reaction 1 and 3 produce  $\text{H}_2\text{S}$ , while reaction 2 forms N-substituted thioamides. In our case, TAA react with OLA to form a mixture of  $\text{H}_2\text{S}$  and long chain N-substituted thioamides. The highly reactive  $\text{H}_2\text{S}$  leads to the production of kesterite phases while the poorly reactive long chain thioamides yields the formation of wurtzite phase. Therefore, a mixture of kesterite phase and wurtzite phase was obtained.



### 4.3.3 Effects of crystal structures on optical and electrical properties

Figure 4.8 shows the absorbance data of the CZTS sample S, sample DDT and sample TAA. The absorbance of sample S and sample TAA increases with the decrease of wavelength all the way to UV region, and it is in good agreement with most of optical

properties reported for CZTS so far.<sup>10, 13</sup> It is noticed that the absorbance of sample DDT shows a different behavior, where the absorbance drop with the decrease of wavelength until around 680 nm and then rise again in the UV regime. Lu et al. observed similar absorbance data using DDT as sulfur source. It was reported that  $\text{Cu}_x\text{S}$  has a characteristic broad absorption in the near infra-red region.<sup>27-29</sup> Therefore, the reason for the different absorption behavior of sample DDT compared with sample S and TAA could arise from the presence of  $\text{Cu}_7\text{S}_4$ . Inset of Figure 5 shows the  $(\alpha h\nu)^2$  vs.  $h\nu$  plot. The band gaps are estimated to be 1.48 eV and 1.55 eV for sample S and sample TAA respectively. However, due to the interference of  $\text{Cu}_7\text{S}_4$  phase, the band gap of sample DDT could not be estimated accurately using the  $(\alpha h\nu)^2$  vs  $h\nu$  plot. The optical band gaps sample S and sample TAA estimated based on UV-vis-NIR measurements agree well with previous reported band gap range of 1.4 ~ 1.6 eV for CZTS.<sup>30</sup>

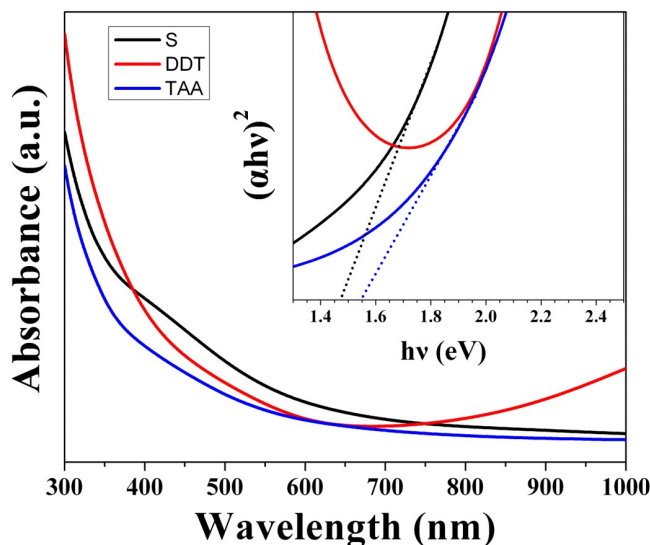


**Figure 4.8:** The UV-vis-NIR absorbance of sample S, sample DDT and sample TAA. Inset: the  $(\alpha h\nu)^2$  vs.  $h\nu$  plot for the three samples and the dotted tangent lines were drawn to assist estimating the band gap.

To investigate the conduction band (CB) and valence band (VB) energy levels of kesterite and wurtzite CZTS samples, cyclic voltammetry (CV) analysis was performed on sample S, sample DDT and sample TAA. As far as we know, this is the first time the energy levels of CZTS are determined using CV method. This is the first time energy levels of wurtzite CZTS are reported. Ferrocene was used as the reference material for all CV measurements. Figure 4.9 shows the CV measurement of ferrocene. The oxidation potential onset of ferrocene as marked by the vertical dotted line is estimated to be 0.3V. With the ferrocene as the reference material, the CB and VB energy levels of the inorganic semiconductors can be calculated using the following equation <sup>31</sup>:

$$E_{CB/VB} = [(E_{red/ox} - E_{Ferrocene}) + 4.7] \text{ eV}$$

where  $E_{Ferrocene} = 0.3 \text{ V}$ .

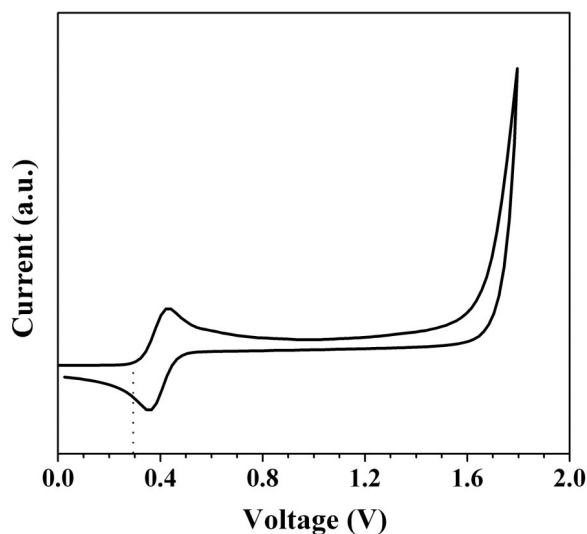


**Figure 4.9.** The cyclic voltammograms of the oxidation potential of Ferrocene as the internal standard in order to calibrate the measurements. From the oxidation scan the onset of the curve shows the oxidation potential of ferrocene to be 0.3V.

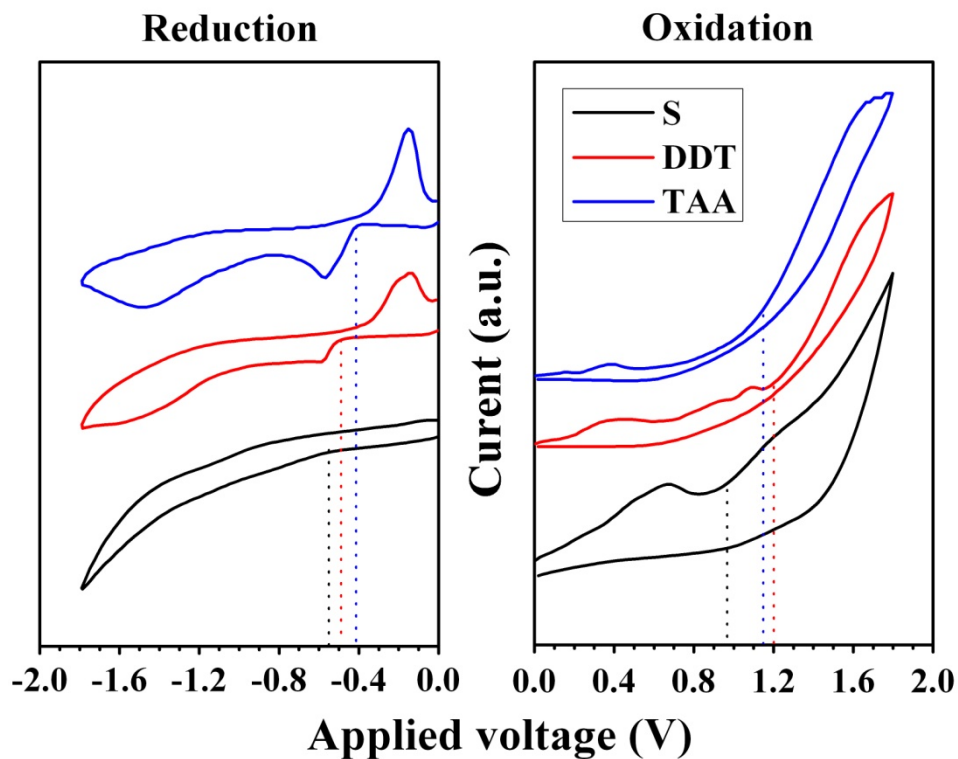


**Figure 4.10.** Cyclic voltammetry of CZTS nanoparticles samples prepared with elemental S, DDT and TAA.

**Table 4. 1** A comparison of CB and VB energy levels as well as the electrochemical band gap of sample S, sample DDT and sample TAA.

CZTS samples	$E_{\text{red}}$ (V)	$E_{\text{ox}}$ (V)	$E_{\text{CB}}$ (eV)	$E_{\text{VB}}$ (eV)	Electrochemical Band gap (eV)
sample S	-0.55	0.97	-3.85	-5.37	1.52
sample DDT	-0.49	1.20	-3.91	-5.60	1.69
sample TAA	-0.41	1.15	-3.99	-5.55	1.56

In an earlier work, Huang et al. determined the CZTS kesterite valence band energy of 5.19 eV and conduction band energy of 3.79 eV using Mott-Schottky plot.<sup>32</sup> With Ultraviolet photoelectron spectroscopy (UPS), Haight et al. estimated the two values to



be 5.4 eV and 3.95 eV.<sup>33</sup> As shown in Table 4.1, the valance band and conduction band energy levels are -5.37 and -3.85 eV (sample S), -5.60 and -3.91 eV (sample DDT), -5.55 and -3.99 eV (sample TAA). The VB and CB energy levels of CZTS kesterite (sample S) are in good agreement well with previously reported values. The difference observed for VB/CB compared to the reported data might arise from the difference in size, composition and characterization method. The VB/CB energy levels of CZTS wurtzite (sample DDT) is very similar to that for kesterite CZTS. Both the VB energy and the CB energy shifted slightly to a lower value. The kesterite-wurtzite mixture also has similar VB/CB energy levels compared with individual kesterite and wurtzite samples. The electrical band gap are determined to be 1.52 eV, 1.69 eV and 1.56 eV for sample S, sample DDT and sample TAA respectively. All the three values matched well with the reported band gap range of 1.4 ~ 1.6 eV for CZTS. In the mean time, they vary slightly with the optical band gap determined by UV-vis-NIR absorption measurements. The slight discrepancies between electrical band gap and optical band gap could possibly arise from the interfacial energy barrier between CZTS samples with the electrode. Therefore, higher band gap values for CV measurements than optical measurements are expected.

### 4.4 Conclusions

In conclusion, we have successfully synthesized kesterite, wurtzite and mixed kesterite-wurtzite CZTS nanoparticles using elemental S, DDT and TAA as the sulfur source respectively. The XRD spectra matched well with the database. The Raman peaks of sample S and sample TAA are in good agreements with reported value of CZTS. Both elemental S and TAA produce irregular shaped nanoparticles with wide size distribution.

On the other hand, DDT yields nearly spherical mono-dispersed nanoparticles. The d-spacings of each sample are also consistent with the reported values. To understand to growth mechanisms of kesterite and wurtzite phases, the time-dependant studies were performed for sample S and sample DDT. The elemental S could react with oleylamine to produce highly reactive small molecule  $H_2S$ , which then reacts with Cu, Zn and Sn species to form kesterite CZTS nanoparticles. As for the case of DDT, the covalent bonded S is very stable and hence difficult to be broken down to release the S atom for the reaction, resulting in a slow reaction rate when DDT is used as the sulfur source. Therefore, the supply of S is limited and the DDT selectively reacts with relative more reactive Cu species to form  $Cu_7S_4$  seed. Subsequent reaction grows from  $Cu_7S_4$  seed to form wurtzite phase. TAA react with OLA to produce highly reactive  $H_2S$  and less reactive long chain N-substituted thioamides, therefore results in formation of mixed kesterite and wurtzite phases.

The optical band gap was estimated to be 1.48 eV and 1.55 eV for sample S and sample TAA respectively based on UV-vis-NIR measurements. The band gap of sample DDT was not able to be estimated accurately due to the interference of  $Cu_7S_4$  phase that co-existed with wurtzite CZTS as an impurity phase. The valance band and conduction band energy levels are determined using CV measurements to be -5.37 and -3.85 eV (sample S), -5.60 and -3.91 eV (sample DDT), -5.55 and -3.99 eV (sample TAA). The electrochemical band gaps were found to be 1.52 eV, 1.69 eV and 1.56 eV respectively.

### References

1. Xu, L.-C.; Wang, R.-Z.; Liu, L.-M.; Chen, Y.-P.; Wei, X.-L.; Yan, H.; Lau, W.-M., Wurtzite-type CuInSe<sub>2</sub> for high-performance solar cell absorber: ab initio exploration of the new phase structure. *Journal of Materials Chemistry* **2012**, 22, (40), 21662-21666.
2. Walsh, A.; Chen, S.; Wei, S.-H.; Gong, X.-G., Kesterite Thin-Film Solar Cells: Advances in Materials Modelling of Cu<sub>2</sub>ZnSnS<sub>4</sub>. *Advanced Energy Materials* 2, (4), 400-409.
3. Goodman, C. H. L., The prediction of semiconducting properties in inorganic compounds. *Journal of Physics and Chemistry of Solids* **1958**, 6, (4), 305-314.
4. Pamplin, B. R., A systematic method of deriving new semiconducting compounds by structural analogy. *Journal of Physics and Chemistry of Solids* **1964**, 25, (7), 675-684.
5. Shannon, R., Revised effective ionic radii and systematic studies of interatomic distances in halides and chalcogenides. *Acta Crystallographica Section A* **1976**, 32, (5), 751-767.
6. Yeh, C. Y.; Lu, Z. W.; Froyen, S.; Zunger, A., Zinc-blende-wurtzite polytypism in semiconductors. *Physical Review B* **1992**, 46, (16), 10086-10097.
7. Yu, J. H.; Joo, J.; Park, H. M.; Baik, S. I.; Kim, Y. W.; Kim, S. C.; Hyeon, T., Synthesis of quantum-sized cubic ZnS nanorods by the oriented attachment mechanism. *Journal of the American Chemical Society* **2005**, 127, (15), 5662-5670.
8. Wang, Z. W.; Daemen, L. L.; Zhao, Y. S.; Zha, C. S.; Downs, R. T.; Wang, X. D.; Wang, Z. L.; Hemley, R. J., Morphology-tuned wurtzite-type ZnS nanobelts. *Nature Materials* **2005**, 4, (12), 922-927.
9. Hall, S. R.; Szymanski, J. T.; Stewart, J. M., Kesterite Cu<sub>2</sub>(Zn,Fe)SnS<sub>4</sub> and stannite Cu<sub>2</sub>(Fe,Zn)SnS<sub>4</sub> structurally similar but distinct minerals. *The Canadian Mineralogist* **1978**, 16, (2), 131-137.
10. Steinhagen, C.; Panthani, M. G.; Akhavan, V.; Goodfellow, B.; Koo, B.; Korgel, B. A., Synthesis of Cu<sub>2</sub>ZnSnS<sub>4</sub> Nanocrystals for Use in Low-Cost Photovoltaics. *Journal of the American Chemical Society* **2009**, 131, (35), 12554-+.
11. Lu, X.; Zhuang, Z.; Peng, Q.; Li, Y., Wurtzite Cu<sub>2</sub>ZnSnS<sub>4</sub> nanocrystals: a novel quaternary semiconductor. *Chemical Communications* **2011**, 47, (11), 3141-3143.
12. Chen, S.; Walsh, A.; Luo, Y.; Yang, J.-H.; Gong, X. G.; Wei, S.-H., Wurtzite-derived polytypes of kesterite and stannite quaternary chalcogenide semiconductors. *Physical Review B* **2010**, 82, (19), 195203.

13. Riha, S. C.; Parkinson, B. A.; Prieto, A. L., Solution-based synthesis and characterization of  $\text{Cu}_2\text{ZnSnS}_4$  nanocrystals. *Journal of the American Chemical Society* **2009**, 131, (34), 12054-+.
14. Chen, S. Y.; Gong, X. G.; Walsh, A.; Wei, S. H., Crystal and electronic band structure of  $\text{Cu}_2\text{ZnSnX}_4$  (X=S and Se) photovoltaic absorbers: First-principles insights. *Applied Physics Letters* **2009**, 94, (4), 3.
15. Guo, Q. J.; Hillhouse, H. W.; Agrawal, R., Synthesis of  $\text{Cu}_2\text{ZnSnS}_4$  nanocrystal ink and its use for solar cells. *Journal of the American Chemical Society* **2009**, 131, (33), 11672-+.
16. Singh, A.; Geaney, H.; Laffir, F.; Ryan, K. M., Colloidal synthesis of wurtzite  $\text{Cu}_2\text{ZnSnS}_4$  nanorods and their perpendicular assembly. *Journal of the American Chemical Society* **2012**, 134, (6), 2910-2913.
17. Regulacio, M. D.; Ye, C.; Lim, S. H.; Bosman, M.; Ye, E.; Chen, S.; Xu, Q.-H.; Han, M.-Y., Colloidal nanocrystals of wurtzite-type  $\text{Cu}_2\text{ZnSnS}_4$ : facile noninjection synthesis and formation mechanism. *Chemistry – A European Journal* **2012**, 18, (11), 3127-3131.
18. Paier, J.; Asahi, R.; Nagoya, A.; Kresse, G.,  $\text{Cu}_2\text{ZnSnS}_4$  as a potential photovoltaic material: A hybrid Hartree-Fock density functional theory study. *Physical Review B* **2009**, 79, (11), 115126.
19. Todorov, T. K.; Reuter, K. B.; Mitzi, D. B., High-efficiency solar cell with earth-abundant liquid-processed absorber. *Advanced Materials* **2010**, 22, (20), E156-+.
20. Todorov, T. K.; Tang, J.; Bag, S.; Gunawan, O.; Gokmen, T.; Zhu, Y.; Mitzi, D. B., Beyond 11% efficiency: characteristics of state-of-the-art  $\text{Cu}_2\text{ZnSn(S,Se)}_4$  solar cells. *Advanced Energy Materials* **2012**, 3, (1), 34-38.
21. Guo, Q.; Ford, G. M.; Yang, W. C.; Walker, B. C.; Stach, E. A.; Hillhouse, H. W.; Agrawal, R., Fabrication of 7.2% efficient CZTSSe solar cells using CZTS nanocrystals. *Journal of the American Chemical Society* **2010**, 132, (49), 17384-17386.
22. Scragg, J. J.; Berg, D. M.; Dale, P. J., A 3.2% efficient Kesterite device from electrodeposited stacked elemental layers. *Journal of Electroanalytical Chemistry* **2010**, 646, (1-2), 52-59.
23. Cheng, A. J.; Manno, M.; Khare, A.; Leighton, C.; Campbell, S. A.; Aydil, E. S., Imaging and phase identification of  $\text{Cu}_2\text{ZnSnS}_4$  thin films using confocal Raman spectroscopy. *Journal of Vacuum Science & Technology A: Vacuum, Surfaces, and Films* **2011**, 29, (5), 051203.
24. Fan, F.-J.; Wu, L.; Gong, M.; Chen, S. Y.; Liu, G. Y.; Yao, H.-B.; Liang, H.-W.; Wang, Y.-X.; Yu, S.-H., Linearly arranged polytypic CZTSSe nanocrystals. *Sci. Rep.* **2012**, 2.

25. Thomson, J. W.; Nagashima, K.; Macdonald, P. M.; Ozin, G. A., From sulfur-amine solutions to metal sulfide nanocrystals: peering into the oleylamine-sulfur black box. *Journal of the American Chemical Society* **2011**, 133, (13), 5036-5041.
26. Petrov K. A., Andreev, L. N., The chemical properties of thioamides. *Russian Chemical Reviews* **1971**, 40, (6).
27. Kameyama, T.; Osaki, T.; Okazaki, K.-i.; Shibayama, T.; Kudo, A.; Kuwabata, S.; Torimoto, T., Preparation and photoelectrochemical properties of densely immobilized  $\text{Cu}_2\text{ZnSnS}_4$  nanoparticle films. *Journal of Materials Chemistry* **2010**, 20, (25), 5319-5324.
28. Silvester, E. J.; Grieser, F.; Sexton, B. A.; Healy, T. W., Spectroscopic studies on copper sulfide sols. *Langmuir* **1991**, 7, (12), 2917-2922.
29. Zhao, Y.; Pan, H.; Lou, Y.; Qiu, X.; Zhu, J.; Burda, C., Plasmonic  $\text{Cu}_{2-x}\text{S}$  nanocrystals: optical and structural properties of copper-deficient copper(I) sulfides. *Journal of the American Chemical Society* **2009**, 131, (12), 4253-4261.
30. Katagiri, H.,  $\text{Cu}_2\text{ZnSnS}_4$  thin film solar cells. *Thin Solid Films* **2005**, 480, 426-432.
31. A. J. Bard, L. R. F., Electrochemical methods : fundamentals and applications. *New York: Wiley* **1980**, 1-864.
32. Huang S., L. W., Zou Z., Band positions and photoelectrochemical properties of  $\text{Cu}_2\text{ZnSnS}_4$  thin films by the ultrasonic spray pyrolysis method. *J. Phys. D: Appl. Phys* **2013**, (46).
33. Haight, R.; Barkhouse, A.; Gunawan, O.; Shin, B.; Copel, M.; Hopstaken, M.; Mitzi, D. B., Band alignment at the  $\text{Cu}_2\text{ZnSn}(\text{S}_x\text{Se}_{1-x})_4/\text{CdS}$  interface. *Applied Physics Letters* **2011**, 98, (25), 253502-3.

# Chapter 5: Synthesis of CZTS thin film using binary sulfide nanoparticles

## 5.1 Introduction

In Chapter 3 and 4, the synthesis and studies of  $\text{Cu}_2\text{ZnSnS}_4$  (CZTS) nanoparticles using hot injection method were presented. This method could also good size, shape, composition and phase control by varying synthesis parameters such as temperature, time, solvents and surfactants, Cu-, Zn-, Sn- and S-precursors. However, hot injection method has its limitations in practical applications. Firstly, the use of organic solvents, e.g. oleylamine, is costive and not quite environmentally friendly. Secondly, the synthesis of CZTS nanoparticles requires harsh experimental conditions including high reaction temperature (generally above 200 °C) and inert gas protection. Last but not least, the hot injection method is not suitable for large scale production. Regarding to the above challenges, in this chapter, we develop a low-cost, environmentally friendly and easily up-scalable method to form CZTS thin film making use of aqueous solution synthesized CuS, ZnS and  $\text{SnS}_2$  nanoparticles.

Quaternary chalcogenide CZTS compound is a suitable absorber material for TFSCs mainly due to the following material properties: (i) direct band gap around 1.5 eV, (ii) good absorption coefficient of more than  $10^4 \text{ cm}^{-1}$ , and (iii) earth-abundant constituents.<sup>1,</sup>

<sup>2</sup> To date, many different routes have been developed to deposit CZTS thin film.<sup>3</sup> Vacuum-based deposition techniques have been very successful in demonstrating high efficiencies in CIGS solar cells, and therefore have been widely adopted in the deposition

of CZTS thin films.<sup>4,5</sup> Katagiri and co-workers pioneered the early studies of CZTS solar cells.<sup>1, 6, 7</sup> With radio frequency (RF) co-sputtered of elemental and binary sulfides precursors, they obtained a solar cell efficiency of 6.77%.<sup>8</sup> In another popular approach, Cu-, Zn- and Sn-metal layers are deposited by sputtering, and then the films are annealed at high-temperature in H<sub>2</sub>S environment to form CZTS.<sup>9</sup> The ratio of Cu : Zn : Sn could be tuned by changing the thickness of each metal layer. Using this method, Kobayashi et al. achieved a device efficiency of 5.45%.<sup>10</sup> More recently, Shin et al. made use of co-evaporation of elemental Cu, Zn, Sn and S followed by annealing the film resulting in a device with a high efficiency of 8.4% (device area of 0.45 cm<sup>2</sup>).<sup>11</sup> Despite the excellent progress, vacuum-based techniques still require high energy input and impose a significant cost on devices. Hence, there is a move towards finding an alternative low-cost fabrication method to the vacuum deposition techniques.

Recently, CZTS has been fabricated using low-cost solution-based methods. Scragg et al. fabricated CZTS TFSCs using electrodeposited stacked metal layers and achieved an device performance of 3.2%.<sup>12</sup> Kumar et al. synthesized CZTS thin film by spray pyrolysis technique, where the precursor solution contained Cu-, Zn-, Sn-salts and thiourea.<sup>13</sup> The CZTS nanoparticles approach and hybrid solution-particles approach have attracted more interest than other methods due to its possibility in generating solar cells with high power conversion efficiency - 7.2% for the former and beyond 11% for the latter.<sup>14, 15</sup> In CZTS nanoparticles approach, the CZTS nanocrystals were synthesized usually via hot coordinating solvent method and the nanocrystal dispersion could then be deposited on the substrate and annealed to form the absorber layer.<sup>16-18</sup> The hybrid solution-particles approach made use of slurry containing Cu-, Sn-chalcogenide solution

precursors and Zn-chalcogenide nanoparticles dispersion in hydrazine ( $\text{N}_2\text{H}_4$ ), which was then spin-coated and annealed to form CZTS layer.<sup>19</sup>

To date, it has been shown that solution processed CZTS solar cells have reasonably high conversion efficiency and hence cost wise there is a potential for this technology to compete with mature CdTe, CIGS technologies. The chemicals involved as well as the byproduct in the synthesis process have low toxicity which is an added advantage. Since CZTS can be processed in solution, the fabrication process can be easily scaled up for mass production. Of the various solution deposition methods, the electrodeposition method suffers from low conversion efficiency. For the spray pyrolysis method, the  $\text{NH}_3$  and HCl byproducts is less friendly to the environment especially in large quantity.<sup>20, 21</sup> Although the CZTS nanoparticles approach and hybrid solution-particles approach were able to demonstrate high efficiency, both methods have issues that limit large scale practical applications: (i) the use of expensive and toxic organic solvents (oleylamine, hexadecylamine for the former, and hydrazine for the latter) that may increase the fabrication cost and also lead to environmental issues; (ii) highly demanding processing conditions such as high reaction temperature and inert environment make the processes difficult to scale up. Therefore, a novel synthesis method that is cost-effective, environmentally benign and easily upscalable is highly required.

Here, we report one such method to prepare CZTS thin film. Since  $\text{Cu}_2\text{ZnSnS}_4$  is a quaternary compound, instead of ionic precursors, the starting precursors to the film can also be a combination of  $\text{Cu}_2\text{S}$ ,  $\text{ZnS}$  and  $\text{SnS}_2$  binary sulfides in 1:1:1 ratio, and the transformation to quaternary films from these binary precursors will not change the



valence state of any element. Inspired by this idea, CZTS thin film is synthesized using the respective Cu-, Zn- and Sn- binary sulfides nanoparticles. These binary sulfides nanoparticles can be easily synthesized in an aqueous environment. This method allows the use of most common Cu-, Zn- and Sn-precursors including chlorides, sulfates, nitrates and acetates, while the sulfur source is from hydrated sodium sulfide ( $\text{Na}_2\text{S} \cdot 9\text{H}_2\text{O}$ ). The deposition techniques could be spray coating, printing, spin-coating, and many other solution deposition techniques. This route could allow easy tuning of the composition of the films and the possibility preparing stable inks for printing, and hence pave the way for large scale and environmentally friendly way to fabricate TFSCs.

## 5.2 Experimental Procedures

### *Chemicals*

Copper (II) acetate ( $\text{Cu}(\text{OAc})_2$ , Aldrich, 98%), zinc acetate ( $\text{Zn}(\text{OAc})_2$ , Aldrich, 99.99%), tin (IV) chloride pentahydrate ( $\text{SnCl}_4 \cdot 5\text{H}_2\text{O}$ , Sigma-Aldrich, 98%), sodium sulfide nonahydrate ( $\text{Na}_2\text{S} \cdot 9\text{H}_2\text{O}$ , Aldrich, 98%), (n-hexadecyl) trimethyl ammonium bromide (CTAB, Lancaster, 98%) and ethanol (Aik Moh Paints & Chemicals, 95%) were purchased and used as received. Milli-Q water (Millipore,  $18.5 \text{ M}\Omega\text{cm}$  at  $25^\circ\text{C}$ ) was used in all synthesis and centrifugation processes.

### *Experiment*

The preparation of CZTS film consists of four consecutive steps as shown in Figure 5.1:

(i) synthesis of CuS, ZnS and  $\text{SnS}_2$  nanoparticles, (ii) mix the sulfides nanoparticles in desired molar ratio in proper solvent (water, ethanol, etc) to form the precursor solution, (iii) deposit precursor solution onto substrates to form precursor films and (iv) anneal

precursor films to form CZTS films. The CuS, ZnS and SnS<sub>2</sub> nanoparticles were synthesized using precipitate reactions between S<sup>2-</sup> anions and Cu<sup>2+</sup>, Zn<sup>2+</sup>, Sn<sup>4+</sup> cations in aqueous solution. Cetyl trimethylammonium bromide (CTAB) was used as the capping ligand for all three types of nanoparticles. Table 5.1 shows the experimental details for the synthesis of CuS, ZnS and SnS<sub>2</sub> nanoparticles. During the experiment, freshly prepared sulfur precursor solution was added into respective cations precursor solution drop by drop under constant stirring at room temperature (25 °C). The solution was allowed to react a period of time as mentioned in Table 5.1. After the synthesis, CuS, ZnS and SnS<sub>2</sub> binary nanoparticles were rinsed three times using water and ethanol to remove excess ligands and any unreacted precursors.

**Table 5.1** Synthesis details for CuS, ZnS and SnS<sub>2</sub> nanoparticles

Binary Sulfides	Cation Precursors	Sulfur Precursor	Reaction Time
<b>CuS</b>	1.2 mmol Cu(OAc) <sub>2</sub> , 100 ml H <sub>2</sub> O	2.4 mmol Na <sub>2</sub> S.9H <sub>2</sub> O, 0.6 mmol CTAB, 15 ml H <sub>2</sub> O	3 h
<b>ZnS</b>	1.2 mmol Zn(OAc) <sub>2</sub> , 100 ml H <sub>2</sub> O		30 min
<b>SnS<sub>2</sub></b>	1.2 mmol SnCl <sub>4</sub> .5H <sub>2</sub> O, 100 ml H <sub>2</sub> O		30 min

The experimental scheme is shown in Figure 5.1. In a typical experiment, 95.6 mg CuS (1 mmol), 48.7 mg ZnS (0.5 mmol) and 91.4 mg SnS<sub>2</sub> (0.5 mmol) were weighed and added into 300 ml solvent. The solvent can be either ethanol or DI water. The solution mixture was then ultrasonicated for 30 min followed by another 30 min stirring in order to form well-dispersed precursor solution. Subsequently, the precursor solution was spray deposited onto a glass or Mo-coated glass substrates. During the spraying process, the

substrates surface temperature was maintained at 100 °C for ethanol solvent and 300 °C for DI water solvent. The precursor film can then be annealed under inert gas to form CZTS thin film. In this work, the annealing temperatures at 200 °C, 300 °C, 400 °C and 450 °C were studied, and the annealing time was kept at 30 min for all temperatures. The precursor film could also go through a “selenization” process, or annealing under selenium vapor, to form  $\text{Cu}_2\text{ZnSn}(\text{S}, \text{Se})_4$  (CZTSSe) film. The selenization process was performed at 520 °C for 12 min with 30mg of Se pellet.

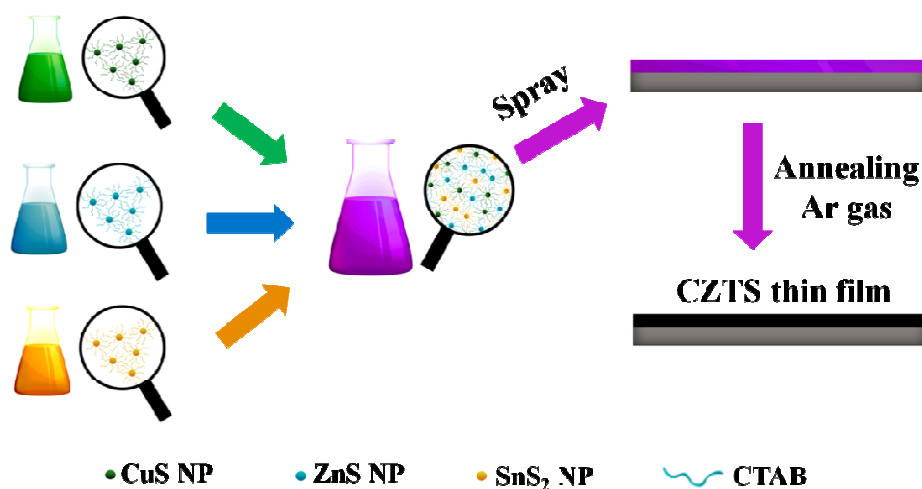


**Figure 5.1.** The scheme of the preparations of CZTS thin film using CuS, ZnS and SnS<sub>2</sub> nanoparticles.

### *Characterizations*

The Grazing Incidence X-ray diffraction (GIXRD) patterns were collected using Bruker D8 Advance equipped with Cu K $\alpha$  radiation ( $\lambda = 1.54 \text{ \AA}$ ). The diffraction was taken at a fixed incident angle of 1°, and collected from 10° to 80° in steps of 0.05°. Rietveld refinement was performed using TOPAS V3 software with fundamental parameter peak profile for CZTS sample. A five-coefficient Chebychev polynomial and 1/x background,

a zero error, scale factor, lattice parameters and crystal size were successively refined. SEM images were acquired on a JEOL JSM 7600F FESEM at an accelerating voltage of 5 kV. The FESEM is equipped with an Oxford X-MAX energy dispersive X-ray spectroscopy (EDS) detector, which was used to estimate the atomic ratio of CZTS thin film. The film was deposited on Si substrate to reduce the sample charging during imaging and EDX measurement. The TEM analysis was performed using JEOL JSM – 2100F equipped with EDAX EDS detector. The voltage used for imaging and elemental mapping was 200 kV. The UV-Vis-NIR absorption spectra were measured using a Shimadzu UV-Vis-NIR PerkinElmerLambda 900 spectrophotometer.

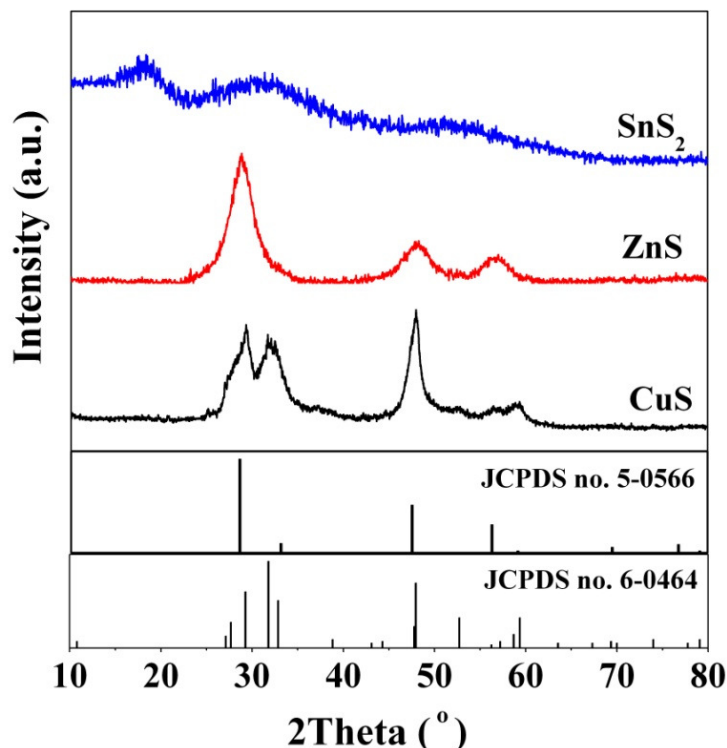
### 5.3 Results and Discussion

This section will present the synthesis and characterization of the CZTS thin films prepared using binary sulfides nanoparticles. The phase evolution processes from binary sulfides to quaternary CZTS films will also be discussed. Near stoichiometric and Zn-rich compositions films are demonstrated to show the feasibility of composition control with our approach. In addition, the annealed CZTS film and selenized CZTS<sub>Se</sub> film will be compared and evaluated for their use in solar cells. Lastly, the device performance of CZTS TFSCs is also presented and discussed.

#### 5.3.1. Binary sulfide nanoparticles

The synthesized CuS, ZnS and SnS<sub>2</sub> nanoparticles were washed thoroughly using water and ethanol for three times to remove unreacted precursors, by products and excess ligand. The as-prepared CuS, ZnS and SnS<sub>2</sub> nanoparticles can be re-dispersed in both water and ethanol. In the section 5.3.1 and 5.3.2, ethanol solvent was used to prepare

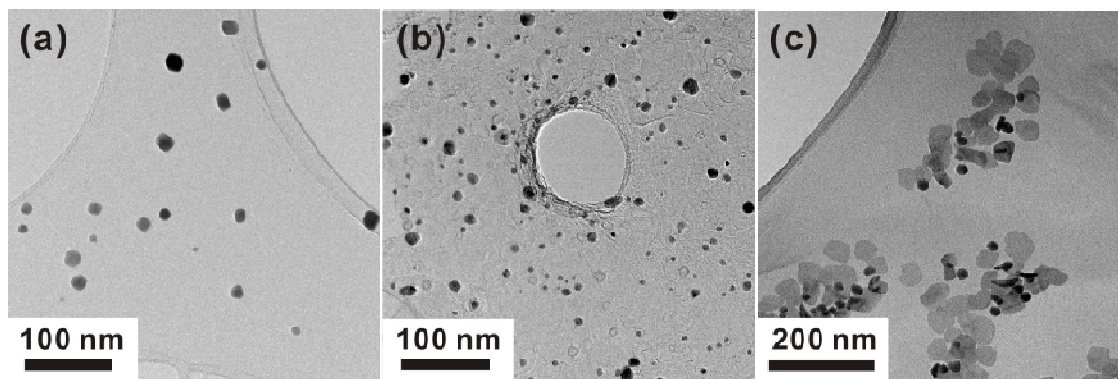
CZTS film mainly because ethanol has a lower boiling temperature than water. This allows low substrate temperature ( $\sim 100\text{ }^{\circ}\text{C}$ ) during spray deposition. The low substrate temperature could help to minimize the oxidation issue during spray.



**Figure 5.2.** The XRD patterns of as-synthesized CuS, ZnS and SnS<sub>2</sub> nanoparticles. The diffraction peaks for CuS (JCPDS no. 6-0464) and ZnS (JCPDS no. 5-0566) from the database are also shown as comparison. The XRD samples were prepared by spraying the respective nanoparticles suspension in ethanol onto glass substrates.

Figure 5.2 presents the XRD patterns of as-synthesized CuS, ZnS and SnS<sub>2</sub> nanoparticles. It is found that the XRD patterns of CuS and ZnS match well with CuS (JCPDS no. 6-0464) and ZnS (JCPDS no. 5-0566), which are also shown in the same figure. For SnS<sub>2</sub> nanoparticles, instead of distinct peaks, three major humps at  $2\theta$  around  $18^{\circ}$ ,  $30^{\circ}$  and  $50^{\circ}$  were observed. The synthesis of SnS<sub>2</sub> nanoparticles was carried out using  $\text{Sn}^{4+}$  and  $\text{S}^{2-}$  and this has been reported previously and showed low crystallinity.<sup>22</sup> The lack of distinct

peaks in the XRD pattern may be assigned to the high amorphous content in this sample. The EDS analysis showed that the Sn to S ratio is 1:1.80, which is close to stoichiometry of 1:2 for  $\text{SnS}_2$ . The EDS data for  $\text{SnS}_2$  sample can be found in Appendix A.



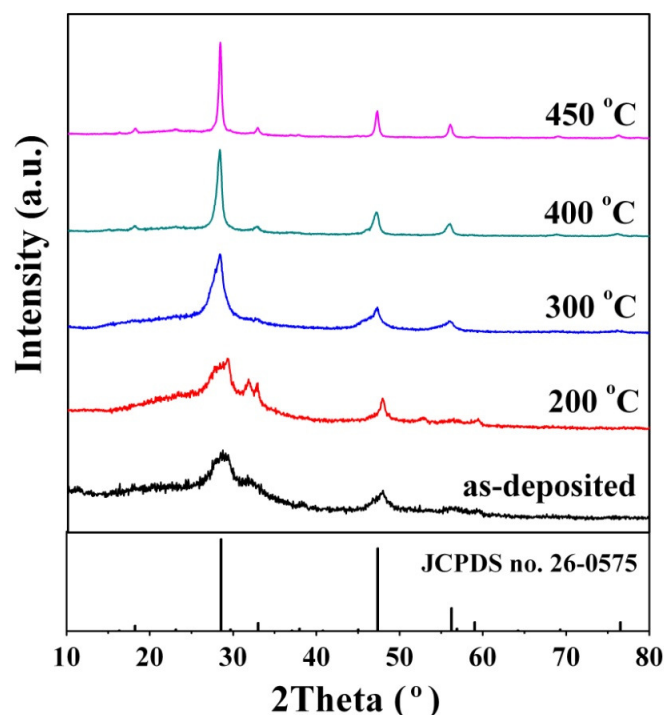
**Figure 5.3.** The TEM images of as-synthesized (a) CuS, (b) ZnS and (c)  $\text{SnS}_2$  nanoparticles.

Figure 5.3a-c shows the TEM images of the as-prepared CuS, ZnS and  $\text{SnS}_2$  nanoparticles respectively. The size of all three types of nanoparticles is found to be in the order of tens of nanometers. These small particles have much larger surface energy compared to micron sized particles, hence there is a stronger driving force for coalescence to happen as this will reduce the surface energy. On top of this, as compared to micron sized particles or even larger particles, during annealing, the atoms in the particles only need to diffuse to a short distance to their nearest neighbours for coalescence to occur because they are packed closer. Therefore, on top of higher driving force for coalescence to occur due to high surface energy, the nanometer dimension would also mean shorter diffusion distances for Cu, Zn, Sn and S atoms during the formation of CZTS film as compared to larger particles. It is also noticed that all the three types of nanoparticles could be dispersed quite well with no obvious aggregation up to

three hours. Any localized agglomeration of the same species may lead to the non-uniformity in the composition in the final CZTS thin film.

### 5.3.2. Kesterite CZTS thin film using binary nanoparticles

The precursor film, which was made up of a mixture of CuS, ZnS and SnS<sub>2</sub> nanoparticles in a molar ratio of 2 : 1 : 1, was annealed at different temperatures - 200, 300, 400 and 450 °C for 30 min under Ar gas environment. As shown in Figure 5.4, the XRD spectrum of the as-deposited precursor film consists of overlapping XRD patterns of as-synthesized CuS, ZnS and SnS<sub>2</sub> nanoparticles. After annealing at 200 °C for 30 min, it could be noticed that the  $2\theta$  peaks at 29.3°, 31.8°, 32.9 °, 47.9°, 52.7° and 58.7° became sharper compared to the as deposited precursor film, showing increased crystallinity of CuS nanoparticles. New sharp peaks at 28.5°, 47.3° and 56.2° can be observed for samples annealed at 300, 400 and 450 °C, which correspond to (112), (220) and (312) planes of kesterite CZTS (JCPDS no. 26-0575). These are the major peaks for kesterite CZTS. In addition, all the minor peaks also matched well with kesterite CZTS and no unidentified peaks was observed. This indicates the formation of kesterite CZTS phase at these temperatures. Comparing the XRD spectra taken at various temperatures, the full width at half maximum (FWHM) for (112) peak is found to decrease as the annealing temperature increases from 300 to 450 °C, which indicates that the CZTS grain size in the annealed film increased with temperature.



**Figure 5.4.** The XRD spectra for the as-prepared precursor film and the films that were annealed at 200, 300, 400 and 450 °C. The reference diffraction peaks for kesterite CZTS (JCPDS no. 26-0575) is also displayed at bottom.

The XRD results for precursors annealed at 300, 400 and 450 °C provide the evidence for formation of kesterite CZTS phase at these temperatures. Unfortunately, some binary and ternary phases such as  $\text{Cu}_2\text{S}$  (JCPDS 4-15-2234),  $\text{ZnS}$  (JCPDS 5-0566) and  $\text{Cu}_2\text{SnS}_3$  (JCPDS 1-089-4714) share similar crystal structure as well as XRD patterns with CZTS. This makes it difficult to conclusively deduce if the film contains impurity phases at these temperatures using only the XRD data. Raman spectroscopy is a well established technique to identify impurity phases in CZTS film.<sup>23</sup> The Raman peaks for CZTS (288, 338 and 368  $\text{cm}^{-1}$ ),  $\text{Cu}_2\text{S}$  (475  $\text{cm}^{-1}$ ),  $\text{ZnS}$  (278 and 351  $\text{cm}^{-1}$ ) and  $\text{Cu}_2\text{SnS}_3$  (298 and 356  $\text{cm}^{-1}$ ) are distinct.<sup>24-27</sup> Hence, in order to check whether the CZTS film contains secondary phases, Raman analysis was performed. As shown in Figure 5.5, the samples



annealed at all three temperatures exhibit strong peak at around  $336\text{ cm}^{-1}$  with two weak shoulder peaks at  $288$  and  $368\text{ cm}^{-1}$ . The above three peaks are indicative of the presence of CZTS phase in the films annealed at  $300$ ,  $400$  and  $450\text{ }^{\circ}\text{C}$ . In addition, no noticeable peaks corresponding to  $\text{Cu}_2\text{S}$  ( $475\text{ cm}^{-1}$ ), as well as  $\text{ZnS}$  ( $278$  and  $351\text{ cm}^{-1}$ ) and  $\text{Cu}_2\text{SnS}_3$  ( $298$  and  $356\text{ cm}^{-1}$ ) can be observed, which exclude the existence of all the three possible impurity phases. Therefore, from Raman analysis together with the XRD data, it can be concluded that pure CZTS films were formed at  $300$ ,  $400$  and  $450\text{ }^{\circ}\text{C}$ .

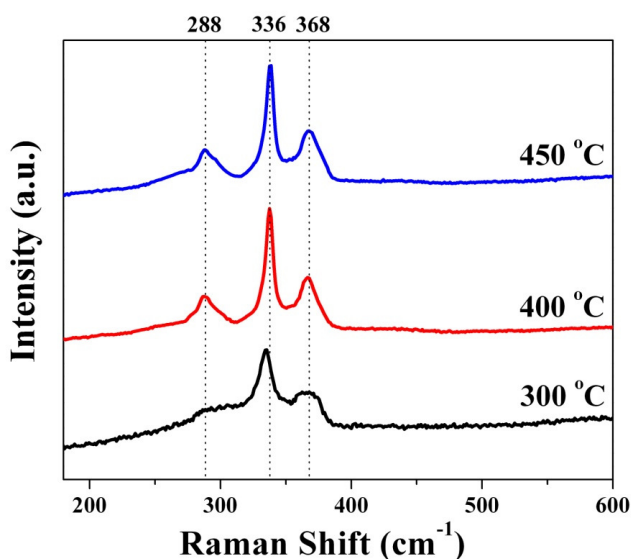


**Figure 5.5.** The Raman analysis of the films annealed at  $300$ ,  $400$  and  $450\text{ }^{\circ}\text{C}$ . The peak position of  $288$ ,  $336$  and  $368\text{ cm}^{-1}$  are marked with vertical dotted lines.

The top view of SEM image for CZTS thin film prepared at  $400\text{ }^{\circ}\text{C}$  is shown in Figure 5.6a. The film is dense and the average grain size is observed to be about  $100\text{ nm}$ . The cross-section view of SEM image in Figure 5.6b shows that the thickness of CZTS thin film is around  $1\text{ }\mu\text{m}$ . There are some small voids within the film that could also be observed. The HRTEM image of the CZTS grain is shown in Figure 5.6c and the

interplanar spacings were determined to be 0.31 nm and 0.27 nm. These two spacings correspond to the d-spacing for (112) planes and (020) planes respectively for kesterite CZTS.<sup>17</sup> Figure 5.6d shows the select area electron diffraction (SAED) pattern and two primary diffraction spots were marked indicating the diffraction corresponding to the reciprocal lattices of CZTS. The SAED was performed with zone axis along [201].

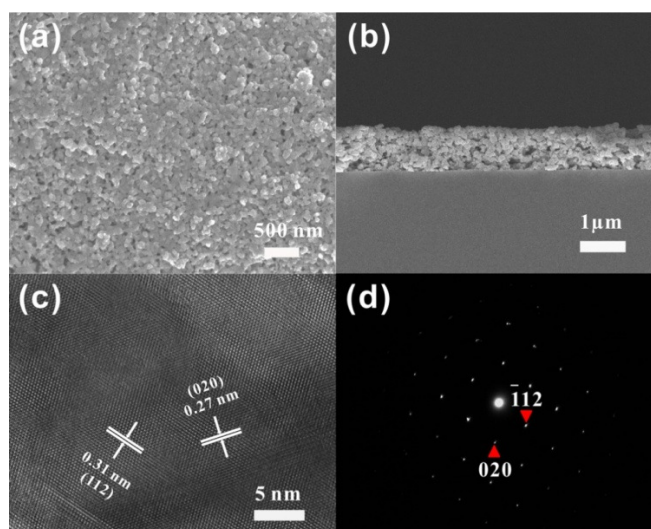


**Figure 5.6.** Electron micrographs of sample annealed at 400 °C. (a) Top view SEM image of CZTS thin film and (b) cross-sectional view of SEM image. (c) HRTEM image and (d) SAED pattern.

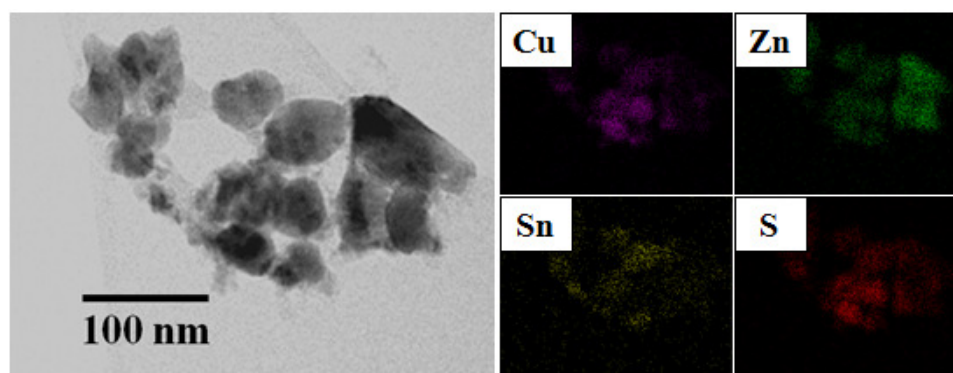
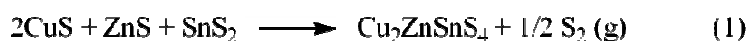


**Figure 5.7.** STEM-EDS elemental mapping of the particles obtained from as prepared CZTS film. The distributions of Cu, Zn, Sn and S are presented.

In order to investigate the distribution of Cu, Zn, Sn and S elements of the as-prepared CZTS thin film samples, the elemental maps of the annealed particles were collected using the STEM-EDS. The TEM sample was prepared by re-dispersing CZTS nanocrystals film into ethanol and drop-casting the solution onto holey carbon-coated Ni-grid. As shown in Figure 5.7, it was found that all the four elements (Cu, Zn, Sn and S) were distributed relatively uniformly in the nanocrystals investigated. This could also serve as another evidence for the formation of CZTS phase instead of ZnS and Cu<sub>2</sub>SnS<sub>3</sub> phases and this is in agreement with the Raman results presented previously.



The composition of precursor films and CZTS thin films was investigated using EDS. The atomic ratio of Cu: Zn: Sn: S was determined to be 1.9: 0.9: 0.9: 4.2 for precursor film. This is in agreement with the amount of initially added CuS, ZnS and SnS<sub>2</sub>. After annealing in 400 °C for 30 min, the Cu: Zn: Sn: S ratio changed to 1.9: 1.0: 0.9: 4.1, which is close to the stoichiometric ratio of 2: 1: 1: 4 with slight S-rich. The EDS data for CZTS thin film can be found in the Appendix A. The possible reason for the film to be S-rich is that the binary sulfide precursors contain excess S due to the oxidation states of Cu binary compound. In CZTS compound, Cu exists as Cu<sup>+</sup>, and thus one Cu<sup>+</sup> corresponds to half S<sup>2-</sup> to account for charge neutrality. By contrast, one Cu<sup>2+</sup> corresponds to one S<sup>2-</sup> in CuS compound. During the formation of CZTS, Cu<sup>2+</sup> will be reduced to Cu<sup>+</sup>, resulting excess S. The proposed chemical reaction is shown in Equation 1. Sulfur vapor is formed as a by-product in the reaction. Generally, CZTS films suffer from Sn and S loss during annealing.<sup>28</sup> Looking at EDX results of the annealed CZTS films, it was found that the Sn

ratio was maintained with slight S loss. This is mainly due to the relatively low annealing temperature of 400 °C.

The composition of CZTS films can be tuned by modifying the ratio of binary sulfides precursors. In addition to the stoichiometric composition, Zn-rich CZTS films with  $([Zn]/[Sn]) \sim 1.25$  and  $[Cu]/([Zn]+[Sn]) \sim 0.9$  were prepared. The reason for choosing the above ratios is that most of the highly efficient devices reported were achieved with this narrow composition range.<sup>29</sup> The optical properties of stoichiometric CZTS and Zn-rich CZTS were evaluated using UV-vis-NIR spectrophotometer with integrating sphere. The transmittance ( $T_\lambda$ ) and reflectance ( $R_\lambda$ ) measurements for each film were performed. The absorption coefficient ( $\alpha$ ) could be calculated by the following formula:

$$\alpha = \frac{1}{t} \ln \left[ \frac{(1 - R_\lambda)^2}{T_\lambda} \right]$$

where  $t$  is the film thickness.

The  $(\alpha h\nu)^2$  versus  $h\nu$  curves for stoichiometric CZTS and Zn-rich CZTS are shown in Figure 5.8, where  $h$  is the Planck constant and the frequency of light  $\nu = c/\lambda$  (where  $c$  is velocity of light.  $\lambda$  is wavelength of light). The linear region was extrapolated for each curve with a dotted line and the intercepts on  $h\nu$  axis is the optical band gaps for each material. The band gap energies were found to be 1.43 eV (stoichiometric CZTS) and 1.52 eV (Zn-rich CZTS), and they are in good agreements with reported values.<sup>1, 30</sup> This fabrication route is highly flexible in controlling the composition of CZTS film and it would be possible to prepare films with other compositions by simply modifying the molar ratio of CuS, ZnS and SnS<sub>2</sub> nanoparticles precursors. Moreover, the same synthetic

approach could also be adopted to  $\text{Cu}_2\text{ZnSnSe}_4$  (CZTSe) or even  $\text{Cu}_2\text{ZnSn}(\text{S},\text{Se})_4$  (CZTSSe) thin films by using respective binary metal sulfides/selenides compounds.

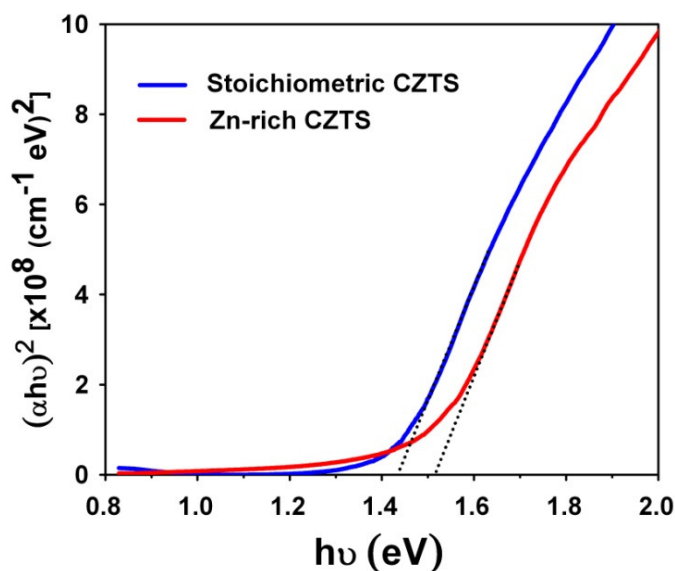


**Figure 5.8.** The  $(\alpha h\nu)^2$  versus  $h\nu$  plots for stoichiometric CZTS and Zn-rich CZTS. The interception of the dotted lines with  $h\nu$  axis determines the band gap.

### 5.3.3. Solar cells performance

Using ethanol as the solvent, pure CZTS nanoparticles film was successfully prepared. Although the low substrate temperature could prevent the oxidation of the as deposited nanoparticles, one major problem with low temperature is the limited grain growth in CZTS film. As a result, the as prepared CZTS thin films are not very compact. These voids present in the films are extremely detrimental for electron and hole transport and hence should be minimized. One way to solve this problem is to increase the substrate temperature. At higher temperatures, such as 300 °C, the nanoparticles precursor can actually fuse and grow more, which is likely to densify the film. Unfortunately, it is very difficult to spray deposit the nanoparticles with ethanol solvent at such high temperature

because it is highly flammable. Therefore, water, which is less flammable, was used as the solvent for high temperature deposition. The substrate temperature was set to be 300 °C for spraying of the solution with DI water as the solvent. In order to prevent the oxidation of binary sulfides nanoparticles, thiourea (TU) which served as sulfur precursor was added and mixed homogeneously into the CuS, ZnS and SnS<sub>2</sub> nanoparticles mixture solution. The molar ratio of [TU]/([CuS] + [ZnS] + [SnS<sub>2</sub>]) was fixed at two.

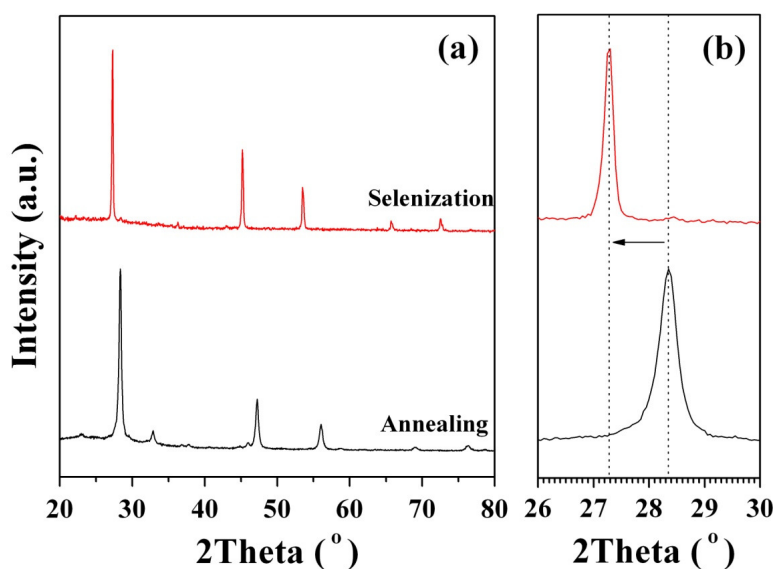


**Figure 5.9.** The XRD pattern of CZTS film prepared by annealing the precursor film and CZTSSe film prepared by selenized the precursor film: (a) full scale and (b) magnified version.

The nanoparticles precursor films were spray deposited with water as solvent and substrate temperature of 300 °C. The precursor films were then thermally annealed in Ar gas environment or in selenium vapour (selenization). The thermal annealing was carried out at 500 °C for 30 min in Ar environment, whereas the selenization was performed at 520 °C for 12 min in selenium vapour. Figure 5.9 presents the XRD patterns of the annealed film and the selenized film. The XRD of the annealed film matches well with

that for kesterite CZTS phase with characteristic  $2\theta$  angle of  $28.5^\circ$ ,  $47.3^\circ$  and  $56.2^\circ$ . The selenized film possessed similar XRD patterns to that of the annealed film. This indicates that the new CZTSSe phase retains the kesterite crystal structure. Meanwhile, it is also noticed that the XRD peaks of the selenized film shifted to lower  $2\theta$  value as compared with the annealed film. In the magnified image shown in Figure 5.9b, it was found that the major peak at  $28.5^\circ$  for CZTS shifted around  $1^\circ$  to  $27.5^\circ$  for the CZTSSe. The Se atom has larger atomic radius than S atoms. During selenization process, the S atoms are replaced by Se atoms. Due to the larger size of Se atoms than S atoms, the lattice spacings of CZTSSe lattice increase as compared with CZTS. As  $2\theta$  is inversely proportional to the lattice spacing, the diffraction peak of the selenized film shifts to lower  $2\theta$  angle as expected.

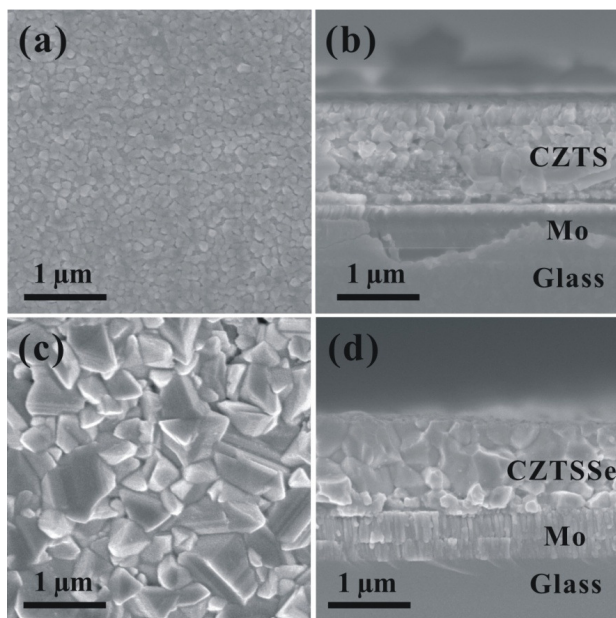


**Figure 5.10.** The SEM images of the annealed film (a) topography and (b) cross-section, and selenized film (c) topography and (d) cross-section.

Figure 5.10 shows the SEM images of the annealed film and the selenized film. As shown in Figure 5.10a and b, a compact nanocrystalline CZTS film with thickness around 1  $\mu\text{m}$  is formed after annealing. The average grain size is estimated to be around 100 nm. The selenized film shows a significant increase in grain size (Figure 5.10c and d). The grain size ranges from a few hundred nanometres up to more than one micrometre. In CZTS based TFSCs, large grain size is usually favoured due to better charge transport properties.<sup>31, 32</sup>

The solar cells were fabricated using the selenized film, or CZTSSe thin film, as the absorber due to the large grain size. The Cu-poor, Zn-rich film composition was used with  $\text{Cu}/(\text{Zn} + \text{Sn}) = 0.72$  and  $\text{Zn}/\text{Sn} = 1.2$ . The  $\text{Se}/(\text{S} + \text{Se})$  ratio determined by EDX was found to be approximately 0.8. The photovoltaic devices were fabricated using the following standard procedures – CZTSSe thin films were deposited and selenized on molybdenum on glass and following that 50 nm CdS was deposited using chemical bath deposition. 50 nm i-ZnO is then deposited using DC sputtering followed by 400 nm ITO deposited using RF sputtering. Lastly, a patterned Au grid is thermally evaporated as the top electrode.

Figure 5.11a shows the cross-sectional SEM image of as-prepared CZTSSe solar cell with the configuration - Mo/CZTSSe/CdS/ZnO/ITO/Au. The CZTSSe solar cells were divided into smaller cells each with a defined area of 0.11  $\text{cm}^2$ . The current density – voltage (J–V) characteristics for a typical as-prepared CZTSSe solar cell measured in the dark and under AM1.5G illuminations are shown in Figure 5.11b. The device demonstrates a total power conversion efficiency (PCE) of 5.12% with open-circuit



voltage ( $V_{oc}$ ) of 378 mV, short-circuit current density ( $J_{sc}$ ) of 26.2 mA/cm<sup>2</sup>, fill factor (FF) of 51.7%. The series resistance ( $R_s$ ) and shunt resistance ( $R_{sh}$ ) are determined to be 3.6  $\Omega \cdot \text{cm}^2$  and 404  $\Omega \cdot \text{cm}^2$  respectively.

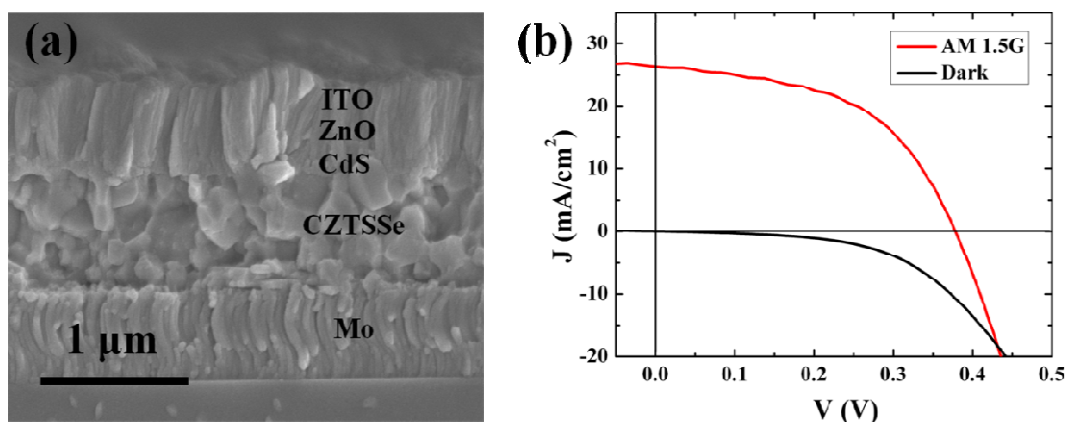


**Figure 5.11.** (a) The cross-sectional SEM image of CZTSSe TFSC and (b) the J-V curve of the as-prepared CZTSSe solar cells in dark and under AM1.5G illumination

Figure 5.12a shows the external quantum efficiency (EQE) of the CZTSSe based solar cell as a function of photon wavelength. The EQE is fairly high (more than 60%) between 500 to 900 nm. The band gap of the absorber layer is determined to be 1.22 eV by fitting a plot of  $[\text{h}\nu \ln(1-\text{EQE})]^2$  vs.  $\text{h}\nu$  near the band edge (Figure. 5.12b). The calculation of band gap based on EQE results instead of optical absorption or other method is because the EQE method allows the measurement and calculation in a full solar cell. Our band gap matches well with the reported range of 1.0 eV to 1.5 eV for CZTSSe using EQE measurements.<sup>33</sup> It is also in good agreement with the band gap of CZTSSe based on optical absorption measurement.<sup>34</sup> The band gap estimated based on EQE is reasonable considering the majority of S atoms are replaced with Se during the selenization process.

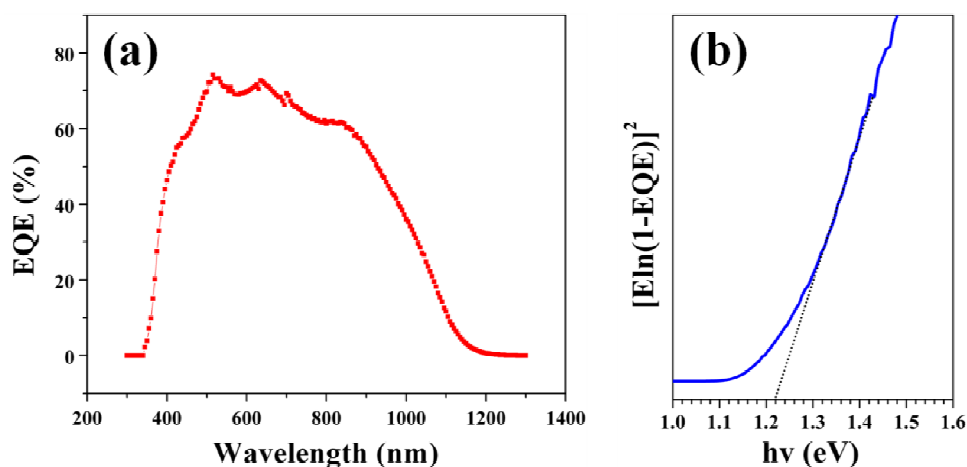


**Figure 5.12.** (a) The EQE of the CZTSSe solar cell, and (b) the corresponding  $(\ln(1-EQE))^2$  vs.  $h\nu$  plot where the band gap is determined to be 1.18 eV.

Our solar cell performances are comparable with the above best performing nanoparticles based CZTSSe solar cells. Woo et al. reported CZTS solar cells with ball milled  $\text{Cu}_2\text{S}$ , Zn, Sn and S powders.<sup>35</sup> They managed to achieve an efficiency of 5.14%,  $V_{oc}$  of 516.9 mV,  $J_{sc}$  of 18.9  $\text{mA}/\text{cm}^2$ , FF of 52.8%. Using CZTS nanoparticles, Guo et al. prepared CZTSSe solar cells with efficiency of 7.2% ( $V_{oc} = 430$  mV,  $J_{sc} = 31.2$   $\text{mA}/\text{cm}^2$ , FF = 53.9%).<sup>14</sup> The lower  $V_{oc}$  value compared with that of Woo et al. are most probably due to the band gap of the absorber film. Woo et al. made use of pure sulfide system and had a band gap of 1.51 eV compared with our value of 1.22 eV. The slight discrepancy of  $V_{oc}$  between our value and that of Guo et al. could possibly arise from the fabrication processes. In terms of  $J_{sc}$  value, our value is between those of Woo et al. and Guo et al. This could also be reflected from the EQE results. Woo et al. reported a narrower EQE region with EQE value drop to zero at around 900 nm wavelength. By contrast, both our and Guo et al.'s EQE region extend to beyond to 1200 nm with more squarish shape. The reason is that with Se incorporation, the band gap is reduced which enhances the light

absorption at near infrared wavelength. Our EQE value show a maximum of around 74.3%, while the maximum value for Guo et al. is around 90%. This indicates that CZTSSe films may have more defects which lead to recombination of charge carriers and thus a lower  $J_{sc}$  value. Our FF value is quite comparable to those of Woo et al. and Guo et al.

Despite the above progress, our solar cell performance is still considered low as compared with the hydrazine method.<sup>19</sup> For instance, Todorov et al. obtained 11.1% efficient device with  $V_{oc}$  of 460 mV,  $J_{sc}$  of 34.5 mA/cm<sup>2</sup> and FF of 69.8%.<sup>15</sup> By comparison, our  $V_{oc}$ ,  $J_{sc}$  and FF are all significant lower than above values. The ideality factor ( $n$ ) of our device is about 3.1, in contrast with 1.5 for the above 11.1% efficient cell. In an ideal diode, the ideality factor should be 1 and in that case, assuming no recombination occurs. A higher ideality factor implies that the charge carriers recombination is one of the limiting factors for our devices.<sup>36</sup> In order to reduce recombination, future work may focus on increasing grain size of CZTSSe, improving the contact between Mo and CZTSSe, between CZTSSe and CdS.

## 5.4 Conclusions

In conclusion, we have developed a low-cost, environmentally friendly and easily upscalable method to prepare CZTS thin film making use of aqueous solution synthesized CuS, ZnS and SnS<sub>2</sub> nanoparticles. The post-annealing plays an important role in the phase evolution from binary phases into quaternary CZTS phase. It was found that pure CZTS phase formed at 300°C, 400°C and 450°C based on XRD and Raman results. Due to the high reactivity of nanoparticles precursor, it is possible to form CZTS phase at far

more lower temperature than conventional reported value of above 500°C. The CZTS film exhibits a thickness of around 1  $\mu\text{m}$  with average grain size of 100 nm. It is also worth highlighting that the as-prepared CZTS films were S rich due to the excess sulfur content associated with the binary sulfides phases. Furthermore, the composition of stoichiometric CZTS and Zn-rich CZTS were demonstrated and their band gaps were determined by UV-vis-NIR measurement to be 1.43 eV and 1.52 eV respectively.

CZTSSe TFSCs were fabricated with the binary sulfides nanoparticles approach. The selenization process was performed on the nanoparticles precursor film. The selenized film exhibits a significant large grain size as compared to the annealed film. The as-fabricated device exhibited a total area efficiency of 5.12% with  $V_{oc}$  of 378 mV,  $J_{sc}$  of 26.2  $\text{mA}/\text{cm}^2$  and FF of 51.7%. These results are comparable with some of the best performing nanoparticles based CZTSSe solar cells. Combined with the low-cost, environmentally friendly and upscalable fabrication steps, our synthesis method is highly promising for potential industry scale application. At the moment, this work is still at early stage due to the constraint of time and manpower. A lot more work needs to be done before its real application. Future work may focus on increasing grain size of CZTSSe, improving the contact between Mo and CZTSSe, between CZTSSe and CdS to improve the device performance.

## References

1. Katagiri, H.,  $\text{Cu}_2\text{ZnSnS}_4$  thin film solar cells. *Thin Solid Films* **2005**, 480-481, 426-432.
2. Andersson, B. A., Materials availability for large-scale thin-film photovoltaics. *Progress in Photovoltaics* **2000**, 8, (1), 61-76.

3. Mitzi, D. B.; Gunawan, O.; Todorov, T. K.; Wang, K.; Guha, S., The path towards a high-performance solution-processed kesterite solar cell. *Solar Energy Materials and Solar Cells* **2011**, 95, (6), 1421-1436.
4. Repins, I.; Contreras, M. A.; Egaas, B.; DeHart, C.; Scharf, J.; Perkins, C. L.; To, B.; Noufi, R., 19.9%-efficient ZnO/CdS/CuInGaSe<sub>2</sub> solar cell with 81.2% fill factor. *Progress in Photovoltaics* **2008**, 16, (3), 235-239.
5. Jackson, P.; Hariskos, D.; Lotter, E.; Paetel, S.; Wuerz, R.; Menner, R.; Wischmann, W.; Powalla, M., New world record efficiency for Cu(In,Ga)Se<sub>2</sub> thin-film solar cells beyond 20%. *Progress in Photovoltaics* **2011**, 19, (7), 894-897.
6. Katagiri, H.; Sasaguchi, N.; Hando, S.; Hoshino, S.; Ohashi, J.; Yokota, T., Preparation and evaluation of Cu<sub>2</sub>ZnSnS<sub>4</sub> thin films by sulfurization of E-B evaporated precursors. *Solar Energy Materials and Solar Cells* **1997**, 49, (1-4), 407-414.
7. Jimbo, K.; Kimura, R.; Kamimura, T.; Yamada, S.; Maw, W. S.; Araki, H.; Oishi, K.; Katagiri, H., Cu<sub>2</sub>ZnSnS<sub>4</sub>-type thin film solar cells using abundant materials. *Thin Solid Films* **2007**, 515, (15), 5997-5999.
8. Katagiri, H.; Jimbo, K.; Yamada, S.; Kamimura, T.; Maw, W. S.; Fukano, T.; Ito, T.; Motohiro, T., Enhanced conversion efficiencies of Cu<sub>2</sub>ZnSnS<sub>4</sub>-based thin film solar cells by using preferential etching technique. *Applied Physics Express* **2008**, 1, (4).
9. Katagiri, H.; Jimbo, K.; Maw, W. S.; Oishi, K.; Yamazaki, M.; Araki, H.; Takeuchi, A., Development of CZTS-based thin film solar cells. *Thin Solid Films* **2009**, 517, (7), 2455-2460.
10. H.Katagiri, K. J., K.Monya, K.Tsuchida, Solar cell without environmental pollution by using CZTS thin film. *Proceedings of the World Conference on Photovoltaics Energy Conversion* **2003**, III, 2874 -2879.
11. Shin, B.; Gunawan, O.; Zhu, Y.; Bojarczuk, N. A.; Chey, S. J.; Guha, S., Thin film solar cell with 8.4% power conversion efficiency using an earth-abundant Cu<sub>2</sub>ZnSnS<sub>4</sub> absorber. *Progress in Photovoltaics: Research and Applications* 21, (1), 72-76.
12. Scragg, J. J.; Berg, D. M.; Dale, P. J., A 3.2% efficient Kesterite device from electrodeposited stacked elemental layers. *Journal of Electroanalytical Chemistry* **2010**, 646, (1-2), 52-59.
13. Kumar, Y. B. K.; Babu, G. S.; Bhaskar, P. U.; Raja, V. S., Preparation and characterization of spray-deposited Cu<sub>2</sub>ZnSnS<sub>4</sub> thin films. *Solar Energy Materials and Solar Cells* **2009**, 93, (8), 1230-1237.

14. Guo, Q.; Ford, G. M.; Yang, W.-C.; Walker, B. C.; Stach, E. A.; Hillhouse, H. W.; Agrawal, R., Fabrication of 7.2% Efficient CZTSSe Solar Cells Using CZTS Nanocrystals. *Journal of the American Chemical Society* **2010**, 132, (49), 17384-17386.
15. Todorov, T. K.; Tang, J.; Bag, S.; Gunawan, O.; Gokmen, T.; Zhu, Y.; Mitzi, D. B., Beyond 11% efficiency: characteristics of state-of-the-art  $\text{Cu}_2\text{ZnSn}(\text{S},\text{Se})_4$  Solar Cells. *Advanced Energy Materials* **2012**, 3, (1), 34-38.
16. Guo, Q.; Hillhouse, H. W.; Agrawal, R., Synthesis of  $\text{Cu}_2\text{ZnSnS}_4$  nanocrystal ink and its use for solar cells. *Journal of the American Chemical Society* **2009**, 131, (33), 11672-11673.
17. Riha, S. C.; Parkinson, B. A.; Prieto, A. L., Solution-Based Synthesis and Characterization of  $\text{Cu}_2\text{ZnSnS}_4$  Nanocrystals. *Journal of the American Chemical Society* **2009**, 131, (34), 12054-12055.
18. Steinhagen, C.; Panthani, M. G.; Akhavan, V.; Goodfellow, B.; Koo, B.; Korgel, B. A., Synthesis of  $\text{Cu}_2\text{ZnSnS}_4$  nanocrystals for use in low-cost photovoltaics. *Journal of the American Chemical Society* **2009**, 131, (35), 12554-12555.
19. Todorov, T. K.; Reuter, K. B.; Mitzi, D. B., High-efficiency solar cell with earth-abundant liquid-processed absorber. *Advanced Materials* **2010**, 22, (20), E156-E159.
20. Kumar, Y. B. K.; Bhaskar, P. U.; Babu, G. S.; Raja, V. S., Effect of copper salt and thiourea concentrations on the formation of  $\text{Cu}_2\text{ZnSnS}_4$  thin films by spray pyrolysis. *Physica Status Solidi a-Applications and Materials Science* **2010**, 207, (1), 149-156.
21. Kumar, Y. B. K.; Babu, G. S.; Bhaskar, P. U.; Raja, V. S., Effect of starting-solution pH on the growth of  $\text{Cu}_2\text{ZnSnS}_4$  thin films deposited by spray pyrolysis. *Physica Status Solidi a-Applications and Materials Science* **2009**, 206, (7), 1525-1530.
22. Tsukigase, H.; Suzuki, Y.; Berger, M.-H.; ne; Sagawa, T.; Yoshikawa, S., Wet Chemical Synthesis and Self-Assembly of  $\text{SnS}_2$  Nanoparticles on  $\text{TiO}_2$  for Quantum Dot-Sensitized Solar Cells. *Journal of Nanoscience and Nanotechnology* **2010**, 11, (4), 3215-3221.
23. Cheng, A. J.; Manno, M.; Khare, A.; Leighton, C.; Campbell, S. A.; Aydil, E. S., Imaging and phase identification of  $\text{Cu}_2\text{ZnSnS}_4$  thin films using confocal Raman spectroscopy. *Journal of Vacuum Science & Technology A: Vacuum, Surfaces, and Films* **2011**, 29, (5), 051203-11.
24. Fernandes, P. A.; Salome, P. M. P.; da Cunha, A. F., Growth and Raman scattering characterization of  $\text{Cu}_2\text{ZnSnS}_4$  thin films. *Thin Solid Films* **2009**, 517, (7), 2519-2523.

25. Munce, C. G.; Parker, G. K.; Holt, S. A.; Hope, G. A., A Raman spectroelectrochemical investigation of chemical bath deposited  $\text{Cu}_x\text{S}$  thin films and their modification. *Colloids and Surfaces A: Physicochemical and Engineering Aspects* **2007**, 295, (1-2), 152-158.
26. Cheng, Y. C.; Jin, C. Q.; Gao, F.; Wu, X. L.; Zhong, W.; Li, S. H.; Chu, P. K., Raman scattering study of zinc blende and wurtzite  $\text{ZnS}$ . *Journal of Applied Physics* **2009**, 106, (12), 123505-5.
27. Mehdi, A.; Mohamad Mehdi Bagheri, M.; Hosein, E., Preparation and characterization of  $\text{Cu}_2\text{SnS}_3$  ternary semiconductor nanostructures via the spray pyrolysis technique for photovoltaic applications. *Physica Scripta* 85, (3), 035603.
28. Weber, A.; Mainz, R.; Schock, H. W., On the Sn loss from thin films of the material system  $\text{Cu--Zn--Sn--S}$  in high vacuum. *Journal of Applied Physics* 107, (1), 013516-6.
29. H.Katagiri, K. J., M.Tahara, H.Araki, K.Oishi, The influence of the composition ratio on CZTS-based thin film solar cells. *Mater. Res. Soc. Symp. Proc.* **2009**, 1165, M04-01.
30. Liu, Q.; Zhao, Z.; Lin, Y.; Guo, P.; Li, S.; Pan, D.; Ji, X., Alloyed  $(\text{ZnS})_x(\text{Cu}_2\text{SnS}_3)_{1-x}$  and  $(\text{CuInS}_2)_x(\text{Cu}_2\text{SnS}_3)_{1-x}$  nanocrystals with arbitrary composition and broad tunable band gaps. *Chemical Communications* **2010**, 47, (3), 964-966.
31. Rockett, A.; Birkmire, R. W.,  $\text{CuInSe}_2$  for phototovoltaic applications. *Journal of Applied Physics* **1991**, 70, (7), R81-R97.
32. Lakshmikumar, S. T.; Rastogi, A. C., Selenization of Cu and In thin-films for the preparation of selenide phot-absorber layers in solar-cells using Se vapor source. *Solar Energy Materials and Solar Cells* **1994**, 32, (1), 7-19.
33. Haight, R.; Barkhouse, A.; Gunawan, O.; Shin, B.; Copel, M.; Hopstaken, M.; Mitzi, D. B., Band alignment at the  $\text{Cu}_2\text{ZnSn}(\text{S}_x\text{Se}_{1-x})_4/\text{CdS}$  interface. *Applied Physics Letters* **2011**, 98, (25), -.
34. Riha, S. C.; Parkinson, B. A.; Prieto, A. L., Compositionally tunable  $\text{Cu}_2\text{ZnSn}(\text{S}_{1-x}\text{Se}_x)_4$  nanocrystals: probing the effect of Se-inclusion in mixed chalcogenide thin films. *Journal of the American Chemical Society* **2011**, 133, (39), 15272-15275.
35. Woo, K.; Kim, Y.; Moon, J., A non-toxic, solution-processed, earth abundant absorbing layer for thin-film solar cells. *Energy & Environmental Science* **2012**, 5, (1), 5340-5345.
36. Sullivan, J. P.; Tung, R. T.; Pinto, M. R.; Graham, W. R., Electron transport of inhomogeneous Schottky barriers: A numerical study. *Journal of Applied Physics* **1991**, 70, (12), 7403-7424.

# Chapter 6: Conclusions and Future Works

## 6.1 Overall Summary

Quaternary  $\text{Cu}_2\text{ZnSnS}_4$  (CZTS) is a promising absorber material for TFSCs. Conventionally, CZTS thin films were prepared using vacuum deposition techniques. Recently, much progress has been made in the development of low-cost solution deposition methods. Among them, the CZTS nanocrystals ink approach offers the possibility of high performance devices with low fabrication cost. As a result, many research efforts have been dedicated to the synthesis, characterizations and applications of CZTS nanoparticles.

Synthesis parameters such as the reaction temperature, reaction time, solvent and ligand have huge effect on the formation of CZTS nanoparticles. It was found that at temperature below 200 °C, the binary  $\text{Cu}_{2-x}\text{S}$  and ternary  $\text{Cu}_2\text{SnS}_3$  phases formed together with quaternary kesterite CZTS phase. At reaction temperature of 220 °C and above, pure kesterite CZTS phase is favored. The reaction time has great influence on the growth of CZTS nanoparticles. From 0 min to 30 min, the average size of the nanoparticles gradually increased and the size distribution became narrower. With longer reaction time, the nanoparticles show the phenomenon of Ostwald ripening with the growth of large particles with the consumption of small particles. The size and shape of nanoparticles could be controlled through solvent-ligand optimization. With DCB as the solvent and OLA as the ligand, near-spherical shape (0.5 ml OLA), faceted (1 ml OLA), and nanoplates (2 ml OLA) CZTS nanostructures were synthesized.



CZTS kesterite, wurtzite as well as mixed kesterite-wurtzite phases were successfully synthesized by using elemental S, DDT and TAA respectively. It was found that the reaction rate was the key factors that determined the formation of each phase. Elemental S could react with oleylamine to produce highly reactive small molecule  $\text{H}_2\text{S}$ , which then go on to react with Cu, Zn and Sn species to form kesterite CZTS nanoparticles. As for DDT, the covalently bonded S is very stable and it is necessary to break this bond to release the S atom, resulting in a slower reaction rate. DDT selectively reacts with the relatively more reactive “Cu” species to form  $\text{Cu}_7\text{S}_4$  seed, which then gradually evolved into wurtzite CZTS. TAA react with OLA to produce the highly reactive  $\text{H}_2\text{S}$  and less reactive long chain N-substituted thioamides, therefore results in the formation of mixed kesterite and wurtzite phases. From the UV-vis-NIR measurements, the band gap was estimated to be 1.48 eV and 1.55 eV for sample S and TAA respectively. The interference of  $\text{Cu}_7\text{S}_4$  impurity phase makes it difficult to determine the band gap using absorption measurements for the DDT sample. The valance band and conduction band energy levels are determined using CV measurements to be -5.37 and -3.85 eV (sample S), -5.60 and -3.91 eV (sample DDT), -5.55 and -3.99 eV (sample TAA), corresponding to electrical band gaps of 1.52 eV, 1.69 eV and 1.56 eV respectively.

The low-cost, environmentally friendly water based nanocrystal ink using CuS, ZnS and  $\text{SnS}_2$  nanoparticles was also developed. Post-annealing at 300 °C and above promoted the solid-state reactions between the binary CuS, ZnS and  $\text{SnS}_2$  to form quaternary CZTS phases. The composition of CZTS film can be tuned by modifying the molar ratio of binary sulfides precursors. The band gaps of as-prepared stoichiometric CZTS and Zn-rich CZTS were determined by UV-vis-NIR measurement to be 1.43 eV and 1.52 eV

respectively. CZTS based TFSCs were fabricated with the binary sulfides nanoparticles approach. The device demonstrates a total area efficiency of 5.12% with  $V_{oc} = 378$  mV,  $J_{sc} = 26.2$  mA/cm<sup>2</sup> and FF = 51.7%. The series resistance ( $R_s$ ) and shunt resistance ( $R_{sh}$ ) are determined to be  $3.6 \Omega \cdot \text{cm}^2$  and  $404 \Omega \cdot \text{cm}^2$ . Combined with the low-cost, environmentally friendly and upscalable fabrication steps, our synthesis method is highly promising for potential industry scale application.

### 6.2 Scientific Contributions

1. Detailed investigations on the effects of synthesis parameters including reaction temperature, reaction time, solvent and ligand were performed. The growth mechanism of CZTS nanoparticles were proposed based on results from time-dependent studies. The knowledge could provide guideline for the controlled synthesis of CZTS nanoparticles.
2. CZTS kesterite, wurtzite and mixed kesterite-wurtzite phases were synthesized using different sulfur sources. It was found for the first time that the reaction rate of sulfur precursor is the key factor that determines the formation of each phase.
3. Cyclic voltammetry studies have been used for the first time to estimate the conduction band energy, valence band energy as well as the electrical band gap of CZTS. The conduction band energy and valence band energy of wurtzite CZTS were first reported.
4. The water based nanocrystals ink using CuS, ZnS and SnS<sub>2</sub> nanoparticles has been developed for the first time. The as-prepared solar cells demonstrated an encouraging performance with a total area efficiency of 5.12%.

### 6.3 Future Directions

The studies and findings shown in this thesis dissertation provide better understanding of the synthesis and formation mechanisms of both kesterite and wurtzite CZTS nanoparticles. The knowledge is very useful for the preparations and applications of CZTS nanoparticles. In addition, water based nanocrystals ink using CuS, ZnS and SnS<sub>2</sub> nanoparticles is very promising due to low fabrication cost and environmental factors. However, there are still some issues described below needs to be tackled.

1. The choices of solvent and ligand were limited due to time constrain. In this thesis, DCB was used as the solvent, and OLA was used both as the solvent and ligand. Future research efforts could be made to explore other solvents like 1-hexadecane (C<sub>16</sub>H<sub>34</sub>), and ligands such as trioctylphosphine oxide (TOPO), hexadecylamine (HDA), oleic acid (OA) and dodecylphosphonic acid (DDPA). The optimization of solvent and ligand may led to better control in the size and morphology of CZTS nanoparticles
2. The composition uniformity and localized secondary phases were two main problems that reduced the solar cells performance. More work needs to be done to find ways to prepare highly pure CZTSSe thin film with uniform composition distribution. Studies using electron probe micro-analyzer (EPMA) and cross-sectional EDS line on the CZTSSe film scan may help to solve these problems.
3. The loss mechanism of as-prepared CZTSSe solar cells needs to be investigated. The knowledge of the loss mechanism could provide guidelines for future

advancement of the devices. In view of this, the time-resolved photoluminescence (TRPL) studies could be carried out.

## Appendix A

### Compositional Analysis of CZTS Nanoparticles and Thin Films

The composition of  $\text{Cu}_2\text{ZnSnS}_4$  nanoparticles and thin films was analyzed using an energy dispersive X-ray spectroscopy (EDS) equipped on a FESEM. The accelerating voltage of 20 kV was used. In a typical measurement, the percentages of S, Cu, Zn and Sn for five different spots were measured, and then the average percentages were determined. The ratio for each element was calculated by dividing each percentage with 12.5% respectively. Table A1 shows the EDS measurements of CZTS nanoparticles prepared using hot injection method is presented with Cu: Zn: Sn: S ratio of 1.96: 0.8: 1.05: 4.19. In Table A2, the compositional information of CZTS thin film prepared using binary sulfide approach is presented, showing a Cu: Zn: Sn: S ratio of 1.96: 1.00: 1.05: 4.11.

**Table A1:** EDS measurements of kesterite CZTS nanoparticles sample

Elements	#1 (%)	#2 (%)	#3 (%)	#4 (%)	#5 (%)	Ave. (%)	Ratio
S	51.77	52.74	52.46	53.27	51.57	52.36	4.19
Cu	24.82	23.79	24.96	23.98	25.00	24.51	1.96
Zn	10.09	10.20	9.46	9.88	10.44	10.01	0.80
Sn	13.32	13.27	13.12	12.87	12.99	13.11	1.05

**Table A2:** EDS measurements of CZTS thin film using binary sulfide approach

Elements	#1 (%)	#2 (%)	#3 (%)	#4 (%)	#5 (%)	Ave. (%)	Ratio
S	50.64	50.11	51.51	51.37	53.49	51.42	4.11
Cu	25.75	24.40	25.20	23.99	22.89	24.45	1.96
Zn	11.71	14.19	12.25	13.27	11.20	12.52	1.00
Sn	11.90	11.30	11.04	11.37	12.42	11.61	0.93

The XRD results in Chapter 5 show that the as synthesized  $\text{SnS}_2$  contains high content of amorphous phase. In addition to XRD, EDS measurements were also carried out. Table A3 presents the EDS results for the as-synthesized  $\text{SnS}_2$  sample. The ratio between S to Sn was determined to 1.79: 1.

**Table A3:** EDS measurements of  $\text{SnS}_2$  sample

Elements	#1 (%)	#2 (%)	#3 (%)	#4 (%)	#5 (%)	Ave. (%)	Ratio
S	63.98	64.67	62.90	64.35	65.01	64.18	1.79
Sn	36.02	35.33	37.10	35.65	34.99	35.82	1

## Appendix B

### TOPAS refinement of CZTS samples prepared with TAA

The XRD pattern of sample DDT was refined. As shown in Figure A1, the XRD pattern matches well with the calculated data for CZTS wurtzite structure. As discussed in Chapter 4, the CZTS samples prepared using TAA as sulfur source were found to be a mixture of kesterite and wurtzite phases. In order to determine the relative amount of each phase, the rietveld TOPAS refinement was also performed on sample TAA (Figure A2). It was found that the CZTS samples prepared using TAA as sulfur source contains 50.3 wt% of kesterite phase and 49.7 wt% of wurtzite phase.

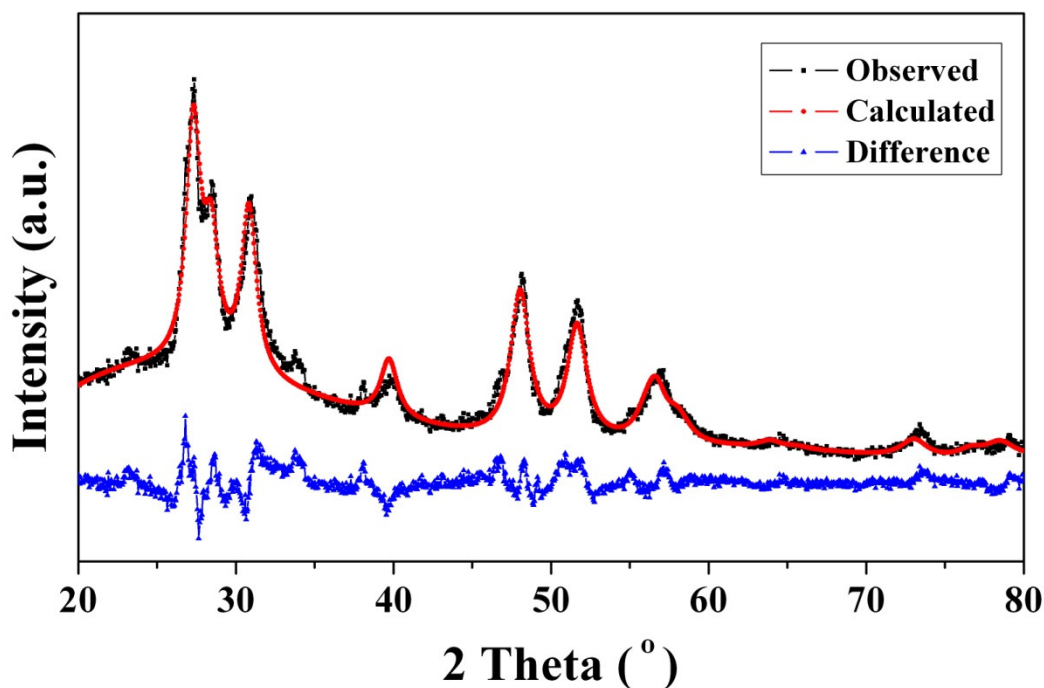


**Figure A1:** The retrieved TOPAS refinement results for Sample DDT. The XRD pattern matches with the CZTS wurtzite structure.

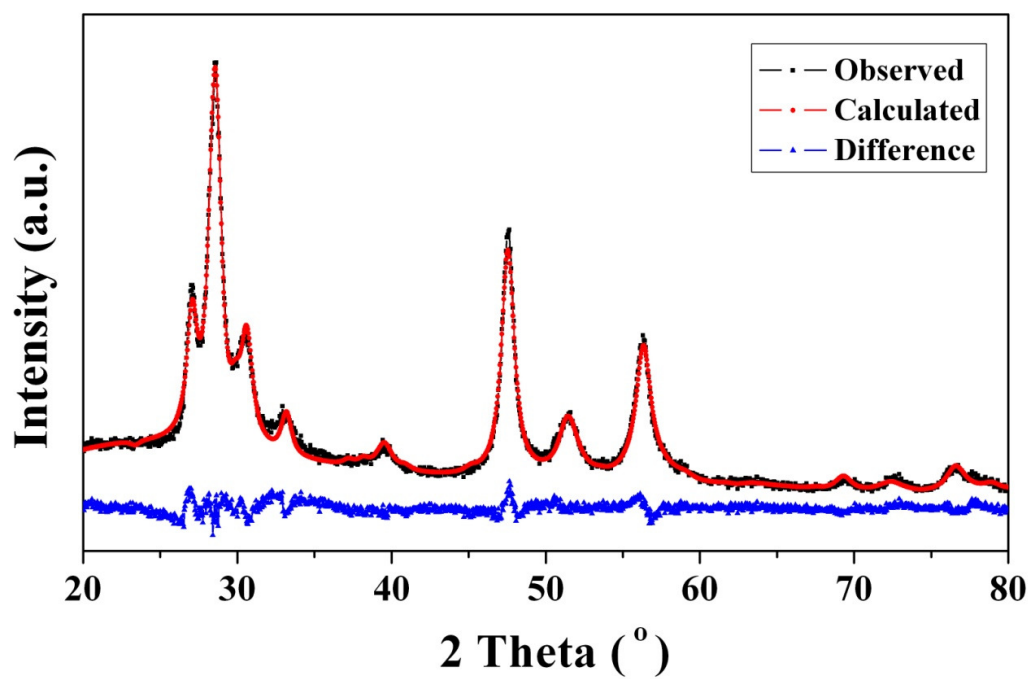


**Figure A2:** The retrieved TOPAS refinement results of sample TAA shows that this sample contains 50.3 wt% of kesterite phase and 49.7 wt% of wurtzite phase.



### Appendix C

#### Time -dependent studies of CZTS nanoparticles prepared using DDT

Figure A3 shows the TEM images of nanoparticles prepared with DDT as the sulfur source. It could be observed that the size of nanoparticles increases gradually with respect to reaction time. At 10 min and 30 min (Figure A3 a and b), the shape of nanoparticles is mainly near-spherical. At 1 hour (Figure A3c), the nanocube-, nanobrick-like shapes start to emerge. At 2 hour (Figure A3d), more nanocubes and nanobricks are observed.

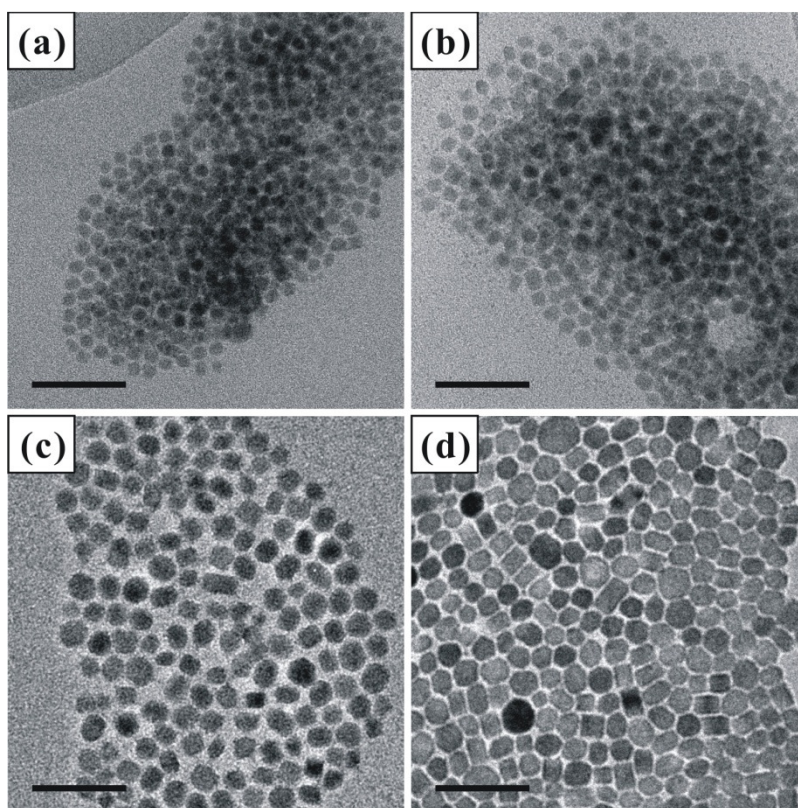


**Figure A3:** The TEM images of nanoparticles prepared using DDT as precursor reacted for (a) 10 min, (b) 30 min, (c) 1 hour and (d) 2 hour.